

1 MEASUREMENT OF ELECTROWEAK PRODUCTION OF
2 SAME-SIGN W BOSON PAIRS WITH ATLAS

3 William Kennedy DiClemente

4 A DISSERTATION
5 in
6 Physics and Astronomy

7 Presented to the Faculties of The University of Pennsylvania
8 in Partial Fulfillment of the Requirements for the Degree of Doctor of Philosophy
9 2019 *Last compiled: February 27, 2019*

10

11 I. Joseph Kroll, Professor, Physics
12 Supervisor of Dissertation

13

14 Joshua Klein, Professor, Physics
15 Graduate Group Chairperson

16 Dissertation Committee
17 Elliot Lipeles, Associate Professor, Physics
18 Christopher Mauger, Associate Professor, Physics
19 Burt Ovrut, Professor, Physics
20 Justin Khoury, Professor, Physics
21 I. Joseph Kroll, Professor, Physics

22 MEASUREMENT OF ELECTROWEAK PRODUCTION OF SAME-SIGN W BOSON PAIRS
23 WITH ATLAS

24 COPYRIGHT
25 2019
26 William Kennedy DiClemente

27 All rights reserved.

Acknowledgements

29 It would be impossible to properly thank everyone who has helped me along this journey; nevertheless
30 I will attempt to be as thorough as possible.

31 First and foremost, I would like to thank my family. My parents, Gwynne Kennedy and John
32 DiClemente, for always believing in me and listening to me attempt to explain what it is I am
33 working on. My many feline friends past and present—Stella, Lucky, Julia, Elise, Lucille, Tweedie,
34 Ruby, and Sylvie—for keeping me warm during the winter holidays back home. My girlfriend Amber
35 Wright, for tolerating me these past few months and doing your best to keep me relatively sane.

36 Thanks to my advisor Joe Kroll for guiding me through the past six years at Penn; your advice
37 both in physics and in life has been invaluable to my growth as a physicist and a person. Additional
38 thanks to the rest of the ATLAS faculty at Penn: Elliot Lipeles, Evelyn Thomson, and Brig Williams.
39 The amount of open collaboration between students and faculty irrespective of who works for whom
40 has helped me learn so much.

41 I would also like to extend thanks to two important figures from before my time at Penn. Firstly,
42 to Gardner Friedlander, my high school physics teacher who first got me interested in the subject.
43 You were the first to show me how I could use a pen and paper to predict events in real life, a
44 fascination of mine that has continued into my work here, just with much harder math and on a more
45 fundamental scale. Secondly, my undergraduate research advisor, Al Goshaw, at Duke University.
46 You gave a college freshman who thought particle physics was “pretty neat” the opportunity to do
47 meaningful research with one of the leading collaborations in the field. Without either of you, I
48 likely would not be in this position today.

49 Thanks to the members of the Inner Detector Alignment group, including but not limited to
50 Anthony Morley for his guidance on my qualification task, and to Shih-Chieh Hsu, Pierfrancesco
51 Butti, Matthias Danninger, Salvador Marti, and Steffen Henkelmann for numerous collaborative

52 alignment efforts.

53 The entire $W^\pm W^\pm jj$ 13 TeV analysis group, and those with whom I worked most closely: Philip
54 Sommer, Emily Duffield, Rustem Ospanov, Stefanie Todt, and Liqing Zhang. Special thanks to
55 Rustem for pushing me to find my voice in the analysis. Thanks to my $W^\pm W^\pm jj$ 14 TeV prospects
56 collaborators Claire Lee and Karolos Potamiamos.

57 Lastly, thanks to my fellow Penn ATLAS graduate students, Bijan Haney, Joey Reichert, Khilesh
58 Mistry, Leigh Schaefer, Bill Balunas, Christian Herwig, Elodie Ressegue, and many more, for lis-
59 tening to my ramblings, answering my many questions, and for countless entertaining lunchtime
60 discussions.

ABSTRACT

62 MEASUREMENT OF ELECTROWEAK PRODUCTION OF SAME-SIGN W BOSON PAIRS
 63 WITH ATLAS

William Kennedy DiClemente

J. Kroll

66 This thesis presents two studies of electroweak same-sign $W^\pm W^\pm jj$ scattering with the ATLAS
 67 experiment. The first is a measurement of the fiducial cross section at $\sqrt{s} = 13$ TeV using 36.1 fb^{-1}
 68 of data recorded in 2015 and 2016. The electroweak production is observed with a signal significance
 69 of 6.9σ , and the fiducial cross section is measured to be $\sigma_{\text{meas}}^{\text{fid}} = 2.91^{+0.51}_{-0.47}(\text{stat})^{+0.28}_{-0.29}(\text{sys}) \text{ fb}$. The
 70 second is a study on the future prospects for the $W^\pm W^\pm jj$ process at the planned High-Luminosity
 71 LHC, with a projected $\sqrt{s} = 14$ TeV and 3000 fb^{-1} of data. The expected electroweak production
 72 cross section is determined with a total uncertainty of 6%, and the purely longitudinal scattering
 73 component is extracted with an expected significance of 1.8σ . Additionally, some time is taken to
 74 detail the alignment of the ATLAS Inner Detector subsystems, as good alignment performance is
 75 essential for making high-quality physics measurements.

Contents

77	Acknowledgements	iii
78	Abstract	v
79	Contents	vi
80	List of Tables	x
81	List of Figures	xiii
82	Preface	xix
83	1 Introduction	1
84	2 Theoretical Framework	3
85	2.1 Introduction to the Standard Model	3
86	2.2 Electroweak symmetry breaking and the Higgs boson	6
87	2.3 Electroweak vector boson scattering	9
88	3 LHC and the ATLAS Detector	12
89	3.1 The Large Hadron Collider	12
90	3.2 The ATLAS Detector	15
91	3.2.1 The Inner Detector	16
92	3.2.1.1 Pixel Detector	17
93	3.2.1.2 Semiconductor Tracker	18
94	3.2.1.3 Transition Radiation Tracker	18

95	3.2.2	The Calorimeters	19
96	3.2.2.1	Liquid Argon Calorimeter	20
97	3.2.2.2	Tile Calorimeter	22
98	3.2.3	The Muon Spectrometer	22
99	3.2.4	Particle reconstruction	23
100	3.2.4.1	Track reconstruction	23
101	3.2.4.2	Muon reconstruction	23
102	3.2.4.3	Electron reconstruction	23
103	3.2.4.4	Jet reconstruction	23
104	4	Alignment of the ATLAS Inner Detector	24
105	4.1	The alignment method	25
106	4.1.1	Alignment levels	28
107	4.1.2	Alignment coordinate systems	29
108	4.2	Early 2015 alignment of the ATLAS detector	30
109	4.2.1	June alignment procedure	31
110	4.2.2	Alignment results	33
111	4.2.2.1	Residual distributions from collisions	34
112	4.2.2.2	Track parameter resolution from cosmic rays	38
113	4.2.3	Error scaling	39
114	4.3	Level 2 alignment of the TRT	41
115	4.4	Momentum bias from sagitta deformations	42
116	4.4.1	Sagitta bias monitoring with electron E/p	43
117	4.4.1.1	Measuring $\langle E/p \rangle$	44
118	4.4.1.2	Results in 13TeV data	46
119	5	Measurement of same-sign WW production at $\sqrt{s} = 13$ TeV with ATLAS	49
120	5.0.1	Experimental overview of vector boson scattering	49
121	5.0.2	Same-sign $W^\pm W^\pm$ scattering	50
122	5.0.3	Overview of backgrounds	52
123	5.1	Data and Monte Carlo samples	54
124	5.1.1	Monte Carlo samples	55
125	5.2	Object and event selection	57

126	5.2.1	Object selection	57
127	5.2.1.1	Muon candidate selection	57
128	5.2.1.2	Electron candidate selection	58
129	5.2.1.3	Jet candidate selection	60
130	5.2.1.4	Treatment of overlapping objects	60
131	5.2.2	Signal event selection	61
132	5.3	Background estimations	62
133	5.3.1	Estimation of the WZ background	63
134	5.3.2	Estimation of the $V\gamma$ background	64
135	5.3.3	Estimation of backgrounds from charge misidentification	66
136	5.3.3.1	Validation of the charge misidentification estimate	68
137	5.3.4	Estimation of non-prompt backgrounds with the fake-factor method	69
138	5.3.4.1	Overview of the default fake-factor method	70
139	5.3.4.2	The fake-factor with p_T^{cone}	72
140	5.3.4.3	Application of the fake-factor	73
141	5.3.4.4	Systematic uncertainties	78
142	5.3.4.5	Results of the fake-factor	78
143	5.3.4.6	Validation of the fake-factor	80
144	5.3.5	Reduction of WZ background using custom overlap removal	82
145	5.4	Cross section measurement	86
146	5.4.1	Maximum likelihood fit	87
147	5.4.2	Definition of the fiducial volume	88
148	5.4.3	Cross section extraction	90
149	5.5	Summary of uncertainties	91
150	5.5.1	Experimental uncertainties	91
151	5.5.2	Theoretical uncertainties	93
152	5.5.2.1	Uncertainties from EWK-QCD interference	93
153	5.6	Results	94
154	6	Prospects for same-sign WW at the High Luminosity LHC	98
155	6.0.1	Analysis Overview	99
156	6.1	Theoretical motivation	100
157	6.1.1	Experimental sensitivity to longitudinal polarization	100

158	6.2 Monte Carlo samples	101
159	6.3 Background estimations	102
160	6.3.1 Truth-based isolation	103
161	6.4 Object and event selection	104
162	6.4.1 Object selection	104
163	6.4.2 Event selection	104
164	6.5 Selection optimization	105
165	6.5.1 Random grid search algorithm	106
166	6.5.2 Inputs to the optimization	107
167	6.5.3 Results of the optimization	108
168	6.6 Results	109
169	6.6.1 Event yields	109
170	6.6.2 Uncertainties	113
171	6.6.3 Cross section measurement	113
172	6.6.4 Longitudinal scattering significance	114
173	7 Conclusion	118
174	A Additional material on $W^\pm W^\pm jj$ measurement at $\sqrt{s} = 13\text{TeV}$	119
175	A.1 Impact of experimental uncertainty on MC background estimations	119
176	A.2 Additional signal region plots	121
177	B Additional material on $W^\pm W^\pm jj$ prospects at the HL-LHC	122
178	B.1 Truth isolation	122
179	B.1.1 TRUTH1++ derivations	123
180	B.1.2 Check of truth-based isolation	124
181	B.1.3 Loose isolation working point	124
182	B.2 Plots of other optimization variables	127
183	Bibliography	129

List of Tables

185 4.1	The four alignment levels for each of the detector subsystems. The total number of alignable structures and degrees of freedom (DoF) to be aligned are given for each level.	30
187 4.2	Summary of the highest level of alignment applied to each ID subsystem when deriving the June alignment.	33
189 4.3	Estimated value of the error scaling term b for each subdetector component with the June alignment.	40
191 5.1	Predicted cross sections for EQK and QCD production of diboson processes relevant to VBS at $\sqrt{s} = 13\text{TeV}$ using the SHERPA MC generator. The numbers for the $W^\pm W^\pm jj$ process are bolded. Leptons are required to have $p_T \geq 25\text{ GeV}$ and lie within $ \eta \leq 2.5$ with $m_{ll} > 20\text{ GeV}$, and at least two jets are required with $p_T \geq 30\text{ GeV}$ and $ \eta < 4.5$. The VBS contributions are enhanced by requiring the dijet invariant mass $m_{jj} > 500\text{ GeV}$ and dijet separation $\Delta y_{jj} > 2.4$	52
197 5.2	Summary of MC samples used in the analysis.	56
198 5.3	Muon selection criteria. All muons are required to pass the preselection (top), and then either the signal (middle) or loose (bottom) criteria is applied to the preselected electrons.	58
200 5.4	Electron selection criteria. All electrons are required to pass the preselection (top), and then either the signal (middle) or loose (bottom) criteria is applied to the preselected electrons.	59
203 5.5	Jet selection criteria. All jets are required to pass the above selection in order to be used in the analysis.	60
205 5.6	Summary of the overlap removal procedure used in the analysis. If the criteria in the “check” column is met, in the “result” column, the object on the left of the arrow is removed in favor of the object on the right.	61
208 5.7	Summary of trigger requirements for electrons and muons for $\sqrt{s} = 13\text{TeV}$ data collected in 2015 and 2016. At least one of the triggers must be satisfied.	62
210 5.8	The signal event selection.	63
211 5.9	Event yields in the WZ control region before normalization. All lepton flavor channels are combined.	64
213 5.10	Selection criteria for the $V\gamma$ control region.	65
214 5.11	Event yields in the $V\gamma$ control region. The $V\gamma$ scale factor of 1.77 is calculated by scaling up the $Z\gamma$ and $Z+jets$ backgrounds to account for the difference between the data and predicted total background.	66

217	5.12 Selection criteria for the same-sign inclusive validation region.	69
218	5.13 Event selection for the dijet region used for calculating the fake-factor. The selected lepton can pass either the nominal (signal) or loose selections. In the case of the nominal leptons, the $p_T > 27$ GeV requirement is replaced with $p_T > 15$ GeV.	75
221	5.14 Values of the fake-factor in each p_T bin and for each individual systematic source.	79
222	5.15 Estimated yields for the fake lepton background. The estimated yield is shown in the first column together with the statistical uncertainty followed by the systematic uncertainties from variations of the the fake-factors within their statistical (stat.) and systematic (syst.) uncertainties. The labels f_e and f_μ indicate the fake-factors for electrons and muons, respectively.	79
227	5.16 Selection criteria for the same-sign top fakes validation region.	80
228	5.17 Custom OR definition. Leptons must pass this selection in order to be counted for the trilepton veto.	85
230	5.18 Definition of the fiducial volume.	89
231	5.19 Impact of various systematic effects on the fiducial cross section measurement. The impact of a given source of uncertainty is computed by performing the fit with the corresponding nuisance parameter varied up or down by one standard deviation from its nominal value.	91
235	5.20 List of sources of experimental uncertainties on the reconstruction of physics objects.	92
236	5.21 Impact of experimental uncertainties for the $W^\pm W^\pm jj$ EWK processes in all channels.	92
237	5.22 Impact of experimental uncertainties for the WZ process in all channels.	93
238	5.23 The set of generator level cuts used for generating the interference samples with <code>MadGraph</code>	94
239	5.24 Cross sections for each different $W^\pm W^\pm jj$ production mode (inclusive, EWK only, QCD only, and interference only) generated using <code>MadGraph</code> . The cross sections are calculated using a minimal set of generator level cuts from events where the W decays to a muon.	94
242	5.25 Table of the data and prediction event yields in the signal region before the fit. Numbers are shown for the six lepton flavor and charge channels and for all channels combined. Here the WZ background yields are normalized to the data in the WZ control region. The background estimations from the fake-factor are included in the “Non-prompt” category, and backgrounds from $V\gamma$ production and electron charge misidentification are combined in the “ e/γ conversions” category. Finally, ZZ , VVV , and $t\bar{t} + V$ backgrounds are combined in the “Other prompt” category.	95
249	5.26 Table of the data and prediction event yields in the signal region after the fit. Numbers are shown for the six lepton flavor and charge channels and for all channels combined. The background estimations from the fake-factor are included in the “Non-prompt” category, and backgrounds from $V\gamma$ production and electron charge misidentification are combined in the “ e/γ conversions” category. Finally, ZZ , VVV , and $t\bar{t}V$ backgrounds are combined in the “Other prompt” category.	95
255	6.1 Summary of MC samples used in the analysis.	102
256	6.2 Truth-based isolation requirements for electrons and muons.	103
257	6.3 Summary of the signal event selection.	105
258	6.4 Updates to the $W^\pm W^\pm jj$ event selection criteria after optimization. Cuts not listed remain unchanged from the default selection in Table 6.3.	109
260	6.5 Signal and background event yields using the default event selection for an integrated luminosity of $\mathcal{L} = 3000 \text{ fb}^{-1}$. Events containing a fake or charge-flipped electron are removed from their respective sources and combined into a single entry each.	110

263	6.6	Signal and background event yields using the optimized event selection for an integrated luminosity of $\mathcal{L} = 3000 \text{ fb}^{-1}$. Events containing a fake or charge-flipped electron are removed from their respective sources and combined into a single entry each.	111
265	6.7	Summary of estimated experimental and rate uncertainties.	114
267	A.1	Impact of experimental uncertainties for the $W^\pm W^\pm jj$ QCD processes in all channels.	119
268	A.2	Impact of experimental uncertainties for triboson process in all channels.	120
269	A.3	Impact of experimental uncertainties for $t\bar{t}V$ processes in all channels.	120
270	A.4	Impact of experimental uncertainties for the $W\gamma$ process in all channels.	120
271	A.5	Impact of experimental uncertainties for the $Z\gamma$ process in all channels.	120
272	A.6	Impact of experimental uncertainties for the ZZ process in all channels.	121
273	B.1	Event yields prior to applying any form of truth-based isolation criteria.	122
274	B.2	Event yields after applying a test version of the truth-based isolation.	123
275	B.3	Electron and muon isolation requirements for the loose working point.	124
276	B.4	Event yields broken down by sample and by background type using the loose isolation workingpoint. Events contining a fake or charge-flipped electron are removed from their respective sample and added to the “fakes” and “charge flip” rows, respectively. Errors include statistical uncertainty and estimated systematic rate uncertainty based on the background process.	125
281	B.5	Event yields broken down by background type using the tight isolation workingpoint. Events contining a fake or charge-flipped electron are removed from their respective sample and added to the “fakes” and “charge flip” rows, respectively. Errors include statistical uncertainty and estimated systematic rate uncertainty based on the background process.	126

List of Figures

287 2.1	Summary of several Standard Model total and fiducial production cross section measurements compared to the corresponding theoretical predictions calculated at NLO or higher. The dark colored error bar represents the statistical uncertainty, and the light colored error bar represents the full uncertainty (including systematic and luminosity uncertainties). The data/theory ratio, luminosity used and reference for each measurement are also shown.	4
293 2.2	An illustration of the potential term $V(\phi)$ in Equation 2.6 for the cases where $\mu^2 > 0$ (left) and $\mu^2 < 0$ (right). The right-hand plot shows the Higgs potential, or “Mexican hat potential”, with the minimum at $ \phi = \sqrt{-\frac{\mu^2}{\lambda}}$ rather than at $ \phi = 0$ as in the left-hand plot.	7
297 2.3	Feynman diagram of a generic VBS process. The gray circle represents any interaction with two incoming and two outgoing vector bosons, including any of the diagrams shown in Figures 2.4 and 2.5.	9
300 2.4	Leading order $VV \rightarrow VV$ Feynman diagrams involving EWK bosons. From left to right: s -channel, t -channel, u -channel, and the quartic gauge coupling.	9
302 2.5	Leading order $VV \rightarrow VV$ Feynman diagrams involving the exchange of a Higgs boson. From left to right: s -channel, t -channel, and u -channel.	10
304 2.6	Cross sections in nanobarns for five different longitudinally polarized VBS processes as a function of center of mass energy \sqrt{s} . Without a Higgs boson (left), the cross sections grow unbounded with \sqrt{s} . With a 120 GeV Higgs boson (right), the cross sections no longer diverge.	11
308 3.1	The CERN accelerator complex. For LHC collisions, protons are accelerated in the PSB (purple), the PS (magenta), and the SPS (light blue) before entering the LHC ring (dark blue).	13
311 3.2	Peak instantaneous luminosity delivered to ATLAS during 13TeV pp data taking as a function of time.	14
313 3.3	Integrated luminosity collected by ATLAS as a function of time at 13TeV from 2015-2018.	14
314 3.4	Distribution of the mean number of interactions per bunch crossing for the 2015 and 2016 pp collision data at 13TeV.	15
316 3.5	Cut-away view of the ATLAS detector.	16
317 3.6	The barrel layers of the Pixel, SCT, and TRT detectors making up the Inner Detector.	17

318	3.7	Cut-away view of the ATLAS calorimeter systems [1].	20
319	3.8	Diagram of the cells within the LAr barrel. The accordion structure can be seen in the cut-away view.	21
321	4.1	Graphical representation of the effect of a misaligned detector element. The reconstructed particle track (dashed arrow) differs from the actual trajectory of the particle (solid arrow) due to the shift in one of the detector elements. The cyan lines represent the track-to-hit residuals.	25
325	4.2	Graphical representation of the ID alignment chain.	28
326	4.3	A schematic representation of the Inner Detector in the longitudinal plane with the global coordinate system overlaid on top. The Pixel detector and IBL are shown in blue, the SCT in green, and the TRT in red. The local coordinates for each subdetector module are inset on the right.	31
330	4.4	The d_0 distributions with respect to the reconstructed primary vertex using the $\sqrt{s} = 13\text{TeV}$ collision data sample reconstructed using the June (black) and March (green) alignments. The data is compared to a MC simulation using a perfect detector geometry (red). The distributions are normalized to the same number of entries.	34
334	4.5	Local x (left) and local y (right) residual distributions of the IBL planar sensors using the $\sqrt{s} = 13\text{TeV}$ collision data sample reconstructed using the June (black) and March (green) alignments. The data is compared to a MC simulation using a perfect detector geometry (red). The distributions are normalized to the same number of entries.	35
338	4.6	The mean of the local x (left) and local y (right) residual distributions as a function of the global z position of each IBL module using the $\sqrt{s} = 13\text{TeV}$ collision data sample reconstructed using the June (black) and March (green) alignments. The data is compared to a MC simulation using a perfect detector geometry (red).	36
342	4.7	Local x (left) and local y (right) residual distributions for the Pixel barrel (excluding the IBL) using the $\sqrt{s} = 13\text{TeV}$ collision data sample reconstructed using the June (black) and March (green) alignments. The data is compared to a MC simulation using a perfect detector geometry (red). The distributions are normalized to the same number of entries.	37
346	4.8	Local x (left) and local y (right) residual distributions for the Pixel endcaps using the $\sqrt{s} = 13\text{TeV}$ collision data sample reconstructed using the June (black) and March (green) alignments. The data is compared to a MC simulation using a perfect detector geometry (red). The distributions are normalized to the same number of entries.	37
350	4.9	Local x residual distributions for the SCT barrel (left) and end-caps (right) using the $\sqrt{s} = 13\text{TeV}$ collision data sample reconstructed using the June (black) and March (green) alignments. The data is compared to a MC simulation using a perfect detector geometry (red). The distributions are normalized to the same number of entries.	37
354	4.10	Residual distributions for the TRT barrel (left) and end-caps (right) using the $\sqrt{s} = 13\text{TeV}$ collision data sample reconstructed using the June (black) and March (green) alignments. The data is compared to a MC simulation using a perfect detector geometry (red). The distributions are normalized to the same number of entries.	38
358	4.11	Representation of splitting a single cosmic ray track passing through the entire detector (left) into two separate tracks (right).	39
360	4.12	Distribution of the difference in the impact parameter Δd_0 (left) and charge over transverse momentum $\Delta q/p_T$ (right) between the two cosmic ray split tracks. The June (black) and March (green) alignments are compared. The distributions are normalized to the same number of entries.	39
364	4.13	Pull distributions in local x (left) and y (right) for the IBL using the $\sqrt{s} = 13\text{TeV}$ collision data sample after applying the error scaling.	40

366	4.14 Residual means by straw layer in two TRT ϕ -sectors affected by a tilt misalignment. The tilts in each of the three modules are clearly visible in the red points representing the reconstructed data prior to alignment. After four iterations of L2 alignment, the residual means in the gray points are flat.	41
370	4.15 Two dimensional map of residuals in the first layer of the TRT barrel vs z and ϕ . Each bin represents the mean of a Gaussian fit to the TRT residuals in that bin. The map on the left is after the L3 (wire-by-wire) alignment of the TRT performed in 2010, and the map on the right is after the L2 alignment at the end of 2015. The z -axis for both plots use the same scale.	42
375	4.16 Representation of a curl distortion in the detector. The image shows a cutaway in the transverse plane. The deformation is represented by the red arrows, and the impact on the reconstructed positive (blue) and negative (green) tracks are shown. The dashed lines represent the true particle trajectories, and the solid lines represent the reconstructed trajectories.	43
380	4.17 Geometric definition of the sagitta s in relation to the length of the chord l and the radius r of a circular arc.	44
382	4.18 E/p distributions of electrons and positrons in two different $\eta\phi$ bins of the detector. The left hand plot is taken from a region with no momentum bias where $\langle E/p \rangle^+ = \langle E/p \rangle^-$, while the right hand plot shows an 8% disagreement in $\langle E/p \rangle$ between electrons and positrons.	45
386	4.19 Sagitta bias in the $\sqrt{s} = 13\text{TeV}$ data collected by ATLAS in 2016 as a function of η and ϕ for the prompt (left) and reprocessed (right) alignments using the E/p method.	47
388	4.20 Sagitta bias in the $\sqrt{s} = 13\text{TeV}$ data collected by ATLAS in 2016 projected along η for the prompt (gray) and reprocessed (blue) alignments using the E/p method.	47
390	4.21 Sagitta bias in the $\sqrt{s} = 13\text{TeV}$ data collected by ATLAS in 2017 as a function of η and ϕ in reconstructed electrons (left) and after two iterations of momentum corrections (right) from the E/p method.	47
393	4.22 Sagitta bias in the $\sqrt{s} = 13\text{TeV}$ data collected by ATLAS in 2017 projected along η in reconstructed electrons (gray) and after one (red) and two (blue) iterations of momentum corrections from the E/p method.	48
396	5.1 Tree-level Feynman diagrams for VBS EWK $VVjj$ production including triple gauge couplings involving W and/or Z bosons (top left and top middle), quartic gauge coupling (top right), or the exchange of a Higgs boson (s -channel bottom left and t -channel bottom right). The labels are quarks (q), fermions (f), and gauge bosons ($V = W, Z$).	51
400	5.2 Tree-level Feynman diagrams for non-VBS EWK $VVjj$ production. The labels are quarks (q), fermions (f), and gauge bosons ($V = W, Z$).	51
402	5.3 Tree-level Feynman diagrams for QCD $VVjj$ production. The labels are quarks (q), fermions (f), and gauge bosons ($V = W, Z$).	51
404	5.4 Leading order Feynman diagrams for VBS EWK production of $W^\pm W^\pm jj$ events. The leftmost diagram contains a quartic gauge coupling vertex, and the rightmost diagram contains an exchange of a Higgs boson.	53
407	5.5 $W^\pm W^\pm jj$ VBS event topology containing two leptons (1 and 2) with the same electric charge, two neutrinos, and two forward tagging jets (3 and 4) with large rapidity separation Δy	53
410	5.6 Generator level comparisons at $\sqrt{s} = 7\text{TeV}$ of dijet invariant mass (m_{jj} , left) and dijet rapidity (Δy_{jj} , right) in EWK (red) and QCD (blue) $W^\pm W^\pm jj$ events with no selection cuts applied.	54

413	5.7 ATLAS event display of a $pp \rightarrow W^+W^+ \rightarrow \mu^+\nu_\mu\mu^+\nu_\mu jj$ event. The muons are represented by the red lines travelling from the ID through the MS, and the forward jets are represented by the blue cones with yellow energy deposits in the calorimeters. The direction of the E_T^{miss} in the transverse plane is indicated by the gray dashed line in the inset image.	55
418	5.8 Leading lepton p_T (left) and η (right) distributions in the WZ control region before normalization. All lepton channels are combined.	64
420	5.9 Trilepton invariant mass m_{lll} distribution in the WZ control region before normalization. All lepton channels are combined.	65
422	5.10 Charge misidentification rates for electrons as a function of $ \eta $ and p_T . Rates are calculated from $Z \rightarrow e^+e^-$ MC after applying scale factors to approximate the charge mis-ID rates in data.	67
425	5.11 Dilepton invariant mass distribution m_{ll} for the ee channel in the same-sign inclusive VR.	69
426	5.12 p_T distributions for the leading (left) and subleading (right) electron for the ee channel in the same-sign inclusive VR. In these plots, the cut requiring m_{ee} to fall within the Z mass window has been inverted in order to test the modelling away from the Z peak.	70
429	5.13 Graphical representation of how the fake factor method is used to estimate the fake background in a given NN region.	71
431	5.14 Δp_T distributions for nominal (blue) and loose (red) muons in simulated $t\bar{t}$ events. Each muon has been matched to a truth-level jet. Both distributions are normalized to unit area.	73
434	5.15 Δp_T distributions for muons (top) and electrons (bottom) in simulated $t\bar{t}$ events. Each lepton has been matched to a truth-level jet, and that truth jet has had its p_T corrected to include all truth muons within a cone of $\Delta R < 0.4$. The nominal leptons are in black. Δp_T is calculated for the loose leptons using p_T (red) and $p_T + p_T^{\text{cone}}$ (blue).	74
438	5.16 Distributions of p_T^{cone}/p_T for nominal (black) and loose (red) muons in simulated $t\bar{t}$ events.	75
439	5.17 The measured fake-factor as a function of muon $p_T + p_T^{\text{cone}}$. The error bars represent the statistical uncertainty only.	76
441	5.18 The measured fake-factor as a function of electron $p_T + p_T^{\text{cone}}$ in the central ($ \eta < 1.37$, blue) and forward ($ \eta > 1.37$, red) regions of the detector. The error bars represent the statistical uncertainty only.	76
444	5.19 Graphical representation of the fake-factor application using $p_T + p_T^{\text{cone}}$. The value of $p_T + p_T^{\text{cone}}$ for the loose lepton is used to “look up” the fake-factor weight which is then applied to the event. The loose lepton’s p_T becomes $p_T + p_T^{\text{cone}}$ for the purpose of the fake background estimation. TODO: Update figure to match style of Fig. 5.13.	77
448	5.20 Systematic variations in the fake-factor as a function of muon $p_T + p_T^{\text{cone}}$. The individual fake-factors obtained for each systematic variation are displayed with their statistical uncertainties.	80
451	5.21 Systematic variations in the fake-factor as a function of electron $p_T + p_T^{\text{cone}}$ in the central ($ \eta < 1.37$, top) and forward ($ \eta > 1.37$, bottom) regions of the detector. The individual fake-factors obtained for each systematic variation are displayed with their statistical uncertainties.	81
455	5.22 Distributions of the subleading lepton p_T in the same-sign top fakes VR for $\mu^\pm\mu^\pm$ events (top right), $e^\pm e^\pm$ events (top left), $\mu^\pm e^\pm$ events (bottom left), and all events combined (bottom right). All errors are statistical only.	82
458	5.23 Pseudorapidity (η) distributions of truth muons (top) and electrons (bottom) for Sherpa $W^\pm W^\pm jj$ and WZ MC samples. The blue vertical lines represent the allowed η range for each lepton flavor. The numbers correspond to the number of raw MC events that fall within and outside of the allowed η range for each MC sample.	83

462	5.24 Distributions of $p_{T,\text{ratio}}(\mu, j)$ for EWK and QCD $W^\pm W^\pm jj$ signal (black) and WZ background (teal) for truth-matched third muons in events that pass the trilepton veto. Both distributions are normalized to unit area. The associated efficiency curves are on the right where efficiency is defined as the percentage of total events that would pass a cut on $p_{T,\text{ratio}}(\mu, j)$ at a given value on the x -axis.	84
467	5.25 Distributions of $\Delta R(\mu, j)$ for EWK and QCD $W^\pm W^\pm jj$ signal (black) and WZ background (teal) for truth-matched third muons in events that pass the trilepton veto. Both distributions are normalized to unit area. The associated efficiency curves are on the right where efficiency is defined as the percentage of total events that would pass a cut on $\Delta R(\mu, j)$ at a given value on the x -axis.	84
472	5.26 Distributions of $p_{T,\text{ratio}}(e, j)$ for EWK and QCD $W^\pm W^\pm jj$ signal (black) and WZ background (teal) for truth-matched third electrons in events that pass the trilepton veto. Both distributions are normalized to unit area. The associated efficiency curves are on the right where efficiency is defined as the percentage of total events that would pass a cut on $p_{T,\text{ratio}}(e, j)$ at a given value on the x -axis.	85
477	5.27 Two-dimensional plots of $p_{T,\text{ratio}}(\mu, j)$ vs $\Delta R(\mu, j)$ for truth-matched third muons in events that pass the trilepton veto for EWK and QCD $W^\pm W^\pm jj$ signal (left) and WZ background (right). The blue overlay indicates the area in which the third leptons will pass the custom OR and result in the event failing the trilepton veto.	86
481	5.28 Visual representation of the different kinematic regions relevant to the cross section measurement. The acceptance factor \mathcal{A} converts from the truth level total phase space to the truth level fiducial region, and the efficiency correction \mathcal{C} translates the fiducial region into the reconstruction level signal region.	89
485	5.29 The dijet invariant mass m_{jj} distributions for data and predicted signal and background in the signal region after the fit. The shaded band represents the statistical and systematic uncertainties added in quadrature. Note that the bins have been scaled such that they represent the number of events per 100 GeV in m_{jj} . The background estimations from the fake-factor are included in the “Non-prompt” category, and backgrounds from $V\gamma$ production and electron charge misidentification are combined in the “ e/γ conversions” category. Finally, ZZ , VVV , and $t\bar{t}+V$ backgrounds are combined in the “Other prompt” category.	96
493	5.30 The event yields for data and predicted signal and background in the WZ and low- m_{jj} control regions after the fit. The shaded band represents the statistical and systematic uncertainties added in quadrature. The background estimations from the fake-factor are included in the “Non-prompt” category, and backgrounds from $V\gamma$ production and electron charge misidentification are combined in the “ e/γ conversions” category. Finally, ZZ , VVV , and $t\bar{t}V$ backgrounds are combined in the “Other prompt” category.	96
499	5.31 Comparison of the measured $W^\pm W^\pm jj$ EWK fiducial cross section with theoretical calculations from SHERPA v2.2.2 and POWHEG-BOX v2 . The light orange band represents the total experimental uncertainty on the measured value, and the dark orange hashed band is the statistical uncertainty. For the simulations, the light blue band represents the total theoretical uncertainty, and the dark blue hashed band are the scale uncertainties. The theory predictions do not include the interference between the EWK and QCD production.	97
506	6.1 Comparison of the leading (left) and subleading (right) lepton p_T distributions for purely longitudinal (LL, black) and mixed polarization (LT+TT, cyan) $W^\pm W^\pm jj$ events.	100
508	6.2 Comparison of the azimuthal dijet separation ($ \Delta\phi_{jj} $) for purely longitudinal (LL, black) and mixed polarization (LT+TT, cyan) $W^\pm W^\pm jj$ events.	101

510 6.3	A visual representation of a two-dimensional rectangular grid (left) and a random grid (right) in variables x and y . The signal events are the black circles, and the red squares are the background events. Each intersection of gray dashed lines represents a cut point to be evaluated by the optimization.	107
514 6.4	Leading (top) and subleading (bottom) jet p_T distributions. The default and optimized cuts are represented by the red and green dashed lines, respectively. The $W^\pm W^\pm jj$ EWK signal (black points) is normalized to the same area as the sum of the backgrounds (colored histogram).	110
518 6.5	Lepton-jet centrality distribution. The default and optimized cuts are represented by the red and green dashed lines, respectively. The $W^\pm W^\pm jj$ EWK signal (black points) is normalized to the same area as the sum of the backgrounds (colored histogram).	111
521 6.6	p_T distributions for the leading jet using the default (left) and optimized (right) event selections for all channels combined.	112
523 6.7	p_T distributions for the subleading jet using the default (left) and optimized (right) event selections for all channels combined.	112
525 6.8	p_T distributions for lepton-jet centrality ζ using the default (left) and optimized (right) event selections for all channels combined.	113
527 6.9	Projections of the statistical (black), theoretical (blue), systematic (yellow), and total (red) uncertainties on the measured cross section as a function of integrated luminosity using the optimized event selection.	115
530 6.10	Dijet azimuthal separation ($ \Delta\phi_{jj} $) for the low m_{jj} region ($520 < m_{jj} < 1100$ GeV, top) and the high m_{jj} region ($m_{jj} > 1100$ GeV, bottom). The purely longitudinal (LL, gray) is plotted separately from the mixed and transverse (LT+TT, cyan) polarizations.	116
533 6.11	Projections of the expected longitudinal scattering significance as a function of integrated luminosity when considering all sources of uncertainties (black) or only statistical uncertainties (red).	117
536 B.1	Number of truth particles within $\Delta R < 0.4$ of a selected muon or electron using the ATLAS standard TRUTH1 (left) and the custom TRUTH1++ (right) derivations in $t\bar{t}$ simulation. The complete truth record is stored in the TRUTH1++ derivation, and this is best seen in the first bin, where the lepton has no nearby truth particles.	123
540 B.2	Leading lepton p_T distribution. The default and optimized cuts are represented by the red and green dashed lines, respectively. The $W^\pm W^\pm jj$ EWK signal (black points) is normalized to the same area as the sum of the backgrounds (colored histogram).	127
543 B.3	Dilepton invariant mass distribution. The default and optimized cuts are represented by the red and green dashed lines, respectively. The $W^\pm W^\pm jj$ EWK signal (black points) is normalized to the same area as the sum of the backgrounds (colored histogram).	127
546 B.4	Dijet invariant mass distribution. The default and optimized cuts are represented by the red and green dashed lines, respectively. The $W^\pm W^\pm jj$ EWK signal (black points) is normalized to the same area as the sum of the backgrounds (colored histogram).	128

Preface

550 This thesis presents the major highlights of my work with the ATLAS experiment as a graduate
551 student at the University of Pennsylvania from Fall of 2013 until early Spring of 2019.

552 The first step of working on the experiment is to complete a *qualification task* in order to be
553 included on the author list of ATLAS publications. These tasks are an opportunity to contribute
554 to the experiment as a whole, such as maintaining detector hardware or monitoring physics perfor-
555 mance. For my qualification task, I worked with the Inner Detector Alignment group which works
556 to make sure we have accurate knowledge of the locations of each and every sensor in the tracking
557 detector. My qualification task involved investigating a possible momentum bias in the Monte Carlo
558 (MC) simulated data. The MC is supposed to be reconstructed with a perfect detector geometry
559 which should in principle be free of any momentum biases. Ultimately I determined that the size of
560 the biases were small enough to be negligible compared to what is seen in the real data, and that
561 they could be corrected for if necessary.

562 My work with the alignment group would continue for the duration of my time here at Penn. In
563 early 2015, at the start of the LHC’s second data-taking run (Run 2), I assisted with the validation
564 of the first set of alignment constants using $\sqrt{s} = 13$ TeV proton-proton collision data. At this point
565 I took over the responsibility of alignment of the TRT subdetector. The TRT was aligned to high
566 accuracy in Run 1, and over the course of my time working on alignment, the TRT never required
567 a straw-by-straw alignment; however it did require a module-level alignment at the end of 2015.
568 My final responsibility in the alignment group was monitoring momentum biases using the energy-
569 momentum ratio (E/p) of electrons. For the large data reprocessing, the E/p method served as a
570 cross check to a similar method using Z boson events for monitoring and aligning out momentum
571 biases in the detector. The results from both methods were also used in the uncertainties for the
572 tracking measurements.

573 On the analysis side, I had previous experience in Standard Model (SM) electroweak physics
574 from my time as an undergraduate at Duke University, and it remained a point of interest for
575 me in graduate school. As such, I was happy to work with fellow Penn students on the cross
576 section measurement of SM WZ diboson production with the early $\sqrt{s} = 13$ TeV ATLAS data.
577 My contribution to the analysis was primarily on the software side, as I maintained and updated
578 the analysis framework. While the WZ measurement is not covered by this thesis, it provided me
579 with invaluable analysis experience in electroweak physics, as well as a detailed understanding of a
580 major background to many diboson processes. The results for this analysis can be found published
581 in Physics Letters B in 2016 [2].

582 The final two analyses I worked on involved the scattering of same-sign W bosons, and they make
583 up the majority of this thesis. The first analysis is a measurement of the $W^\pm W^\pm jj$ cross section
584 at $\sqrt{s} = 13$ TeV. This measurement along with that of the CMS collaboration represent the first
585 observation of the $W^\pm W^\pm jj$ scattering process. My primary contribution to the analysis is in the
586 estimation of the fake lepton background, where we implemented a brand new version of the fake-
587 factor method using particle isolation variables. I also did a preliminary study of the interference
588 between electroweak and strong production of $W^\pm W^\pm jj$ events, assisted in the production of data
589 samples for use with the analysis framework, and used my familiarity with the WZ process to
590 optimize the rejection of this background. Ultimately the results of this optimization were not
591 included in the final result; however, it is still covered in the thesis in the hopes that it will be useful
592 for similar analyses in the future. The formal publication for this measurement will likely be coming
593 out within the next few months.

594 The second $W^\pm W^\pm jj$ analysis is a study on the prospects for a measurement of the process at the
595 upgraded High-Luminosity LHC, scheduled to begin operation in 2026. Here my main contribution
596 was an optimization of the event selection using a Random Grid Search algorithm. Through the
597 optimization we expect to take advantage of the higher center of mass energy and greater volume of
598 data and tighten certain selection cuts to increase the strength of the $W^\pm W^\pm jj$ signal. In addition, I
599 once again maintained and updated the analysis framework and produced the group's data samples,
600 and I also developed a truth-based particle isolation criteria in order to reduce contributions from
601 backgrounds involving the top quark. The results of this prospects study will be published as a part
602 of the annual Yellow Report for the High-Luminosity LHC.

603

Will K. DiClemente
Philadelphia, February 2019

CHAPTER 1

Introduction

606 The Large Hadron Collider (LHC) at CERN is the most powerful collider experiment in the world.
607 At the time of its construction, the largest unanswered question in the Standard Model (SM) was
608 the mechanism behind electroweak symmetry breaking (EWSB). As a result, one of the primary
609 goals of the experiment is to learn as much as possible about this mechanism. Thus far, the LHC
610 has succeeded in discovering a particle consistent with the long-awaited Higgs boson. In addition,
611 measurements of many SM processes have been performed for the first time or at better precision
612 than before thanks to the high collision energy and large volume of data collected by the LHC.

613 Processes involving the scattering of two massive electroweak (EWK) gauge bosons are of par-
614 ticular interest at the LHC for two main reasons. Firstly, they allow for tests of the self-interactions
615 predicted by the EWK gauge theory through triple and quartic gauge couplings. While the triple
616 couplings have been studied by previous experiments as well as at the LHC, the quartic couplings
617 of the massive gauge bosons have not been accessible previously. Thus, processes involving these
618 couplings can be measured and compared to the SM predictions for the first time. Secondly, the scat-
619 tering of two massive gauge bosons is sensitive to the underlying EWSB mechanism. The W^\pm and
620 Z bosons are given non-zero masses—and consequently a longitudinal polarization mode—through
621 the Higgs mechanism, and thus their interactions serve as a direct probe of the symmetry breaking
622 sector.

623 This thesis presents two separate analyses dealing with the scattering of two same-sign W^\pm
624 bosons with the LHC’s ATLAS experiment. The $W^\pm W^\pm jj$ process is one of the most sensitive to the
625 goals above: it has access to the $WWWW$ quartic gauge coupling, production modes that involve the
626 exchange of a Higgs boson, and relatively low backgrounds. Evidence of EWK $W^\pm W^\pm jj$ production
627 was first seen by the ATLAS and CMS experiments at $\sqrt{s} = 8$ TeV, however the data set was too

628 small to claim observation of the process. The first analysis covered here is the follow up to the above
629 ATLAS measurement, measuring the EWK fiducial cross section at $\sqrt{s} = 13$ TeV with a larger data
630 sample. The second analysis explores the prospects for future measurements of the $W^\pm W^\pm jj$ process
631 at the planned High-Luminosity LHC (HL-LHC). A measurement of the production cross section
632 as well as sensitivity to the purely longitudinal component of the $W^\pm W^\pm$ scattering is presented.

633 In addition to the SM measurements, a part of this thesis is devoted to alignment of the detector
634 components making up ATLAS’s Inner Detector (ID). Precise knowledge of the locations of detector
635 elements is essential for accurate particle track reconstruction, which in turn results in improved
636 resolutions for physics measurements. The ATLAS alignment algorithm determines the positions
637 of each ID sensor through minimizing the distance between reconstructed particle tracks and the
638 sensor hit position. Special emphasis is given to the monitoring of momentum biases that may exist
639 in the ID even after alignment.

640 This first few chapters of this thesis are intended to provide context for the main topics. Chapter 2
641 gives a brief introduction to the Standard Model with a focus on the mechanism of electroweak
642 symmetry breaking and vector boson scattering. The experimental apparatus—the LHC and the
643 ATLAS detector—are detailed in Chapter 3. The next three chapters present the main body of
644 work. Chapter 4 covers the alignment of the ATLAS Inner Detector. Finally, Chapters 5 and
645 6 detail the ATLAS $\sqrt{s} = 13$ TeV $W^\pm W^\pm jj$ cross section measurement and the $\sqrt{s} = 14$ TeV
646 HL-LHC $W^\pm W^\pm jj$ prospects study, respectively.

CHAPTER 2

Theoretical Framework

649 This chapter outlines the theoretical groundwork for the rest of the thesis. An overview of the Stan-
 650 dard Model of particle physics (SM) is given in Section 2.1, followed by the electroweak symmetry
 651 breaking mechanism involving the Higgs boson in Section 2.2. Finally, Section 2.3 will go into detail
 652 on the interests of electroweak vector boson scattering (VBS).

653 **2.1 Introduction to the Standard Model**

654 The Standard Model of particle physics serves as a mathematical description of the fundamental
 655 particles of the universe and their interactions. It has been developed over the course of the past
 656 century, incorporating both predictions from theory and results from experiments. All in all, the
 657 SM has proven to be very accurate in describing the particle interactions seen in experiments, as can
 658 be seen in the summary plot of ATLAS standard model measurements through 2018 in Figure 2.1.

659 The SM is a quantum field theory (QFT) [4, 5] in which the fundamental particles are represented
 660 as excited states of their corresponding fields. The spin- $\frac{1}{2}$ fermionic fields give rise to the quarks
 661 and leptons comprising ordinary matter, the spin-1 fields correspond to the electroweak bosons and
 662 the gluon which mediate the electroweak and strong forces, respectively, and finally the scalar Higgs
 663 field is responsible for electroweak symmetry breaking. The excitations and interactions of the fields
 664 are governed by the SM Lagrangian, which is invariant under local transformations of the group
 665 $SU(3) \times SU(2) \times U(1)$.

666 The first quantum field theory to be developed was quantum electrodynamics (QED) [6], which
 667 describes the electromagnetic interaction. The theory predicts the existence of a $U(1)$ gauge field
 668 that interacts with the electrically charged fermions. This field corresponds to the photon. A key

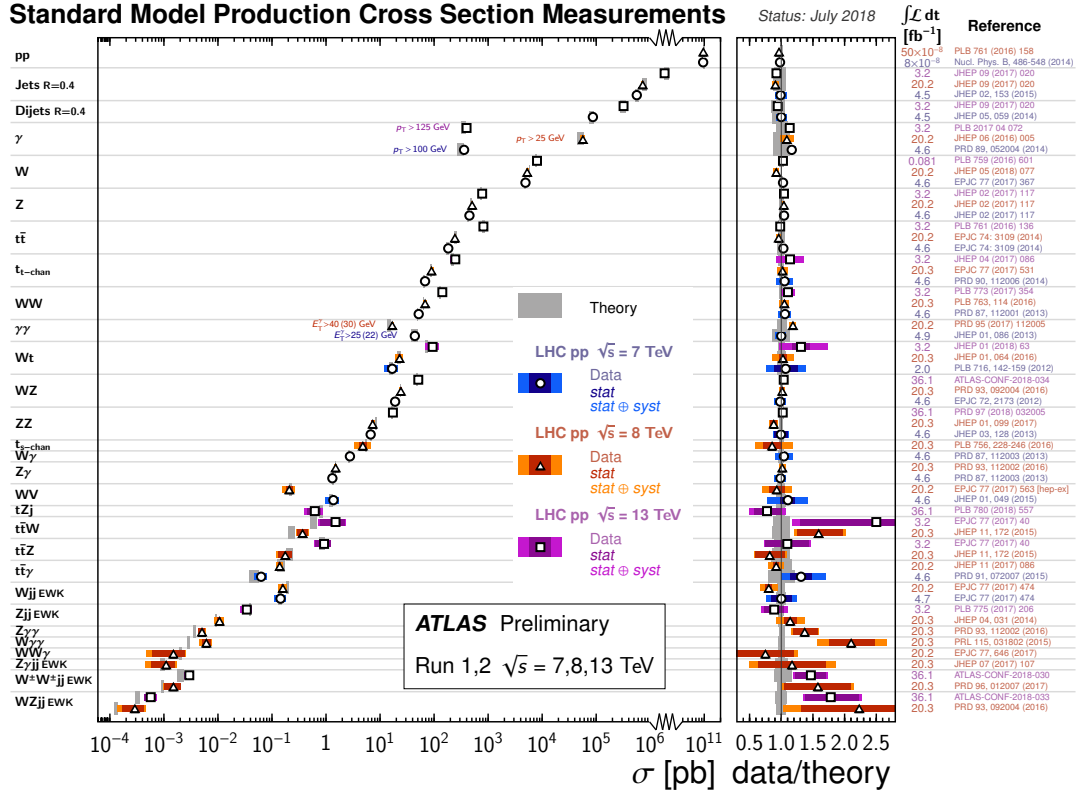


Figure 2.1: Summary of several Standard Model total and fiducial production cross section measurements compared to the corresponding theoretical predictions calculated at NLO or higher. The dark colored error bar represents the statistical uncertainty, and the light colored error bar represents the full uncertainty (including systematic and luminosity uncertainties). The data/theory ratio, luminosity used and reference for each measurement are also shown [3].

aspect of QED is that it is perturbative. The coupling constant $\alpha = e^2/4\pi$ is small, where e is electrical charge of the field, allowing for the use of perturbation theory in calculations. In this case, calculations can be written as a power series in α , where successive higher order terms contribute less to the final result. The accuracy of perturbative calculations is an essential tool for being able to make predictions from the SM.

The strong interaction—the theory of quarks and gluons—has also been described using QFT as quantum chromodynamics (QCD). The symmetry group for QCD is $SU(3)$, and its eight generators correspond to the eight differently charged, massless gluons [7]. Unlike in QED, which has positive and negative charges, the strong force has three “colors”. Color charge combined with the non-Abelian nature of $SU(3)$, which allows the gluons to interact with each other, result in the

most well-known property of QCD: color confinement. In order to increase the separation between two color-charged quarks, the amount of energy required increases until it becomes energetically favorable to pair-produce a new quark-antiquark pair, which then bind to the original quarks. The end result of this is that only color-neutral objects exist in isolation. What this means for the strong coupling constant α_s is that its value at the low energies where confinement occurs is large, on the order of $\alpha_s \sim 1$. The consequence of this is that perturbation theory cannot be used to accurately approximate interactions. While this appears at first to be a critical problem for predictions, fortunately it turns out that α_s “runs”, or decreases in magnitude at higher energy [8, 9]. This so-called “asymptotic freedom” allows QCD to be calculated perturbatively [10] at energies accessible by collider experiments including the LHC.

The last gauge field corresponds to the weak interaction. Ultimately, the weak $SU(2)$ and the electromagnetic $U(1)$ mix to form the $SU(2) \times U(1)$ *electroweak* (EWK) interaction [11, 12]. A more detailed description of the mixing will be discussed in conjunction with electroweak symmetry breaking (EWSB) in Section 2.2; however, a summary of the resulting EWK interaction is presented here, at the risk of some repeated information to follow. There are three weak isospin bosons arising from the $SU(2)$ group (W_μ^1 , W_μ^2 , and W_μ^3) and one weak hypercharge boson from the $U(1)$ group (B_μ). The W_3 and B bosons mix according to the weak mixing angle θ_W to form the Z boson and the photon according to:

$$\begin{pmatrix} \gamma \\ Z \end{pmatrix} = \begin{pmatrix} \cos \theta_W & \sin \theta_W \\ -\sin \theta_W & \cos \theta_W \end{pmatrix} \begin{pmatrix} B_\mu \\ W_\mu^3 \end{pmatrix} \quad (2.1)$$

The value of θ_W is not predicted by the SM; it is one example of an experimental input to the theory, measured to be $\sin^2 \theta_W = 0.23153 \pm 0.00016$ [13]. The charged W^\pm bosons are a mixture of the remaining W_μ^1 and W_μ^2 bosons:

$$W^\pm = \frac{1}{\sqrt{2}}(W_\mu^1 \mp iW_\mu^2) \quad (2.2)$$

Unlike the photon (and the gluon of QCD), the W^\pm and Z bosons are massive. This means that even though $SU(2)$ is non-Abelian, the range of interaction is short and confinement does not occur. Lastly, the EWK interaction is chiral, only coupling to the left-handed component of the fermion fields.

One final field remains within the SM: the scalar Higgs field. It was originally proposed in the 1960’s to explain the masses of the W^\pm and Z bosons [14, 15, 16] and is the mechanism for the EWSB process. The particle associated with the field is a massive scalar boson, the Higgs boson, which was recently discovered by ATLAS and CMS in 2012 [17, 18] with a mass of 125 GeV.

708 **2.2 Electroweak symmetry breaking and the Higgs boson**

709 The results of electroweak mixing and the implications of the Higgs field have been introduced
 710 in the previous section. If the EWK theory were an unbroken symmetry, the associated W^\pm and
 711 Z bosons would be massless; however, when observed experimentally, they were found to be quite
 712 heavy [19, 20], at around 80 GeV and 91 GeV, respectively [21]. Here, a more detailed explanation
 713 of the Higgs mechanism and how it “spontaneously breaks” the EWK symmetry, resulting in the
 714 three massive bosons (W^\pm and Z) and one massless boson (photon), is presented.

715 To see how the Higgs mechanism results in the massive vector bosons and a massless photon,
 716 consider the following. Beginning with a complex scalar doublet ϕ defined as:

$$\phi = \begin{pmatrix} \phi^+ \\ \phi^0 \end{pmatrix} = \sqrt{\frac{1}{2}} \begin{pmatrix} \phi_1 + i\phi_2 \\ \phi_3 + i\phi_4 \end{pmatrix} \quad (2.3)$$

717 a Lagrangian \mathcal{L} can be written:

$$\mathcal{L} = (\mathcal{D}_\mu \phi)^\dagger (\mathcal{D}^\mu \phi) - \mu^2 \phi^\dagger \phi - \lambda(\phi^\dagger \phi)^2 \quad (2.4)$$

718 where $\lambda > 0$ and \mathcal{D}_μ is the covariant derivative defined such that \mathcal{L} is invariant under a local
 719 $SU(2) \times U(1)$ gauge transformation:

$$\mathcal{D}_\mu \phi = \left(\partial_\mu + \frac{ig}{2} \tau_a W_\mu^a + \frac{ig'}{2} B_\mu \right) \phi \quad (2.5)$$

720 Here W_μ^a ($a = 1, 2, 3$) are the $SU(2)$ fields with generators τ_a and coupling constant g , and B_μ is the
 721 $U(1)$ field with coupling constant g' .

722 Isolating the potential term of the Lagrangian:

$$V(\phi) = \mu^2 \phi^\dagger \phi + \lambda(\phi^\dagger \phi)^2 \quad (2.6)$$

723 a choice must be made on the sign of μ^2 , and the case of interest is for $\mu^2 < 0$. This results in
 724 the famous “Mexican hat potential” shown in Figure 2.2, which is minimized along the collection of
 725 points:

$$\phi^\dagger \phi = \frac{1}{2} (\phi_1^2 + \phi_2^2 + \phi_3^2 + \phi_4^2) = -\frac{\mu^2}{2\lambda} \quad (2.7)$$

726 This means that the minimum of the potential is not at $\phi = 0$ (as it would be in the case where
 727 $\mu^2 > 0$), but rather at a value:

$$v \equiv \sqrt{-\frac{\mu^2}{\lambda}} \quad (2.8)$$

728 With no loss of generality due to the SU(2) symmetry, $\phi_1 = \phi_2 = \phi_4 = 0$ can be imposed on
 729 Equation 2.7 leaving $\phi_3^2 = v^2$. Finally, the *vacuum expectation value* (VEV) of the field can be
 730 written as:

$$\langle \phi \rangle = \sqrt{\frac{1}{2}} \begin{pmatrix} 0 \\ v \end{pmatrix} \quad (2.9)$$

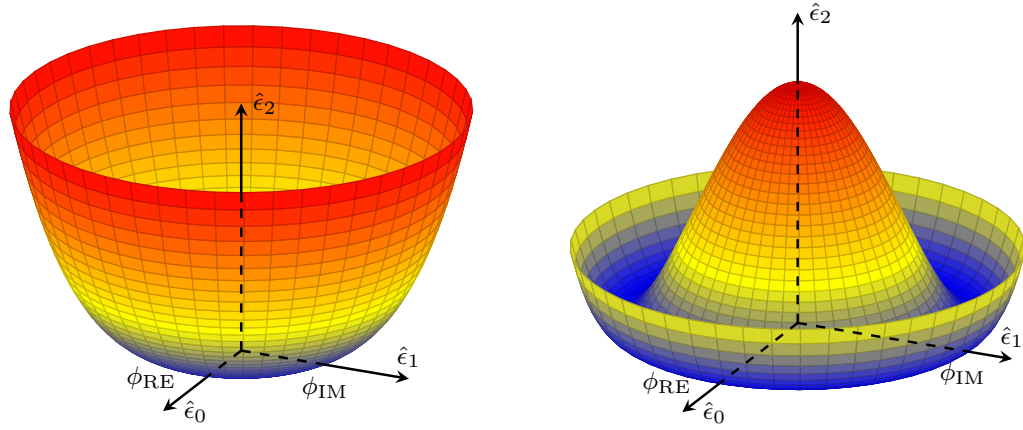


Figure 2.2: An illustration of the potential term $V(\phi)$ in Equation 2.6 for the cases where $\mu^2 > 0$ (left) and $\mu^2 < 0$ (right). The right-hand plot shows the Higgs potential, or ‘Mexican hat potential’, with the minimum at $|\phi| = \sqrt{-\frac{\mu^2}{\lambda}}$ rather than at $|\phi| = 0$ as in the left-hand plot.

731 The VEV can be substituted back into the original Lagrangian in Equation 2.4, and, following
 732 quite a bit of math, a collection of mass terms can be identified:

$$\mathcal{L} \subset \mathcal{L}_M \equiv \frac{1}{8}v^2g^2 \left[(W_\mu^1)^2 + (W_\mu^2)^2 \right] + \frac{1}{8}v^2 \left[g^2(W_\mu^3)^2 - 2gg'W_\mu^3B^\mu + g'^2(B_\mu)^2 \right] \quad (2.10)$$

733 Focusing on the first term for the moment, if Equation 2.2 for the physical W^\pm bosons is substituted
 734 in, the mass term can be seen clearly:

$$M_W^2 W^+ W^- = \left(\frac{1}{2}vg \right)^2 W^+ W^- \quad (2.11)$$

735

$$M_W = \frac{1}{2}vg \quad (2.12)$$

736 With a bit of clever forward-thinking, the second term of Equation 2.10 can be rewritten as:

$$\frac{1}{8}v^2 \left[gW_\mu^3 - g'B_\mu \right]^2 + 0 \left[g'W_\mu^3 - gB_\mu \right]^2 = \frac{1}{2}M_Z^2 Z_\mu^2 + \frac{1}{2}M_A^2 A_\mu^2 \quad (2.13)$$

737 where Z_μ^2 and A_μ^2 represent the physical Z boson and photon, respectively, and are defined as:

$$Z_\mu = \frac{gW_\mu^3 - g'B_\mu}{\sqrt{g^2 + g'^2}} \quad (2.14)$$

738

$$A_\mu = \frac{g'W_\mu^3 - gB_\mu}{\sqrt{g^2 + g'^2}} \quad (2.15)$$

739 From this, it can be seen that the photon is massless ($M_A = 0$ in Equation 2.13), and the mass of
740 the Z boson is identified as:

$$M_Z = \frac{1}{2}v\sqrt{g^2 + g'^2} \quad (2.16)$$

741 Lastly, the Higgs field can couple directly to the fermions. Taking the electron as an example,
742 an additional Lagrangian term can be written:

$$\mathcal{L}_e = -G_e[\bar{e}_L\phi e_R + \bar{e}_R\phi^\dagger e_L] \quad (2.17)$$

743 where e_L and e_R are the left-handed doublet and right-handed singlet, respectively, and ϕ is as in
744 Equation 2.3. The symmetry can be spontaneously broken by a perturbation about the VEV:

$$\phi = \sqrt{\frac{1}{2}} \begin{pmatrix} 0 \\ v + h(x) \end{pmatrix} \quad (2.18)$$

745 which, when substituted into \mathcal{L}_e gives:

$$\begin{aligned} \mathcal{L}_e &= -\frac{G_e}{\sqrt{2}}v(\bar{e}_L e_R + \bar{e}_R e_L) - \frac{G_e}{\sqrt{2}}(\bar{e}_L e_R + \bar{e}_R e_L)h \\ &= -m_e \bar{e}e - \frac{m_e}{v} \bar{e}eh \end{aligned} \quad (2.19)$$

746 for electron mass $m_e = \frac{G_e v}{\sqrt{2}}$. From the second term, it can be seen that the strength of the Higgs
747 coupling to the electron is proportional to the mass of the electron. The rest of the fermion couplings
748 follow from this example.

749 What is accomplished here is quite remarkable. The weak and electromagnetic interactions have
750 been unified into a single $SU(2) \times U(1)$ interaction, and the physical bosons observed in nature
751 arise as mixtures of the four gauge fields. Three of the four degrees of freedom in the scalar field
752 ϕ of Equation 2.3, are absorbed (or “eaten”) by the W^\pm and Z bosons, and the fourth generates
753 the Higgs boson. Additionally, it is shown that the Higgs couples to fermions in proportion to
754 their mass. From experimental measurements, the value of the VEV has been determined to be
755 $v \approx 246$ GeV [21]. However, it should be noted that the theory does not predict the mass of the
756 Higgs boson or of the fermions; these must all be determined from experiment.

⁷⁵⁷ **2.3 Electroweak vector boson scattering**

⁷⁵⁸ Due to the non-Abelian nature of the EWK interaction, the associated gauge bosons are allowed
⁷⁵⁹ to self-interact. This results in triple and quartic couplings of gauge bosons (TGCs and QGCs,
⁷⁶⁰ respectively). The SM allowed TGCs are the $WW\gamma$ and WWZ vertices, which can be measured
⁷⁶¹ experimentally via diboson production or through vector boson fusion (VBF). QGCs predicted by the
⁷⁶² model include $WWZ\gamma$, $WW\gamma\gamma$, $WWZZ$, and $WWWW$ vertices accessible in triboson production
⁷⁶³ or via vector boson scattering (VBS)¹ [22]. VBS processes are defined by a $VV \rightarrow VV$ signature,
⁷⁶⁴ where V represents one of the EWK gauge bosons (W^\pm , Z , or γ), as shown in Figure 2.3. The actual
⁷⁶⁵ interaction between the incoming and outgoing vector bosons can be mediated by the exchange of
⁷⁶⁶ a virtual V , directly via a QGC (as in Figure 2.4), or by the exchange of a Higgs boson (as in
⁷⁶⁷ Figure 2.5).

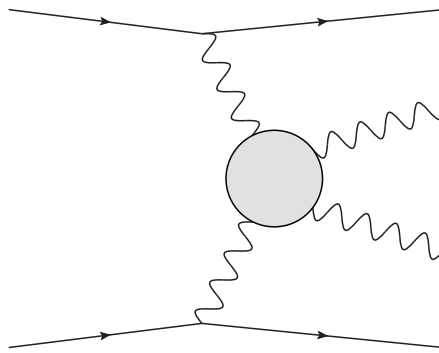


Figure 2.3: Feynman diagram of a generic VBS process. The gray circle represents any interaction with two incoming and two outgoing vector bosons, including any of the diagrams shown in Figures 2.4 and 2.5.

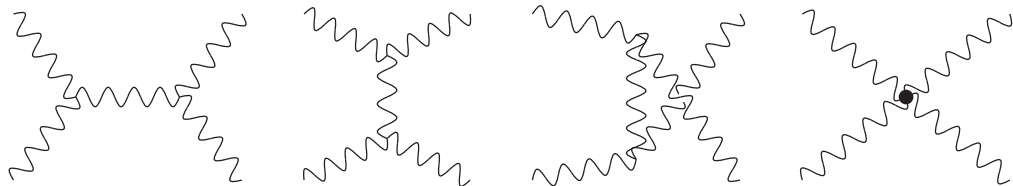


Figure 2.4: Leading order $VV \rightarrow VV$ Feynman diagrams involving EWK bosons. From left to right: s -channel, t -channel, u -channel, and the quartic gauge coupling.

¹Vector boson fusion and scattering typically refer to the s -channel and t -channel exchanges of a vector boson, respectively. Since both deal with a similar $VV \rightarrow VV$ process, for the remainder of this thesis, *vector boson scattering* will refer to both VBF and VBS.

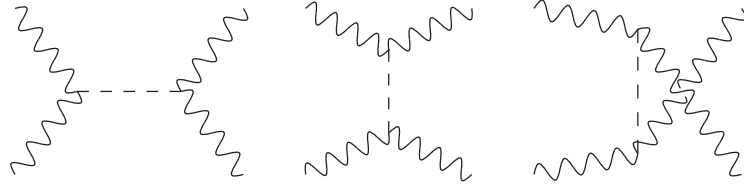


Figure 2.5: Leading order $VV \rightarrow VV$ Feynman diagrams involving the exchange of a Higgs boson. From left to right: s -channel, t -channel, and u -channel.

As detailed in the previous section, the Higgs mechanism produces three Goldstone bosons and a Higgs boson. The Goldstone bosons are then “eaten” by the physical gauge bosons, giving them mass and consequently a longitudinal polarization². In fact, according to the Electroweak Equivalence Theorem, the high-energy interactions of longitudinal gauge bosons can be accurately described by the Goldstone bosons of the EWSB mechanism [23]. Thus, the scattering of the massive gauge bosons are inextricably linked to EWSB.

It turns out that without a light SM Higgs boson, the scattering amplitude of longitudinally polarized vector bosons grows with center-of-mass energy and ultimately violates unitarity above $\sqrt{s} \approx 1.2$ TeV [24, 25]. Writing down the equations for the transverse and longitudinal polarization vectors for a gauge boson of mass M_V [26]:

$$\epsilon_{\pm}^{\mu} = \frac{1}{\sqrt{2}}(0, 0, \pm i, 0) \quad (2.20)$$

where v^{μ} is of the order M_V/E and becomes small in the high energy limit, it can be seen that ϵ_L^{μ} grows with the momentum of the boson p^{μ} . Therefore, the dominant contribution to the VBS process at high energy comes from the longitudinally polarized gauge bosons [27].

The high-energy behavior of longitudinally polarized vector boson scattering can be explored in the case of opposite-sign $W^+W^- \rightarrow W^+W^-$ scattering. In the high-energy limit ($s \gg M_W^2, M_H^2$), the amplitude of W^+W^- scattering without considering the Higgs contributions (the relevant diagrams in Figure 2.4) can be written as [25]:

$$\mathcal{M}_{\text{gauge}} = -\frac{g^2}{4M_W^2}u + \mathcal{O}\left(\left[\frac{E}{M_W}\right]^0\right) \quad (2.22)$$

²A massless spin-1 boson can have one of two transverse polarization states, while a massive spin-1 boson can also be longitudinally polarized. As a result, only the massive W^{\pm} and Z bosons, and not the massless photon, are sensitive to EWSB.

where g is the EWK coupling and u is one of the Mandelstam variables (the others being s and t). The $\mathcal{O}(E^4)$ terms cancel out between the TGC and QGC diagrams [27]. What is left is an amplitude proportional to E^2 that diverges as $E/M_W \rightarrow \infty$. However, the amplitude from the diagrams involving the Higgs boson (the relevant diagrams in Figure 2.5) is:

$$\mathcal{M}_{\text{Higgs}} = -\frac{g^2}{4M_W^2} \left[\frac{(s - M_W^2)^2}{s - m_H^2} + \frac{(t - M_W^2)^2}{t - M_H^2} \right] \quad (2.23)$$

which, in the high-energy limit, reduces to:

$$\mathcal{M}_{\text{Higgs}} = \frac{g^2}{4M_W^2} u + \mathcal{O}\left(\left[\frac{E}{M_W}\right]^0\right) \quad (2.24)$$

Adding the two equations together cancels out the E^2 term and leaves only terms constant in energy. Therefore, with a SM Higgs, the scattering amplitude for longitudinally polarized W bosons no longer diverges. Plots of the cross section of several $VV \rightarrow VV$ scattering processes are shown in Figure 2.6 with and without a SM Higgs boson.

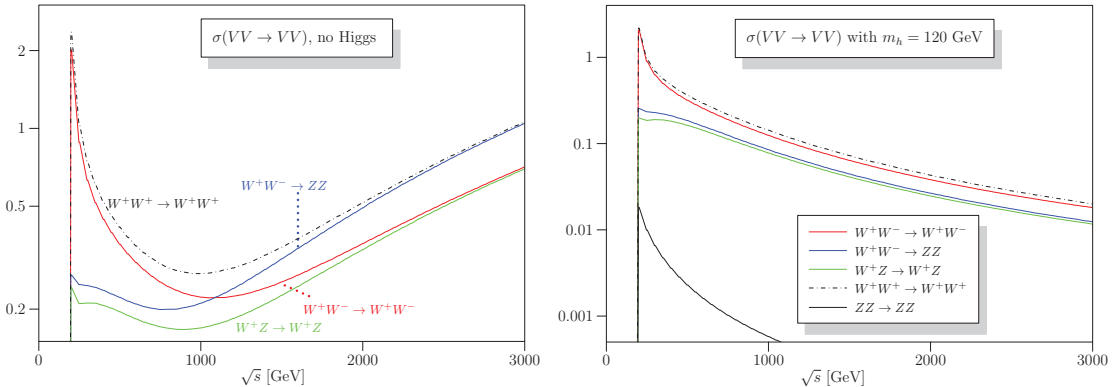


Figure 2.6: Cross sections in nanobarns for five different longitudinally polarized VBS processes as a function of center of mass energy \sqrt{s} . Without a Higgs boson (left), the cross sections grow unbounded with \sqrt{s} . With a 120 GeV Higgs boson (right), the cross sections no longer diverge. Plots taken from [28].

CHAPTER 3

LHC and the ATLAS Detector

This chapter covers the experimental apparatus relevant to this thesis: the Large Hadron Collider (LHC) and the ATLAS detector in Sections 3.1 and 3.2, respectively. Some time is taken to overview the methods used to identify and measure various particle types within ATLAS in Section 3.2.4.

3.1 The Large Hadron Collider

The Large Hadron Collider (LHC) [29] is the most powerful particle accelerator in the world in terms of beam energy, colliding two beams of protons at a center of mass energy of $\sqrt{s} = 13$ TeV. It is operated by the European Organization for Nuclear Research (CERN), and the collider is located beneath the France–Switzerland border. The LHC itself consists of a 27 km ring in which the collisions occur, and it is the last piece in a chain of several smaller accelerators that begin boosting the protons³ to high energies. Collisions occur at each of four detector experiments situated around the ring: ATLAS [30], ALICE [31], CMS [32], and LHCb [33].

Protons are obtained from hydrogen atoms stripped of their electrons by an electric field. A beam of protons is first accelerated up to 50 MeV in the Linac 2 accelerator, then to 1.4 GeV in the Proton Synchrotron Booster (PSB), 25 GeV in the Proton Synchrotron (PS), and finally to 450 GeV in the Super Proton Synchrotron (SPS). The protons are now injected into the LHC ring in two beams running in opposite directions where they each accelerate up to the collision energy of 6.5 TeV. The beams consist of bunches containing on the order of 10^{11} protons separated by 25 ns [34]. A schematic of the CERN accelerator complex, including the chain of accelerators mentioned above, is shown in Figure 3.1.

³The LHC can also collide beams of heavy ions; however, this thesis focuses exclusively on the proton-proton collisions.

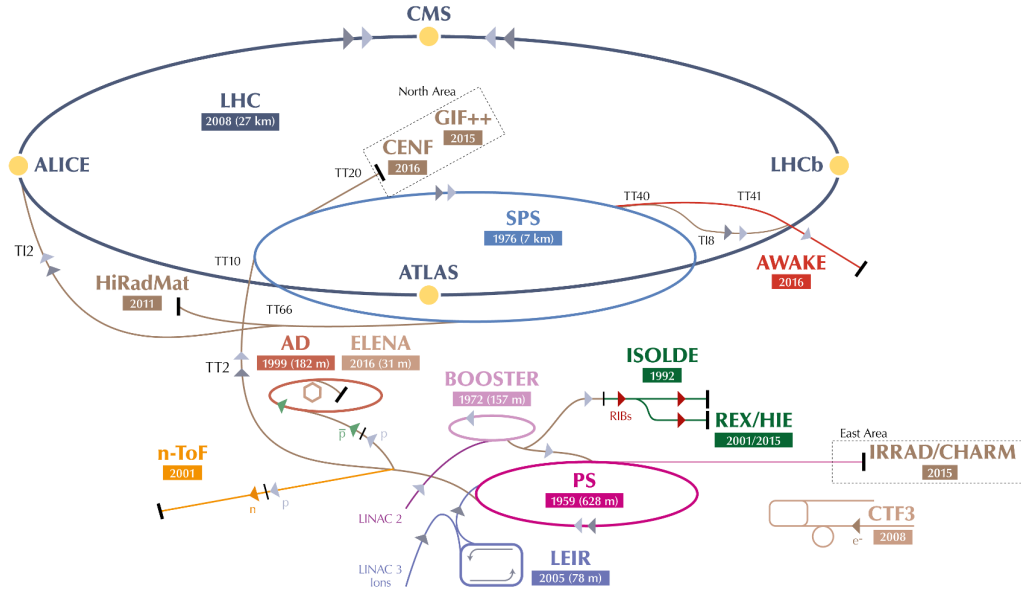


Figure 3.1: The CERN accelerator complex. For LHC collisions, protons are accelerated in the PSB (purple), the PS (magenta), and the SPS (light blue) before entering the LHC ring (dark blue) [35].

In addition to a high center of mass energy, the LHC must also deliver enough data to measure rare processes. The amount of data collected is measured in terms of *luminosity*. The instantaneous luminosity \mathcal{L} is defined in terms of the number of events per second $\frac{dR}{dt}$ and the production cross section σ_p :

$$\mathcal{L} = \frac{1}{\sigma_p} \frac{dR}{dt} \quad (3.1)$$

The calculation itself can be quite tricky, as it depends on a number of factors including (but not limited to) the number of particles per bunch, the spread of the beam, and the crossing angle of the beam [36].

The LHC was originally designed to operate at an instantaneous luminosity of $1.0 \times 10^{34} \text{ cm}^{-2}\text{s}^{-1}$; however, this number was exceeded by the end of the 2016 data taking period, with a peak luminosity of $1.38 \times 10^{34} \text{ cm}^{-2}\text{s}^{-1}$. This number has been more than doubled by the end of Run 2 in December of 2018 [37]. The instantaneous luminosity of pp collisions as a function of time in 2015 and 2016 are shown in Figure 3.2. The integrated luminosity is then the time integral of the instantaneous luminosity. By the end of Run 2 (2015-2018), approximately 140 fb^{-1} of 13 TeV data is available for physics, as shown in Figure 3.3. The 36.1 fb^{-1} collected during the first two years (2015 and 2016) is used for the analysis later in this thesis.

Due to the high instantaneous luminosity, more than one pp interaction occurs in a single bunch

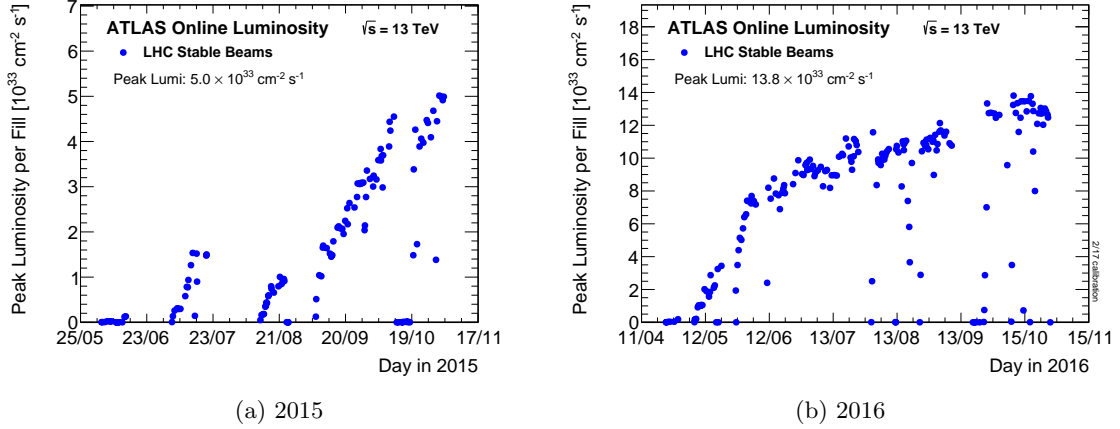


Figure 3.2: Peak instantaneous luminosity delivered to ATLAS during 13 TeV pp data taking as a function of time [37].

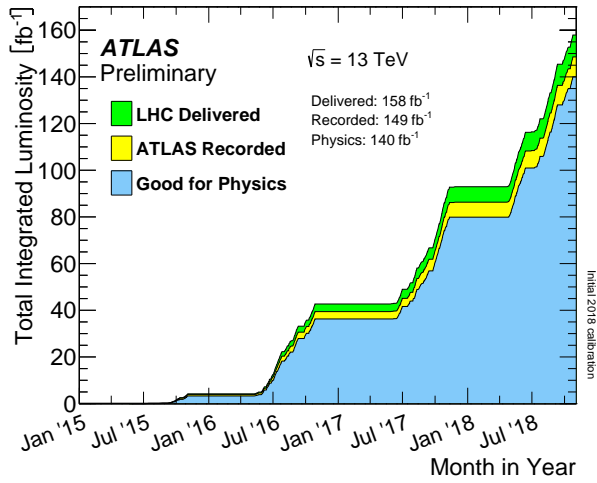


Figure 3.3: Integrated luminosity collected by ATLAS as a function of time at 13 TeV from 2015-2018 [37].

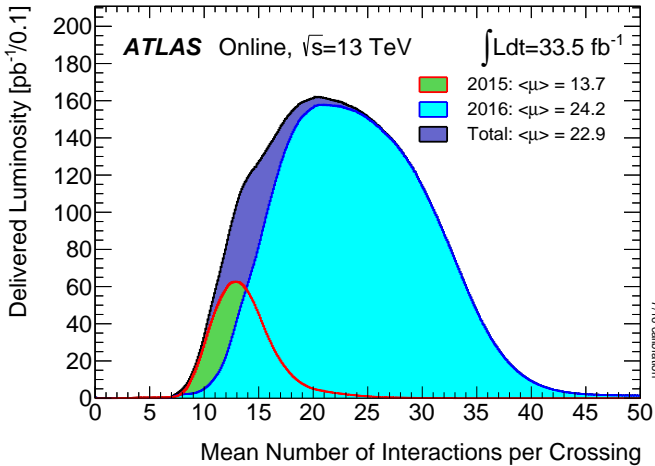


Figure 3.4: Distribution of the mean number of interactions per bunch crossing for the 2015 and 2016 pp collision data at 13 TeV [37].

crossing, referred to as *pileup*. During the 2016 data taking campaign, the average number of interactions per bunch crossing $\langle \mu \rangle$ was approximately 24 but has increased to upwards of 37 in 2017 and 2018 [37]. Figure 3.4 contains the average μ for the 2015–2016 data set used for analysis in this thesis. The high pileup is a challenge for accurately reconstructing an individual collision.

3.2 The ATLAS Detector

ATLAS (A Toroidal LHC ApparatuS) is a general-purpose particle detector. It is made up of several different subdetector systems designed to measure different types of particles. Starting from the beam line and working outwards, the Pixel Detector (PIX), Semiconductor Tracker (SCT), and Transition Radiation Tracker (TRT) make up the Inner Detector (ID) and are responsible for measuring the trajectories and momenta of charged particles. Next are two calorimeters: the Liquid Argon Calorimeter (LAr) stops electromagnetic objects and measures their energies, and the Tile Calorimeter (TileCal) does the same for hadronic objects. Finally, the outermost Muon Spectrometer (MS) measures muon tracks as they leave the detector, as they are not stopped in the calorimeters. The ATLAS detector and its subsystems are shown in Figure 3.5.

ATLAS uses a global, right-handed coordinate system with the origin at the center of the detector (the nominal interaction point). The x -axis points from the origin inwards to the center of the LHC ring, the y -axis points upwards, and the z -axis points along the beam line. Due to the azimuthal symmetry of the detector, it is useful to use cylindrical coordinates (r, ϕ) in the plane transverse

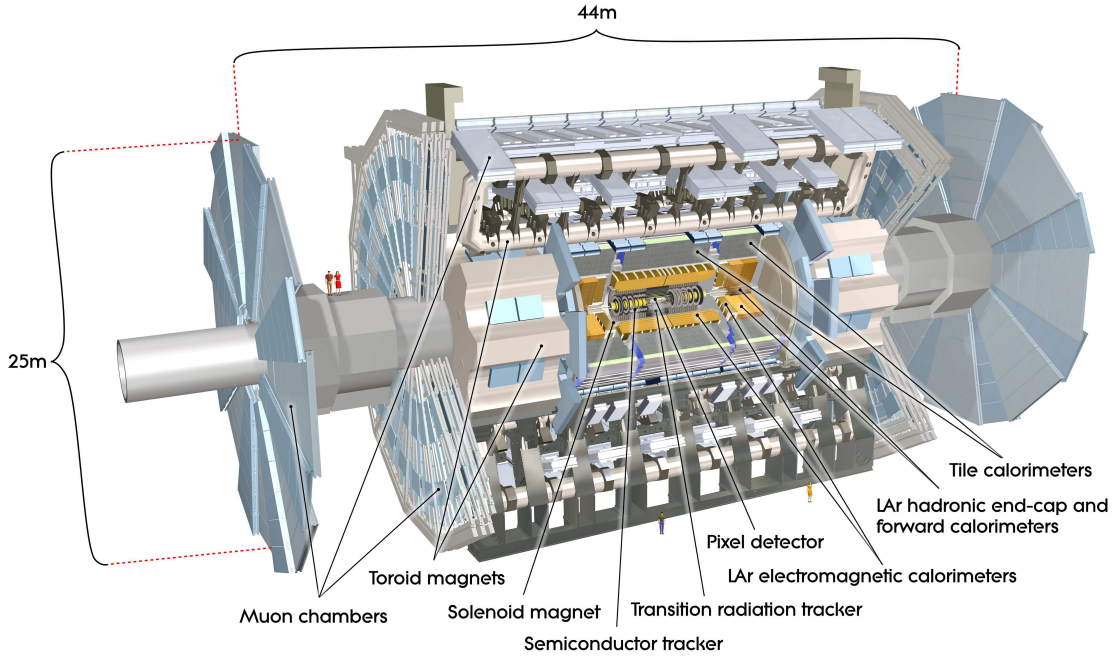


Figure 3.5: Cut-away view of the ATLAS detector [30].

850 to the z -axis where ϕ is the azimuthal angle. Instead of using the polar angle θ to describe particle
 851 trajectories, pseudorapidity η is used instead, defined in terms of θ :

$$\eta = -\ln(\tan(\theta/2)) \quad (3.2)$$

852 Pseudorapidity has the useful property that differences in η are invariant under Lorentz boosts along
 853 the z -axis. The separation between two particles p_i and p_j is often expressed in terms of the quantity
 854 ΔR , defined as:

$$\Delta R(p_i, p_j) = \sqrt{(\eta_i - \eta_j)^2 + \min[|\phi_i - \phi_j|, |\phi_j - \phi_i|]^2} \quad (3.3)$$

855 Here, the difference in ϕ is taken in whichever direction results in a value less than π , since $\phi = [0, 2\pi]$
 856 “wraps around” the detector in the azimuthal direction.

857 3.2.1 The Inner Detector

858 The ID is a tracking system that reconstructs the trajectories of charged particles. It spans just over
 859 a meter in radius, with the innermost layer of sensors at 33.25 cm away from the beam line. Charged
 860 particles traveling through the ID leave *hits* in each sensor they pass through, and a track is fit to

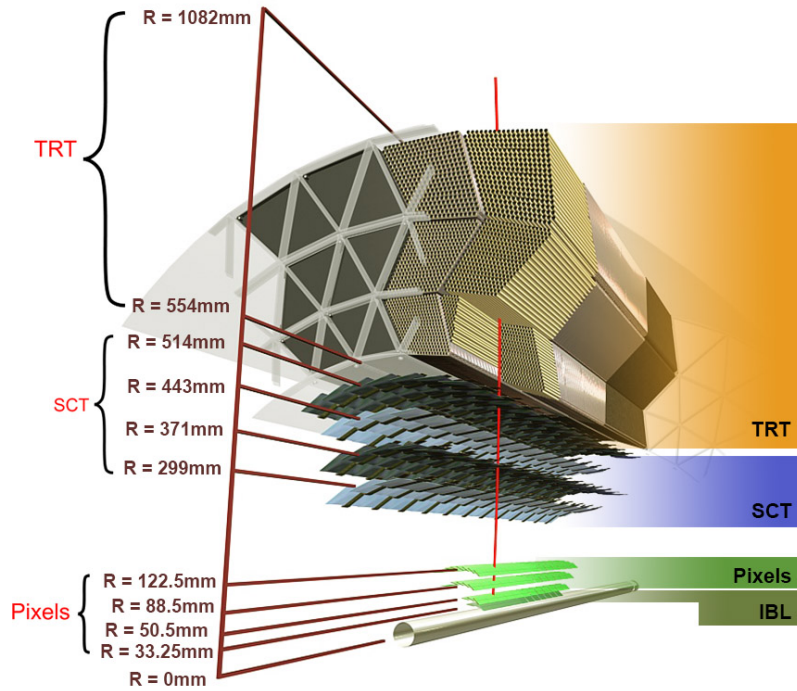


Figure 3.6: The barrel layers of the Pixel, SCT, and TRT detectors making up the Inner Detector.

the hits to reconstruct the path of the particle. Tracks are reconstructed within a pseudorapidity range of $|\eta| < 2.5$. A solenoid magnet outside the ID produces a 2 T magnetic field that bends the particles, allowing for their momenta transverse to the field to be measured according to:

$$p_T = q \cdot B \cdot r \quad (3.4)$$

where q is the charge of the particle (± 1), B is the strength of the magnetic field, and r is the radius of the track's curvature. The three subdetectors making up the ID are detailed in the following subsections, and more technical information can be found in [38, 39]. A cut-away view of the barrel region of the ID is shown in Figure 3.6.

3.2.1.1 Pixel Detector

The Pixel Detector consists of four cylindrical barrel layers⁴ and three endcap disks on either side. It is the innermost subdetector of the ID with coverage up to $|\eta| < 2.5$. The individual sensors measure

⁴For now, the outer three barrel layers will be covered in conjunction with the endcaps; the innermost layer will be described separately.

871 50 $\mu\text{m} \times 400 \mu\text{m}$ and are installed on the silicon wafers that make up the layers. All in all, there are
872 1744 wafers with 80 million readout channels. The sensors themselves are silicon semiconducting
873 diodes that provide a signal when a charged particle passes through. The Pixel Detector has the
874 finest resolution of all the ID subdetectors, at 10 μm in the $r\text{-}\phi$ plane and 40 μm in the z direction.

875 During the upgrade period prior to Run 2, a new innermost layer was added to the Pixel detector
876 barrel: the Insertable B-Layer (IBL) [40]. The IBL lies closest to the interaction point, at a radius
877 of 33.25 cm from the beam line, and it is relied upon to provide high-precision measurements close
878 to the interaction point. Its addition allows better precision in detecting displaced vertices from
879 b -jets, for example. It consists of 280 silicon pixel modules arranged on 14 staves that run parallel
880 to the beam line. Each stave consists of 12 two-chip planar modules in the middle ($|\eta| < 2.7$) with
881 four 3D sensors [41] on either side ($2.7 < |\eta| < 3.0$). The IBL's pixel sensors are 50 $\mu\text{m} \times 250 \mu\text{m}$ in
882 size and have a resolution of 10 μm in $r\text{-}\phi$ and 75 μm in z [42].

883 **3.2.1.2 Semiconductor Tracker**

884 The next subdetector of the ID is the SCT, which has four barrel layers and nine endcap disks per
885 side and provides coverage within $|\eta| < 2.5$. The SCT operates on the same principle as the Pixel
886 Detector, but the sensitive elements are larger silicon “strips” placed on the wafers. This shape
887 change assissts in covering the larger surface area required by the increasing detector radius. Each
888 detector layer is actually made up of two layers of wafers, placed back-to-back with an angle of
889 40 mrad between them. The resolution in the $r\text{-}\phi$ plane is very fine at 17 μm , but, due to the strip
890 shape, the resolution along z is rather poor at 580 μm .

891 **3.2.1.3 Transition Radiation Tracker**

892 The outermost component of the ID is the TRT [43, 44, 45], which uses a completely different
893 technology from the Pixel and SCT to identify particle hits. The TRT is unique in that it combines a
894 drift tube tracker with transition radiation detection for electron identification. The TRT's sensitive
895 elements are drift tubes (referred to as “straws”) that are 4 mm in diameter and consists of a
896 cylindrical cathode with an anode wire running through the center. Each straw is filled with a gas
897 mixture including xenon or argon which provide ionizing radiation when high energy particles pass
898 through them. The resulting electrons drift to the anode and register a voltage, indicating a hit in
899 the detector element.

900 Between the straws are polyethelene fibers in the barrel and polypropylene foil in the endcaps

901 in order to encourage particles to emit transition radiation photons. These photons also ionize the
 902 gas within the straws, leading to a higher signal. The TRT takes advantage of the fact that lighter
 903 particles are more likely to emit transition radiation by using a ternary output: zero, low-threshold,
 904 and high-threshold. High-threshold hits are generally caused by electrons due to their low mass,
 905 and this can help in discriminating electrons against backgrounds.

906 There are over 100,000 straws in the barrel of the TRT, and nearly 250,000 in the endcaps. The
 907 TRT provides pseudorapidity coverage up to $|\eta| < 2.0$ with a resolution in the $r\phi$ plane of $130 \mu\text{m}$.
 908 Since the drift tubes are insensitive along the direction of the wire, the TRT has no resolution in
 909 the z direction.

910 3.2.2 The Calorimeters

911 ATLAS utilizes two different calorimeters, the Liquid Argon and Tile Calorimeters [46, 47], in order
 912 to measure electromagnetic and hadronic objects. The general principle behind both calorimeters is
 913 the same: an incoming particle showers as it passes through and eventually stops, and the resulting
 914 energy deposits are read out. Both are sampling calorimeters, which consist of alternating layers
 915 of a dense material to induce the showering (absorber) and a second material which measures the
 916 energy (active material). An advantage to this type of calorimeter is that a very dense absorber can
 917 be used in order to produce a shower in a limited space, even if it is unsuitable for measuring the
 918 energy from the shower. However, as some of the energy is deposited in the dense material, and the
 919 total shower energy must be estimated. ATLAS's calorimeter systems are shown in Figure 3.7.

920 Electromagnetic objects, such as electrons and photons, shower via cascades of bremsstrahlung
 921 photons and e^+e^- pairs. The radiation length X_0 is defined as the mean distance over which an
 922 electron's energy is reduced to $1/e$ of its original value, or $E(x) = E_0 e^{-x/X_0}$. The majority of the
 923 shower energy is deposited in the first few radiation lengths. The longitudinal shower depth scales
 924 logarithmically with particle energy, and the transverse shower width is described by the Molière
 925 radius⁵ of the material.

926 Hadronic showers (referred to as *jets*) are the result of quarks or gluons which hadronize and
 927 shower primarily via the strong interaction. Hadronic showers are generally wider than the electro-
 928 magnetic showers described above. The longitudinal depth of the hadronic shower scales with the
 929 nuclear interaction length of the material λ , defined as the mean distance for the number of particles

⁵A cone with a radius equal to the Molière radius (M_R) will contain approximately 90% of the shower energy. At a radius of $2M_R$, 95% of the energy will be contained.

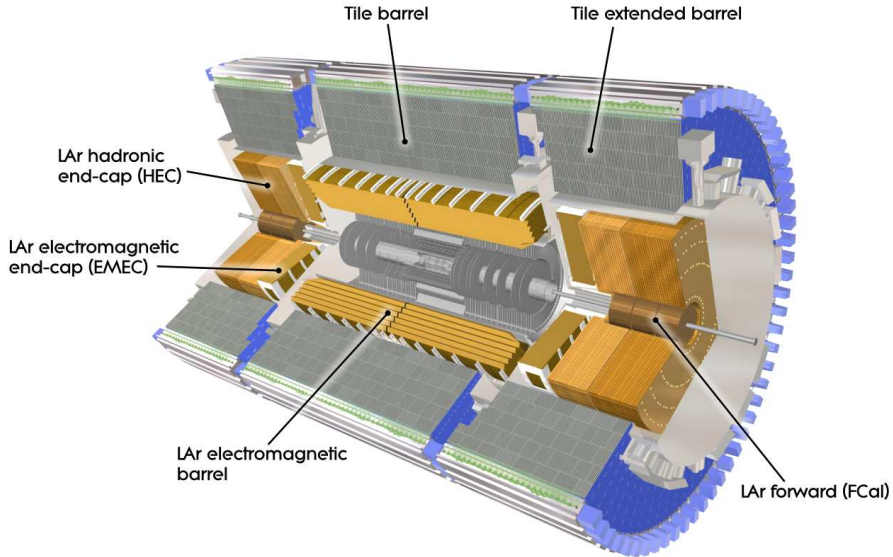


Figure 3.7: Cut-away view of the ATLAS calorimeter systems [1].

in a hadronic jet to be reduced to $1/e$ of the initial number. In addition, about $1/3$ of the shower products are neutral pions π^0 which decay electromagnetically.

3.2.2.1 Liquid Argon Calorimeter

The LAr Calorimeter contains four individual calorimeters: the electromagnetic barrel (EMB) and endcaps (EMEC), and the hadronic endcap (HEC) and forward calorimeter (FCal). The calorimeter is surrounded by a cryostat held at a temperature around 90 K.

Focusing on the electromagnetic components first, the EMB covers $|\eta| < 1.475$ and the two EMECs cover $1.375 < |\eta| < 3.2$. They consist of alternating layers of lead absorber and liquid argon. The thickness of the lead depends on the location within the detector, but the layers range from 1.1-2.2 mm. The absorbers are folded into an accordion shape, where the folding angles are varied in order to keep the thickness of the liquid argon gap constant (about 2.1 mm) across the barrel. The minimum number of radiation lengths at the end of the electromagnetic calorimeter is $24 X_0$.

There are four layers within the EMB and EMEC including an innermost pre-sampler that helps correct for energy lost before the shower reaches the calorimeter. The next three layers consist of differently shaped cells successively reducing in granularity. The first layer consists of narrow strips

946 for fine-grained η resolution, and the majority of the shower energy is deposited in the second layer.
 947 The accordion shape as well as the sizes of the cells in the EMB are shown in Figure 3.8.

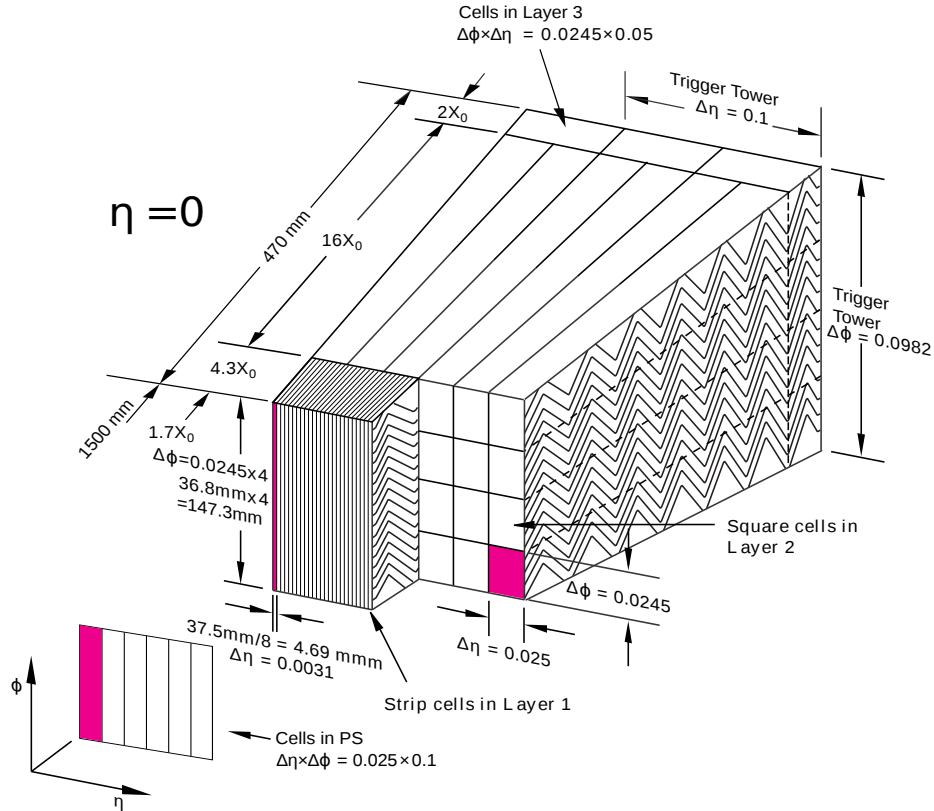


Figure 3.8: Diagram of the cells within the LAr barrel. The accordion structure can be seen in the cut-away view [46].

948 The HEC is located directly behind the EMEC and covers $1.5 < |\eta| < 3.2$. It uses thick copper
 949 plates as the absorber (25 mm in the front wheels and 50 mm in the rear wheels) separated by 8.5 mm
 950 gaps filled with liquid argon. Rather than the accordion shape, the HEC cells are rectangular.

951 The FCal provides coverage for hadronic jets over the range $3.2 < |\eta| < 4.9$. Each FCal endcap
 952 consists of three layers. The first is an electromagnetic calorimeter with a copper absorber, while the
 953 other two hadronic layers use a tungsten absorber. Due to the high particle flux entering the FCal,
 954 the liquid argon gaps are very narrow, and electrodes are embedded into the absorbers parallel to
 955 the beam line.

956 **3.2.2.2 Tile Calorimeter**

957 The TileCal consists of a barrel and two “extended barrel” sections which cover the range $|\eta| < 1.7$.
958 It consists of alternating layers of steel plates and polystyrene scintillator tiles as the absorbers and
959 active material, respectively. The total thickness of the TileCal is approximately 9λ . As the shower
960 passes through the scintillators, photons are emitted that are picked up by wavelength shifting fibers
961 and passed to photomultiplier tubes.

962 **3.2.3 The Muon Spectrometer**

963 The outermost subdetector in ATLAS is the Muon Spectrometer [48]. Due to the high mass of muons
964 compared to electrons, they pass through the calorimeters, necessitating their own detector. The
965 MS is a high-resolution spectrometer providing tracking for muon reconstruction within $|\eta| < 2.7$.
966 A set of toroid magnets provide an azimuthal magnetic field that bends the muons for momentum
967 measurements, much like in the ID. Four different technologies are used in the MS:

- 968 ● Monitored Drift Tubes (MDT) are used across the entire η range for precision measurements
969 of the tracks with a per-hit resolution in the range of $60\text{--}80 \mu\text{m}$. These consist of an aluminum
970 tube with an anode wire running through the middle; the tubes are filled with a gas mixture
971 containing argon. When a muon passes through, the gas is ionized, and the electrons are
972 collected on the wire.
- 973 ● Cathode Strip Chambers (CSC) are used for the forward regions of the endcaps ($|\eta| >$
974 2.0). They operate on a similar principle to the MDTs, except they are strips instead of tubes,
975 with a mesh of anode wires running in parallel.
- 976 ● Resistive Plate Chambers (RPC) in the barrel are primarily used to provide input for the muon
977 trigger system. They consist of pairs of plastic resistive plates with a 2 mm gap between them
978 filled with a gas mixture. Electrodes are attached to the plates, and muons passing through
979 ionize the gas and lead to electric discharges which in turn reduce the potential.
- 980 ● Thin Gap Chambers (TGC) are also used for triggering, but for the endcaps. The TGCs are
981 arranged on circular disks consisting of two rings, and are similar in function to the CSCs but
982 with a different gas mixture.

983 **3.2.4 Particle reconstruction**

984 Particle reconstruction algorithms

985 **3.2.4.1 Track reconstruction**

986 The track reconstruction algorithm used in ATLAS follows

987 Following this procedure, TRT hits can be incorporated into the track fit through *TRT track*
988 *extension* [49]. Compatible sets of TRT measurements are found for tracks found in the silicon
989 detectors surviving the ambiguity solving. The algorithm requires that the original silicon-only
990 track not be modified by the inclusion of the TRT hits; it is simply an extension of the existing
991 track.

992 What is described above is the *inside-out* reconstruction algorithm; there is also an *outside-in*
993 reconstruction that begins in the TRT. This algorithm is not covered in detail here, as much of the
994 process is similar to the above. The general workflow begins with finding track segments in the
995 TRT, constructing the track candidates including the silicon hits, and finally ambiguity solving.

996 **3.2.4.2 Muon reconstruction**

997 **3.2.4.3 Electron reconstruction**

998 **3.2.4.4 Jet reconstruction**

CHAPTER 4

1000 Alignment of the ATLAS Inner Detector

1001 When a charged particle passes through the ATLAS ID, it leaves hits in the sensors along its path.
1002 In order to accurately measure the track of the particle, it is necessary to know where these hits
1003 occurred as precisely as possible, which in turn requires knowledge of the physical location of the
1004 sensor that registered the hit. If one of these sensors is displaced relative to its expected position
1005 in the known detector geometry, or *misaligned*, the assumed location of the corresponding hit will
1006 not match its actual location, resulting in an incorrect track fit. These misalignments can occur for
1007 any number of reasons, including but not limited to elements shifting during maintenance periods
1008 or cycles in ATLAS's magnetic field, or small movements during normal detector operations. The
1009 effect of a misaligned detector element on the track reconstruction is shown in Figure 4.1.

1010 In order to correct the misalignments, the ID alignment procedure is applied to accurately
1011 determine the physical position and orientation of each detector element. The baseline accuracy of
1012 the alignment is required to be such that the track parameter resolutions are not degraded by more
1013 than 20% with respect to those derived from a perfect detector geometry⁶. This corresponds to a
1014 precision of better than $10\mu\text{m}$ in the positioning of the elements of the silicon detectors [50].

1015 This chapter outlines the ID alignment procedure, the alignment of the detector during the 2015
1016 data taking period, and the steps taken to measure momentum biases in the alignment.

⁶The so-called *perfect geometry* refers to the description of the ATLAS detector in which every sensor precisely matches its design specifications. The perfect geometry contains no misalignments, and the position of each sensor is known exactly.

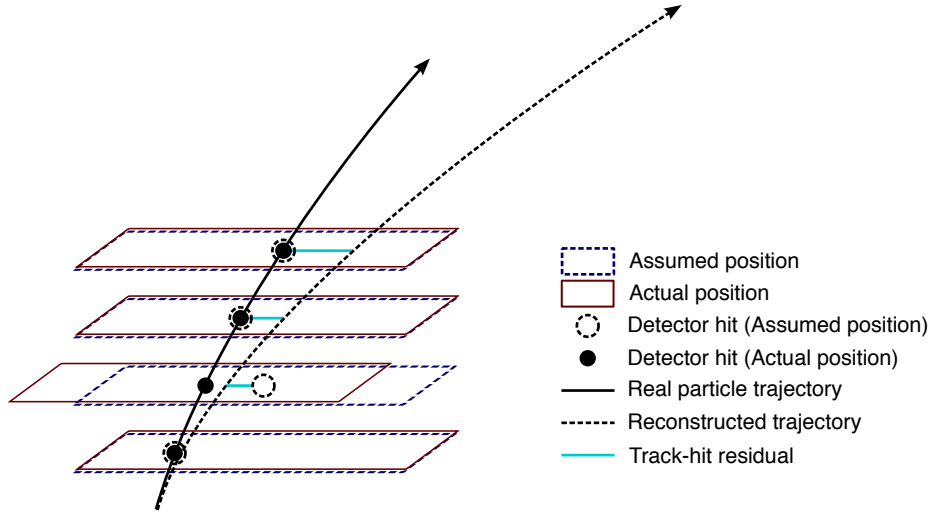


Figure 4.1: Graphical representation of the effect of a misaligned detector element. The reconstructed particle track (dashed arrow) differs from the actual trajectory of the particle (solid arrow) due to the shift in one of the detector elements. The cyan lines represent the track-to-hit residuals.

1017 4.1 The alignment method

1018 The alignment procedure uses a track-based algorithm that updates the locations of detector ele-
 1019 ments in order to minimize the set of track-hit *residuals*. These residuals are defined as the distance
 1020 between the fitted track position in a given detector element to the position of the hit recorded by
 1021 the same element, and are shown by the cyan lines in Figure 4.1.

1022 Tracks in ATLAS are parameterized as five-dimensional vectors [51]:

$$\vec{\tau} = (d_0, z_0, \phi_0, \theta, q/p) \quad (4.1)$$

1023 where d_0 and z_0 are the transverse and longitudinal impact parameters with respect to the origin,
 1024 ϕ_0 is the azimuthal angle of the track at the point of closest approach to the origin, θ is the polar
 1025 angle, and q/p is the charge of the track divided by its momentum. The residual for the i^{th} hit of a
 1026 given track can then be written in terms of the track parameters $\vec{\tau}$ and a set of alignment parameters
 1027 \vec{a} that describe the hit location [52]:

$$r_i(\vec{\tau}, \vec{a}) = (\vec{m}_i - \vec{e}_i(\vec{\tau}, \vec{a})) \cdot \hat{k} \quad (4.2)$$

1028 where \vec{e}_i is the intersection point of the extrapolated track with the sensor, \vec{m}_i is the position of the
 1029 associated hit within the sensor, and \hat{k} is the unit vector defining the direction of the measurement
 1030 within the sensor. \vec{r} then represents the vector of residuals for the given track.

1031 A χ^2 function can be built from the residuals of all collected tracks:

$$\chi^2 = \sum_{\text{tracks}} \vec{r}^T V^{-1} \vec{r} \quad (4.3)$$

1032 where V is the covariance matrix of the hit measurements. The χ^2 function is then minimized with
 1033 respect to the alignment parameters \vec{a} , which contain all degrees of freedom being aligned. The
 1034 minimization condition with respect to \vec{a} is:

$$\frac{d\chi^2}{d\vec{a}} = 0 \rightarrow 2 \sum_{\text{tracks}} \left(\frac{d\vec{r}}{d\vec{a}} \right)^T V^{-1} \vec{r} = 0 \quad (4.4)$$

1035 This equation can be difficult to solve exactly, so the residual is rewritten as a first order Taylor
 1036 expansion:

$$\vec{r} = \vec{r}_0 + \frac{d\vec{r}}{d\vec{a}} \delta\vec{a} \quad (4.5)$$

1037 where \vec{r}_0 is dependent on an initial set of track and alignment parameters \vec{r}_0 and \vec{a}_0 , respectively;
 1038 the track parameter dependence has also been folded into the total derivative $\frac{d\vec{r}}{d\vec{a}}$. Equation 4.5 can
 1039 then be inserted into the minimization condition from Equation 4.4 to give:

$$\left[\sum_{\text{tracks}} \left(\frac{d\vec{r}}{d\vec{a}} \right)^T V^{-1} \left(\frac{d\vec{r}}{d\vec{a}} \right) \right] \delta\vec{a} + \sum_{\text{tracks}} \left(\frac{d\vec{r}}{d\vec{a}} \right)^T V^{-1} \vec{r}_0 = 0 \quad (4.6)$$

1040 From this equation, the alignment matrix \mathcal{M}_a and alignment vector $\vec{\nu}_a$ can be defined:

$$\mathcal{M}_a = \sum_{\text{tracks}} \left(\frac{d\vec{r}}{d\vec{a}} \right)^T V^{-1} \left(\frac{d\vec{r}}{d\vec{a}} \right) \quad (4.7)$$

1041

$$\vec{\nu}_a = \sum_{\text{tracks}} \left(\frac{d\vec{r}}{d\vec{a}} \right)^T V^{-1} \vec{r}_0 \quad (4.8)$$

1042 Finally, the alignment corrections $\delta\vec{a}$ can be solved for by inverting the alignment matrix:

$$\delta\vec{a} = -\mathcal{M}_a^{-1} \vec{\nu}_a \quad (4.9)$$

1043 which is a linear system of equations with a number of equations equal to the number of alignment
 1044 degrees of freedom [53].

1045 Inverting the full matrix and solving the resulting system of equations is referred to as *Global*
 1046 χ^2 alignment [52]. This can be useful, as \mathcal{M}_a contains all the correlations between the alignable
 1047 structures. However, inverting the matrix is difficult when the number of degrees of freedom becomes
 1048 large—as the number of alignable structures increases, so too does the size of the matrix \mathcal{M}_a .
 1049 Eventually inverting the matrix becomes too computationally intensive to be practical.

1050 This problem is solved by the *Local* χ^2 algorithm [54]. In this case, the alignment matrix is
 1051 constructed to be block-diagonal, allowing for it to be inverted even for large numbers of degrees of
 1052 freedom. This is achieved by replacing the full derivative in Equation 4.6 with the partial derivative
 1053 $\frac{\partial \vec{r}}{\partial \vec{a}}$. The new alignment matrix \mathcal{M}'_a and alignment vector $\vec{\nu}'_a$ become:

$$\mathcal{M}_a = \sum_{\text{tracks}} \left(\frac{\partial \vec{r}}{\partial \vec{a}} \right)^T V^{-1} \left(\frac{\partial \vec{r}}{\partial \vec{a}} \right) \quad (4.10)$$

1054

$$\vec{\nu}_a = \sum_{\text{tracks}} \left(\frac{\partial \vec{r}}{\partial \vec{a}} \right)^T V^{-1} \vec{r}_0 \quad (4.11)$$

1055 Inverting \mathcal{M}'_a is considerably faster and less memory intensive even for large numbers of degrees of
 1056 freedom; however, the correlations between the alignable structures is lost.

1057 Due to the Taylor expansion used in Equation 4.6, several iterations of the alignment algorithm
 1058 may be necessary to converge on a final set of alignment constants. The Local χ^2 alignment typically
 1059 requires more iterations due to the loss of the correlation information [55]. In practice, the ATLAS
 1060 reconstruction is run over a set of events, and the resulting tracks are fed to the alignment algorithm.
 1061 The residuals are calculated, the alignment matrix is built and inverted, and a new set of alignment
 1062 constants is obtained. The convergence is checked in two ways:

1063 1. Measuring the $\Delta\chi^2$ with respect to the previous iteration. If it is near zero, then the χ^2 is
 1064 approaching its minimum.

1065 2. Looking at the residual distributions for different alignable structures. A well aligned detector
 1066 will have a mean residual of zero with a width approximating the intrinsic resolution of the
 1067 detector.

1068 If the above checks are satisfied, the process is finished and the final alignment constants are read
 1069 out; if not, another iteration is performed. A visual representation of the alignment chain is shown
 1070 in Figure 4.2.

1071 Since a χ^2 minimization is used to align the detector, if there is a systematic misalignments in
 1072 the detector that does not adversely affect the χ^2 , the algorithm will be insensitive to it. These
 1073 misalignments are referred to as *weak modes*, and special care is taken to remove them [56]. One
 1074 potential impact of weak modes is a bias in the track momentum of reconstructed particles. This
 1075 particular effect is the subject of Section 4.4.

1076 The detector is aligned both in “real-time” as data is collected and during dedicated offline
 1077 alignment campaigns. The real-time alignment is run in ATLAS’s *calibration loop*, which comprises

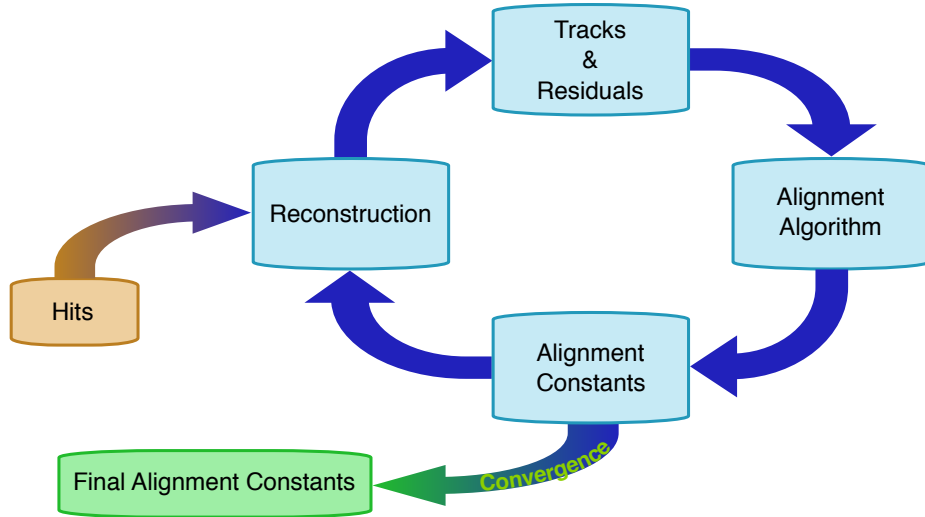


Figure 4.2: Graphical representation of the ID alignment chain.

1078 the first stage in the preparation of data for physics analysis. The calibration loop requires the
 1079 alignment—as well as various other detector calibrations—to be available within 48 hours for initial
 1080 data processing. A fast, coarse-grained alignment⁷ is run on a subset of the available data containing
 1081 full tracking information, and the results are propagated to the reconstruction of that particular
 1082 run [57]. Due to the time constraints of the calibration loop, a full sensor-by-sensor alignment is not
 1083 possible.

1084 The more thorough and finely tuned alignments are reserved for the dedicated alignment cam-
 1085 paigns. These generally occur early in data taking campaigns, typically once a sufficient amount
 1086 of data is collected after a detector shutdown, in order to obtain a good baseline alignment for
 1087 use in the remainder of the data collection period. One such alignment campaign, the initial offline
 1088 alignment of the ATLAS detector at the beginning of Run 2, is the subject of Section 4.2. Once data
 1089 taking is complete, another set of alignment constants is derived for the full set of available data,
 1090 and it is typically divided into several “blocks” to account for potential run-by-run misalignments.
 1091 The data is then reprocessed using the newly derived detector geometry.

1092 4.1.1 Alignment levels

1093 The alignment of the detector is performed at several levels of increasing granularity. This adds
 1094 flexibility in being able to align only as finely as needed, and it also allows for global, detector-level

⁷The calibration loop runs up to a Level 2 alignment in the silicon detectors, which involves treating each layer of sensors as a single object. The alignment levels are defined in greater detail in Table 4.1.

1095 misalignments to be corrected first before dealing with finer adjustments.

- 1096 • Level 1 (L1) alignment involves moving entire subdetector components as a single unit, such
1097 as the entire Pixel detector, or the SCT barrel. These often have the largest misalignments,
1098 but they are easily corrected and do not require large volumes of data to do so.
- 1099 • Level 2 (L2) alignment treats individual layers in the silicon detectors (modules in the TRT)
1100 and end cap disks as individual alignable objects.
- 1101 • Level 2.7 (L27) alignment was introduced with the addition of the IBL to the ID in Run 2. It
1102 involves the stave-by-stave alignment of the IBL and Pixel barrel⁸.
- 1103 • Level 3 (L3) alignment treats each sensor in the silicon detectors and each straw in the TRT
1104 as an individual alignable object. It is the finest grained alignment available but also the most
1105 computationally intensive due to the large number of degrees of freedom. The large number
1106 of individual detector sensors being aligned also requires the largest amount of statistics.

1107 The different alignment levels are listed in more detail in Table 4.1, including the number of alignable
1108 structures and associated degrees of freedom for each detector component.

1109 The implementation of the alignment algorithm in the software is flexible enough to allow each
1110 subsystem to be aligned individually at a specified level. Each alignable structure has six degrees of
1111 freedom: 3 translations (T_x, T_y, T_z) and 3 rotations (R_x, R_y, R_z)⁹; however individual degrees of
1112 freedom may be turned on and off as required. In a typical alignment job, L1 and L2 contain few
1113 enough degrees of freedom that the Global χ^2 algorithm can be used, but L3 alignments (which can
1114 contain over 36,000 degrees of freedom in the silicon detectors alone) require the Local χ^2 algorithm.

1115 4.1.2 Alignment coordinate systems

1116 The global coordinate system (x, y, z) used by the ID alignment matches that of the ATLAS detector
1117 in general. The positions and orientations of individual detector modules of the ID are defined by
1118 a right-handed local coordinate system (x', y', z') where the origin is defined as the geometrical
1119 center of the module. The x' -axis for each silicon module is defined to point along the most sensitive
1120 direction of the module, the y' -axis is oriented along the long side of the module, and the z' -axis is

⁸For the purposes of this Chapter, the term “Pixel” will refer to the original three layers of the Pixel detector, and the IBL will be referenced separately.

⁹The TRT is an exception, as the subdetector does not have any resolution along the length of the straw. Therefore, for the barrel, T_z is omitted. Similarly for the straws themselves, only two parameters are defined: translation with respect to the radial direction (T_ϕ) and rotation with respect to the radial axis (R_r for the barrel and R_z for the end-caps) [58].

Level	Description of alignable structure	Structures	DoF
1	IBL detector	1	6
	Whole Pixel detector	1	6
	SCT barrel and 2 end-caps	3	18
	TRT barrel and 2 end-caps (T_z fixed)	3	17
Total:		8	47
2	IBL detector	1	6
	Pixel barrel layers	3	18
	Pixel end-cap disks	2×3	36
	SCT barrel layers	4	24
	SCT end-cap disks	2×9	108
	TRT barrel 32 modules (T_z fixed)	3×32	480
	TRT end-cap wheels	2×40	480
Total:		208	792
2.7	IBL staves	14	84
	Pixel barrel staves	$22+38+52$	672
	Pixel end-cap disks	2×3	18
	Total:		132
3	IBL modules	280	1,680
	Pixel modules	1,744	10,464
	SCT modules	4,088	24,528
	TRT barrel wires (T_ϕ, R_r only)	105,088	210,176
	TRT end-cap wires (T_ϕ, R_Z only)	245,760	491,520
	Total silicon sensors:		6,112
	Total TRT wires:		350,848
36,672		701,696	

Table 4.1: The four alignment levels for each of the detector subsystems. The total number of alignable structures and degrees of freedom (DoF) to be aligned are given for each level.

orthogonal to the (x', y') plane. For the TRT straws, the x' -axis is perpendicular to both the wire and the radial direction, defined from the origin of the global frame to the straw center, the y' -axis points along the straw, and once again the z' -axis is orthogonal to the (x', y') plane. A depiction of the global and local coordinate systems for the ID is shown in Figure 4.3.

When considering the alignment degrees of freedom listed earlier in Section 4.1.1, grouped collections of modules, layers, or entire subdetectors use the global coordinate system; individual modules use their respective local coordinate systems. The translations T_i are with respect to the origin of the given reference frame, and the rotations R_i are taken about the Cartesian axes.

4.2 Early 2015 alignment of the ATLAS detector

At the end of Run 1, the LHC was shut down for upgrades and maintenance. During this time, a number of upgrades were performed on the ATLAS detector, including the installation of a new

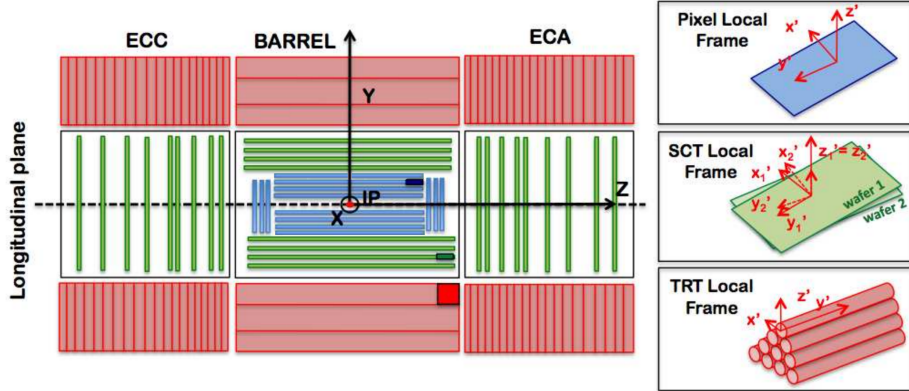


Figure 4.3: A schematic representation of the Inner Detector in the longitudinal plane with the global coordinate system overlaid on top. The Pixel detector and IBL are shown in blue, the SCT in green, and the TRT in red. The local coordinates for each subdetector module are inset on the right. Image taken from [59].

innermost layer of the Pixel detector, the Insertable B-Layer (IBL). These changes to the ID required some detector components to be removed temporarily, and many elements shifted relative to each other over the course of the maintenance process. In order to correct for these large detector movements prior to $\sqrt{s} = 13$ TeV collision data taking, an alignment was performed using cosmic ray data collected in early 2015 [59]. This alignment was able to correct for the majority of the large detector-wide misalignments as well as determine the global position of the IBL at the micron level.

In June of 2015, shortly after the data taking period began, the first track-based alignment of the refurbished ID was performed using the initial 7.9 pb^{-1} of $\sqrt{s} = 13$ TeV pp collision data [60]. Starting from the geometry determined by the cosmic ray alignment, referred to hereafter as the *March alignment*, an improved set of alignment constants (the *June alignment*) was derived from a data set of approximately 1.4 million selected tracks. For comparison, a MC sample containing approximately 2.7 million tracks was constructed from dijet events simulated using a perfect detector geometry; the MC events are reweighted to match the η and p_T distributions found in the data. Additional validation of the alignment results uses a set of cosmic ray data collected by the detector during the LHC collisions.

4.2.1 June alignment procedure

The data set used as the input for the alignment contains a subset of physics events used for prompt reconstruction recorded at a rate of 10 Hz. To ensure that only high quality tracks are used for the

1150 alignment, each track is required to have transverse momentum $p_T > 3$ GeV, contain at least one
1151 hit in the Pixel detector, at least seven hits in the combined silicon detectors, and at least 25 hits
1152 in the TRT.

1153 A full L3 alignment of the IBL was included in the March alignment; however, a realignment was
1154 still necessary. Since cosmic rays used in the March alignment pass through the detector top-down,
1155 the staves on the sides of the IBL recorded fewer hits and thus could not be aligned as precisely
1156 as those on the top and bottom. Additionally, the IBL was operating at a temperature of -20°C
1157 during the cosmic data taking, and it was set to -10°C for collision data taking. This proved to be
1158 significant, as it was observed that the IBL staves experience a temperature-dependent, parabolic
1159 bowing in the local x' -direction of approximately $-10\mu\text{m}/\text{K}$ [61]. As a result, a full L3 alignment
1160 of the IBL was essential in order to correct for the bowing. Due to it being a brand new element of
1161 the detector as well as its importance in vertexing and b jet tagging, aligning the IBL sensors with
1162 a high degree of precision was one of the main goals of the June alignment.

1163 The June alignment was performed in two stages, with the first pass focusing on relative move-
1164 ments of the big structures and correcting for the bowing of the IBL. The March alignment corrected
1165 for these larger movements as well; however, it was observed during Run 1 that these sort of mis-
1166 alignments are introduced by changing conditions in the detector [56], such as in the cooling system
1167 or magnet power cycling, which may have occurred between the early cosmic data taking and the
1168 first $\sqrt{s} = 13$ TeV collisions. The silicon detectors were aligned at several different levels and the
1169 IBL was aligned at the module level; the TRT detector was kept fixed to act as a global reference
1170 frame. The full alignment chain for the first pass consisted of the following steps:

- 1171 1. The IBL, Pixel, and SCT detectors were aligned at L1. The SCT barrel was not aligned in
1172 T_z in order to constrain global displacements along the z -axis, as the TRT is not sensitive to
1173 that degree of freedom.
- 1174 2. The IBL, and Pixel barrel and end-caps, and SCT barrel were aligned at L2. The SCT end-caps
1175 were aligned at L1.
- 1176 3. The IBL and pixel barrel were aligned at L27, using all six degrees of freedom. The Pixel
1177 end-cap disks were only aligned in the plane (T_x , T_y , and R_z). The SCT was treated the same
1178 as in the previous step.
- 1179 4. The IBL was aligned at L3 using all six degrees of freedom for each module.

1180 The primary goal for the second pass was to remove a bias in the transverse impact parameter
 1181 d_0 found in the March alignment. In addition to the bias, the resolution of d_0 was also poorer
 1182 than expected. In order to correct for this, an additional constraint was passed to the alignment
 1183 which added the impact parameter with respect to the beam spot as a pseudo-measurement [62].
 1184 With this setup, when the alignment algorithm minimizes the χ^2 , it will take care of the impact
 1185 parameter minimization as well. Only the IBL and Pixel detectors were aligned in the second pass.
 1186 The different alignment stages are listed below, with the beam spot constraint being used in each:

- 1187 1. The IBL and Pixel detectors were aligned at L2 with the SCT fixed.
 1188 2. The IBL was aligned at L27
 1189 3. The IBL and Pixel barrel and end-caps were aligned at L3.

1190 The set of alignment constants obtained at the end of the second pass represents the June alignment.
 1191 The highest level of alignment each subdetector received over the course of the two passes is listed
 1192 in Table 4.2.

Detector		Highest level of alignment
IBL		L3
Pixel	Barrel	L3
	End-caps	L3 (T_x , T_y , and R_z only)
SCT	Barrel	L2 (except T_z)
	End-caps	L1
TRT		None

Table 4.2: Summary of the highest level of alignment applied to each ID subsystem when deriving the June alignment.

1193 4.2.2 Alignment results

1194 Alignment quality is primarily assessed by looking at the track-hit residual distributions. If the
 1195 detector is well aligned, the residuals will be Gaussian-distributed with a mean of zero and a width
 1196 approximating the detector’s resolution. The residual distributions are constructed from the same
 1197 selection of tracks that were used to perform the alignment, and are the focus of Section 4.2.2.1.
 1198 A second check on the alignment involves observables sensitive to the track parameter resolution.
 1199 In this case, cosmic rays are used, making use of a “split track” technique that takes advantage of
 1200 the top-to-bottom cosmic ray trajectory (compared to the center-out trajectory of collision tracks).
 1201 This method and the corresponding tests of the alignment are detailed in Section 4.2.2.2

1202 Additionally, the effect of the beam spot constrained alignment on the impact parameter d_0
 1203 needs to be checked. The d_0 distributions for both the March and June alignments are compared to
 1204 the MC simulation using a perfect geometry in Figure 4.4. In the March alignment, there is a bias
 1205 of $18 \mu\text{m}$ in the mean of the distribution and the width is nearly twice that of the perfect geometry.
 1206 After the second pass of the June alignment, the mean has shifted to $1 \mu\text{m}$ and the distribution has
 1207 narrowed considerably. From this, it appears that the constrained alignment successfully removed
 1208 the d_0 bias.

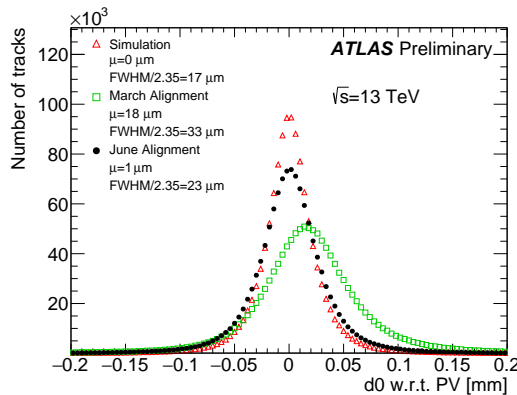


Figure 4.4: The d_0 distributions with respect to the reconstructed primary vertex using the $\sqrt{s} = 13 \text{ TeV}$ collision data sample reconstructed using the June (black) and March (green) alignments. The data is compared to a MC simulation using a perfect detector geometry (red). The distributions are normalized to the same number of entries.

1209 4.2.2.1 Residual distributions from collisions

1210 As mentioned previously, the primary focus of the June alignment campaign was on the IBL and the
 1211 Pixel detectors. These subdetectors are the closest to the beam line and have the finest resolutions
 1212 within the ID. The residual distributions in local x and y of the IBL planar sensors¹⁰ are shown in
 1213 Figure 4.5. These and subsequent figures in this section compare the June and March alignments
 1214 to the perfectly-aligned MC simulation. Noticeable improvement in the distribution widths can be
 1215 seen in both the local x - and y -directions, nearly matching the simulation in local x , which is the
 1216 most sensitive direction.

1217 Due to the temperature-dependent bowing of the IBL, it is also interesting to look at the means of
 1218 the residual distributions for each ring of IBL sensors along the beam line, as shown in Figure 4.6. A

¹⁰The IBL contains 12 planar sensors in the center of a stave, with four 3D sensors on either end. Only the planar sensors are shown here due to low statistics in the 3D sensors as well as poor MC modeling of these sensors.

deformation is clearly visible in the March alignment in both measurement directions, and the shape in the local x -direction is consistent with an average stave bowing due to the different operating temperature of the IBL during the March alignment and the 13 TeV collisions. This feature was nearly eliminated in both directions through the L3 alignment of the IBL sensors.

The local x and y residual distributions for the Pixel detector barrel and end-caps are shown in Figures 4.7 and 4.8. Even though the IBL is not included in the plots of the barrel, some of the noticeable improvement in the more sensitive local x direction is an effect of the improved IBL alignment. Similarly, the relatively broad local y residual distribution in the barrel likely indicates that further refinement of the IBL alignment was needed along that direction. Even so, the June alignment outperforms the March alignment and rivals the simulation in most of the plots.

Similar distributions for the SCT and TRT barrel and end-caps are shown in Figures 4.9 and 4.10, respectively. Much like with the Pixel residuals, there is a reduction in the width of the TRT residuals between the March and June alignments due to the alignment of the other subdetectors improving the quality of the track fit. Even though neither subdetector was aligned at module-level, the residuals indicate that the previous L3 alignment performed in Run 1 did not degrade significantly during the upgrade and maintenance period.

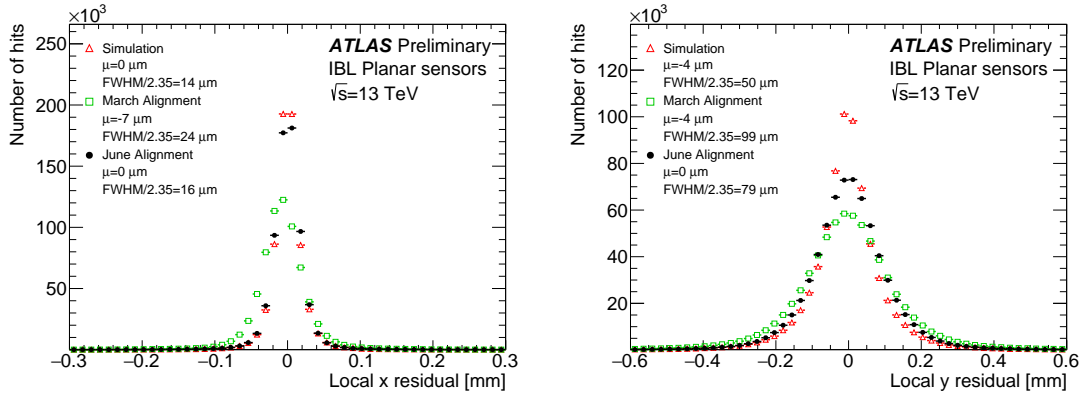


Figure 4.5: Local x (left) and local y (right) residual distributions of the IBL planar sensors using the $\sqrt{s} = 13$ TeV collision data sample reconstructed using the June (black) and March (green) alignments. The data is compared to a MC simulation using a perfect detector geometry (red). The distributions are normalized to the same number of entries.

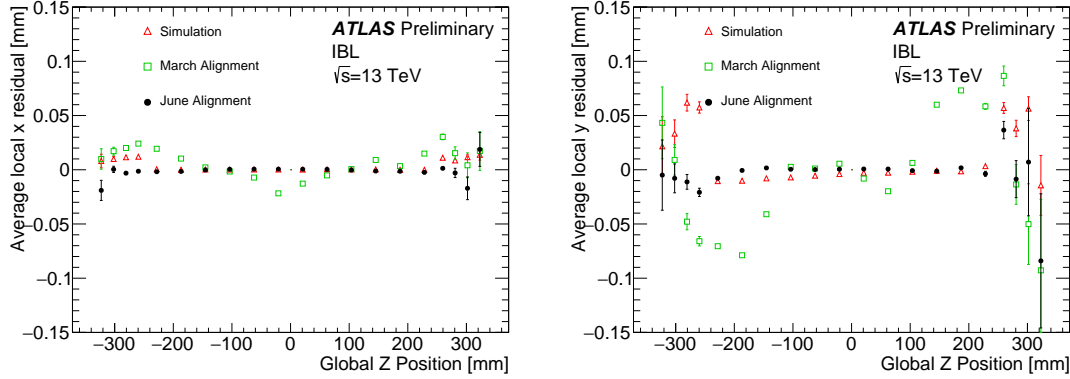


Figure 4.6: The mean of the local x (left) and local y (right) residual distributions as a function of the global z position of each IBL module using the $\sqrt{s} = 13$ TeV collision data sample reconstructed using the June (black) and March (green) alignments. The data is compared to a MC simulation using a perfect detector geometry (red).

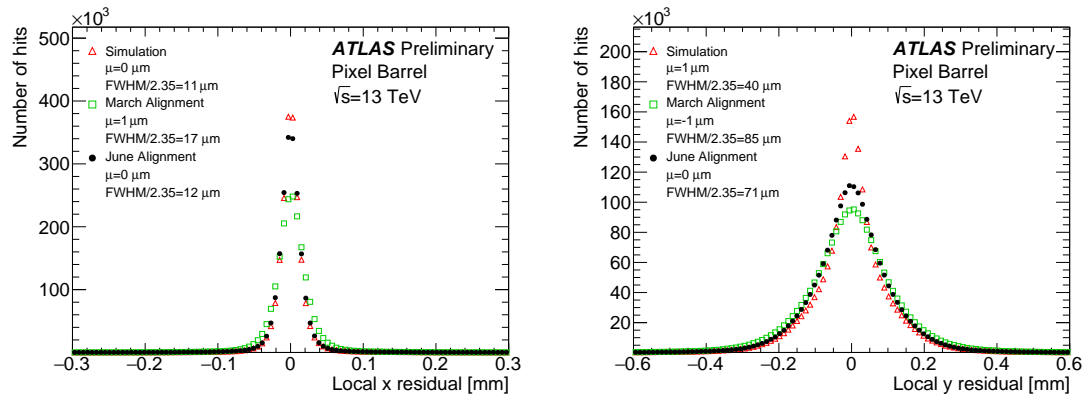


Figure 4.7: Local x (left) and local y (right) residual distributions for the Pixel barrel (excluding the IBL) using the $\sqrt{s} = 13$ TeV collision data sample reconstructed using the June (black) and March (green) alignments. The data is compared to a MC simulation using a perfect detector geometry (red). The distributions are normalized to the same number of entries.

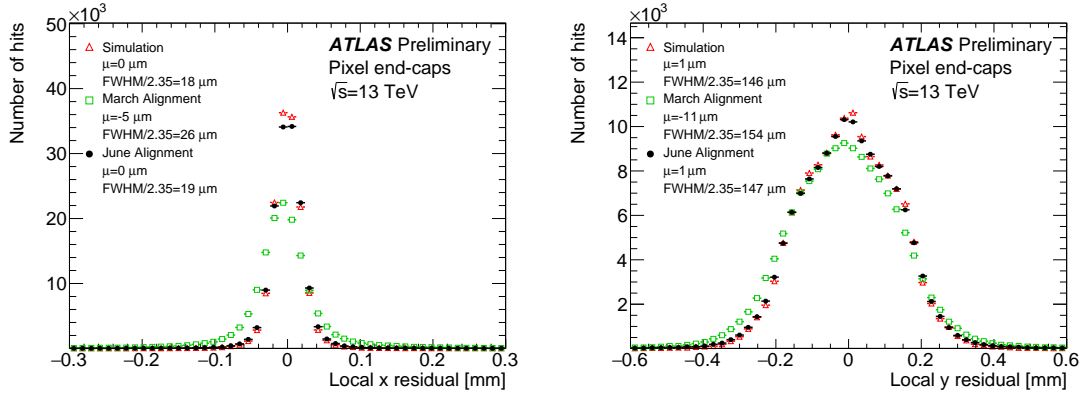


Figure 4.8: Local x (left) and local y (right) residual distributions for the Pixel end-caps using the $\sqrt{s} = 13$ TeV collision data sample reconstructed using the June (black) and March (green) alignments. The data is compared to a MC simulation using a perfect detector geometry (red). The distributions are normalized to the same number of entries.

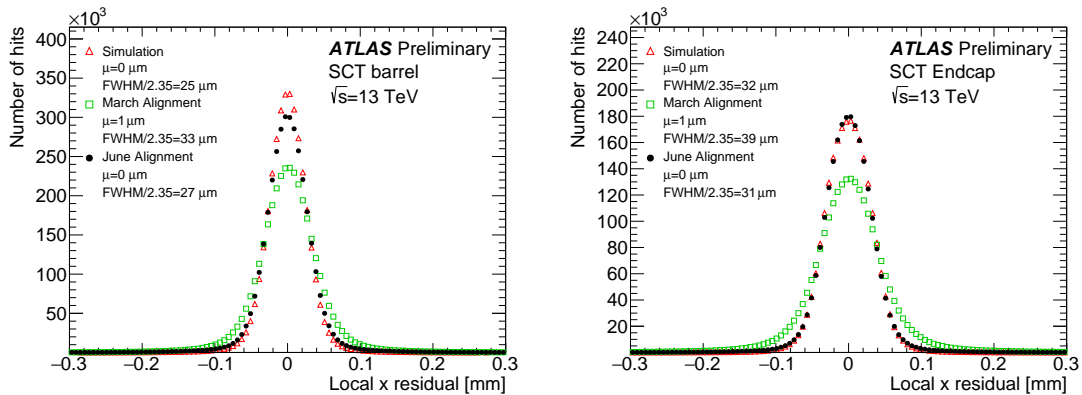


Figure 4.9: Local x residual distributions for the SCT barrel (left) and end-caps (right) using the $\sqrt{s} = 13$ TeV collision data sample reconstructed using the June (black) and March (green) alignments. The data is compared to a MC simulation using a perfect detector geometry (red). The distributions are normalized to the same number of entries.

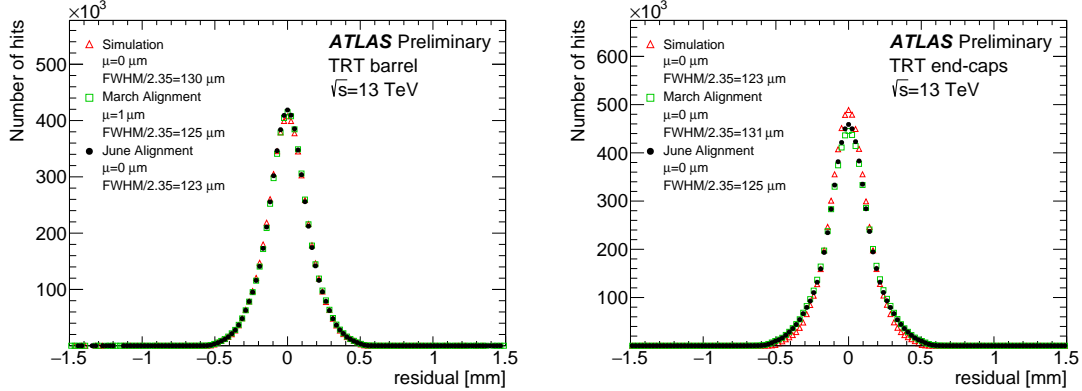


Figure 4.10: Residual distributions for the TRT barrel (left) and end-caps (right) using the $\sqrt{s} = 13$ TeV collision data sample reconstructed using the June (black) and March (green) alignments. The data is compared to a MC simulation using a perfect detector geometry (red). The distributions are normalized to the same number of entries.

1235 4.2.2.2 Track parameter resolution from cosmic rays

1236 Cosmic ray data is very useful as an independent check on the alignment in the barrel of the
 1237 detector. While tracks from $p\bar{p}$ collisions originate within the detector and travel outwards, a cosmic
 1238 ray that passes through the center of the detector leaves a track in both halves of the detector.
 1239 If the cosmic ray is split in half, as in Figure 4.11, then it can be treated as two separate tracks
 1240 each with nearly identical track parameters (some differences arise due to energy loss as the particle
 1241 passes through the detector). The distribution of the difference in a given track parameter $\Delta\tau$ is
 1242 approximately Gaussian with a variance $\sigma^2(\Delta\tau)$. Since both tracks come from the same particle,
 1243 each track individually has a variance equal to $\sigma^2(\Delta\tau)/2$. The resolution of the track parameter is
 1244 then given by the root mean square of the distribution divided by $\sqrt{2}$.

1245 Cosmic rays whose split tracks each had transverse momentum $p_T > 2$ GeV and at least one,
 1246 eight, and 25 hits in the barrels of the Pixel, SCT, and TRT detectors, respectively, were selected to
 1247 measure a collection of track parameters. Figure 4.12 shows the difference in the impact parameter
 1248 Δd_0 and the charge divided by the transverse momentum $\Delta q/p_T$ of the selected split-track cosmic
 1249 rays for both the March and June alignments. Both distributions show a reduction in width in the
 1250 June alignment, corresponding to an improvement in the resolution of each track parameter. The
 1251 Δd_0 plot shows a significant improvement in the June alignment, further validating the removal of
 1252 the bias in the impact parameter.

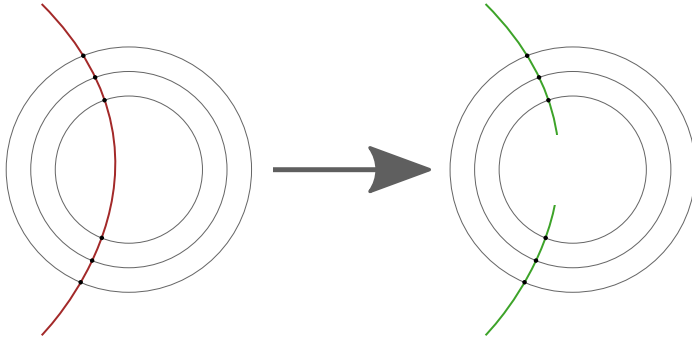


Figure 4.11: Representation of splitting a single cosmic ray track passing through the entire detector (left) into two separate tracks (right).

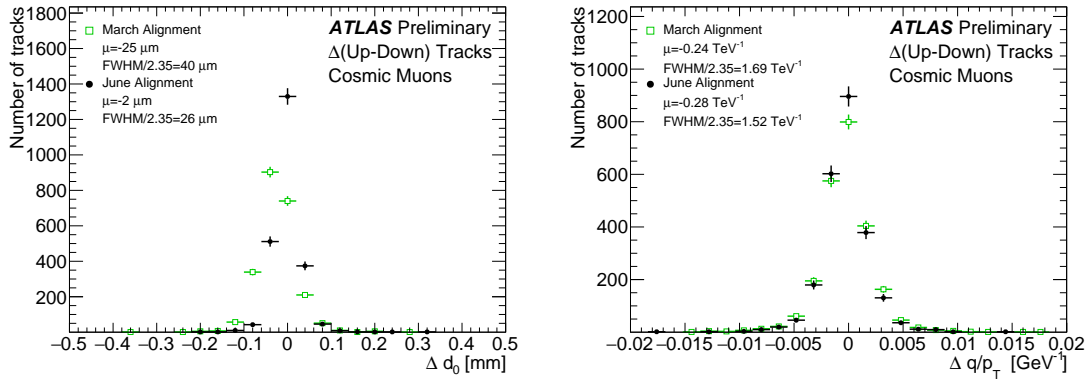


Figure 4.12: Distribution of the difference in the impact parameter Δd_0 (left) and charge over transverse momentum $\Delta q/p_T$ (right) between the two cosmic ray split tracks. The June (black) and March (green) alignments are compared. The distributions are normalized to the same number of entries.

1253 4.2.3 Error scaling

1254 The final step in preparing the new set of June alignment constants deals with the adjustment of
1255 the hit errors, or *error scaling*. Knowledge of the exact position of a hit measurement on a track
1256 is limited by the accuracy with which the sensors' positions are known. Let σ represent the hit
1257 uncertainty used in track fitting, and σ_0 be the detector's intrinsic uncertainty. If $\sigma = \sigma_0$, the pull
1258 of the track-hit residual distributions should form a Gaussian distribution centered at zero with unit
1259 width [53]. In the case of residual misalignment, the pull distributions' standard deviations will
1260 stray from unity. The hit uncertainty can be written as:

$$\sigma = a \cdot \sigma_0 \oplus b \quad (4.12)$$

where a is a scaling factor, and b is a constant term which can be interpreted as a measure of any remaining misalignment of the detector elements. In the June alignment campaign, the value of a was fixed at $a = 1$, and b was evaluated from the residual pull distributions for each subdetector in its sensitive directions.

Once the value of b is determined, pull distributions derived from the new value of σ should have unit width. The error scaling values for each subdetector are listed in Table 4.3, and the pull distributions for the IBL after error scaling are shown in Figure 4.13

Detector	Coordinate	$b(\mu\text{m})$
IBL	x	6.4
	y	43.6
Pixel	x	5.2
	y	28.6
End-caps	x	7.5
	y	0
SCT	Barrel	10.8
	End-caps	8.6
TRT	Barrel	0
	End-caps	0

Table 4.3: Estimated value of the error scaling term b for each subdetector component with the June alignment.

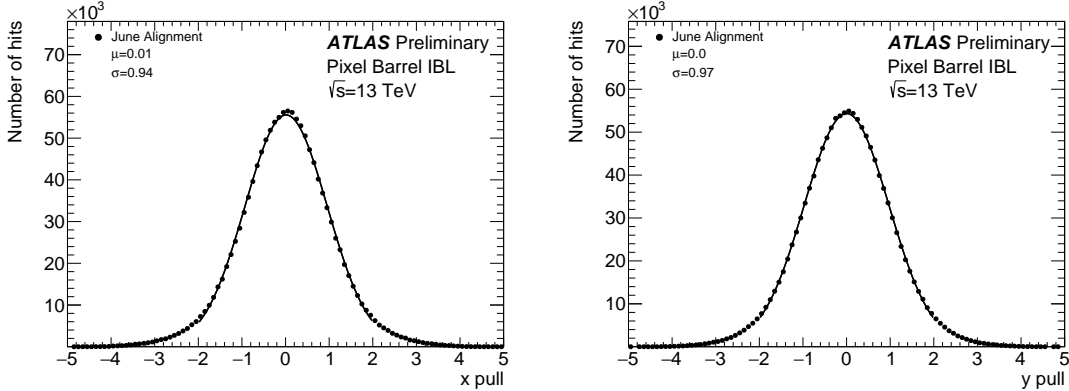


Figure 4.13: Pull distributions in local x (left) and y (right) for the IBL using the $\sqrt{s} = 13 \text{ TeV}$ collision data sample after applying the error scaling.

1268 **4.3 Level 2 alignment of the TRT**

1269 During validation of the final end-of-year reprocessing of the 2015 data, a misalignment was found in
 1270 the barrel of the TRT detector, as several modules (triangular clusters of straws) showed rotations
 1271 in the local y coordinate. The then-best available constants included a full L3 alignment of the
 1272 silicon detectors and a separate L2 alignment of the TRT. However, not all degrees of freedom were
 1273 enabled when the TRT was aligned. To correct for these tilts, an additional four iterations of L2
 1274 alignment was performed on the TRT enabling all available degrees of freedom (T_x , T_y , R_x , R_y , and
 1275 R_z in the barrel, and T_x , T_y , and R_z for the endcaps). Plots of the residual means from barrel ϕ
 1276 sectors containing modules affected by the tilt misalignment are shown in Figure 4.14 before and
 1277 after the L2 alignment.

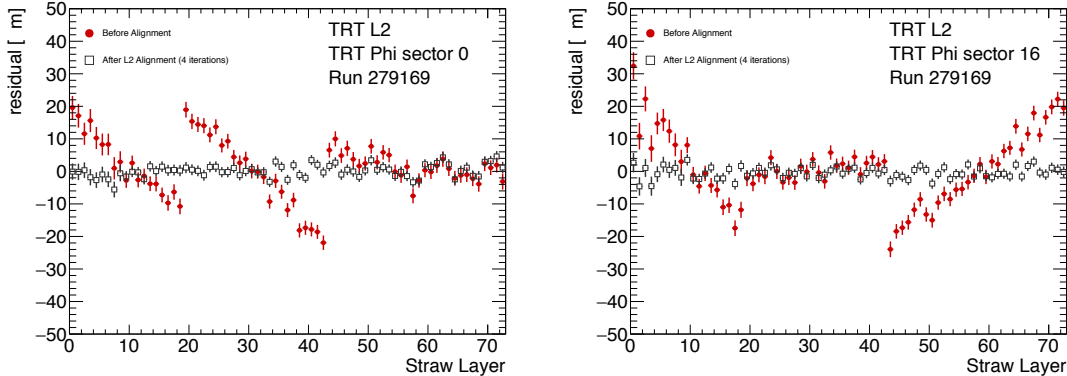


Figure 4.14: Residual means by straw layer in two TRT ϕ -sectors affected by a tilt misalignment. The tilts in each of the three modules are clearly visible in the red points representing the reconstructed data prior to alignment. After four iterations of L2 alignment, the residual means in the gray points are flat.

1278 Following the L2 alignment, some additional time was taken to determine if a full wire-by-wire
 1279 L3 alignment of the TRT was necessary. The TRT was last aligned at L3 during Run 1, but initial
 1280 alignment campaigns in Run 2 did not show signs of misalignment, as can be seen from the residual
 1281 distributions in Figure 4.10. In order to assess the alignment more carefully, two dimensional residual
 1282 maps in ϕ and z were constructed for each layer in the TRT barrel and endcaps using the current
 1283 alignment. These maps were compared to a similar set using the L3 alignment from 2010, from which
 1284 it was determined that the straw-level alignment indeed hadn't degraded and a new L3 alignment
 1285 was not needed. The maps for the first layer of the TRT barrel are shown in Figure 4.15 for both
 1286 sets of alignment constants.

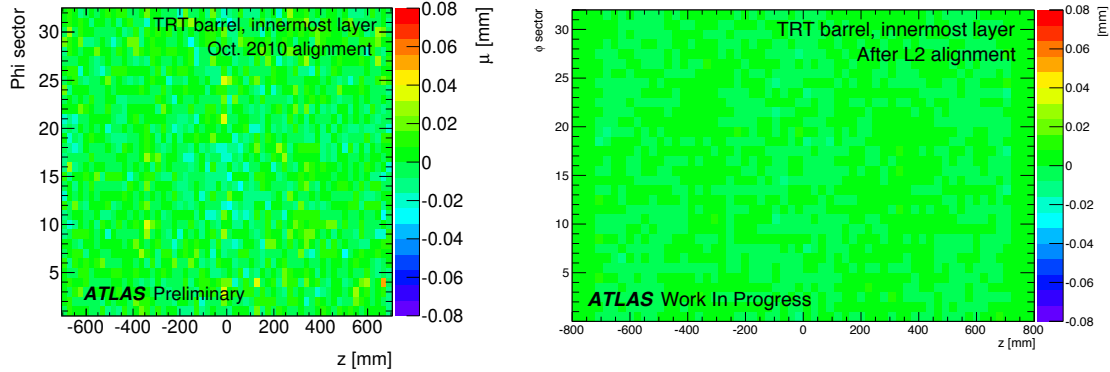


Figure 4.15: Two dimensional map of residuals in the first layer of the TRT barrel vs z and ϕ . Each bin represents the mean of a Gaussian fit to the TRT residuals in that bin. The map on the left is after the L3 (wire-by-wire) alignment of the TRT performed in 2010, and the map on the right is after the L2 alignment at the end of 2015. The z -axis for both plots use the same scale. Left figure taken from [53].

1287 4.4 Momentum bias from sagitta deformations

1288 A variety of weak mode deformations can exist in the detector even after alignment. As mentioned
 1289 previously, these weak modes consist of misalignments which don't affect the χ^2 of the residuals
 1290 and thus are not handled by the basic alignment algorithm. In the presence of a weak mode,
 1291 the description of the detector geometry can still provide efficient and high quality track fits, but
 1292 there may also be systematic biases in one or more track parameters. Several weak modes, their
 1293 impacts on the reconstruction, and the steps taken to eliminate them are detailed in [56, 63]. This
 1294 section focuses specifically on *sagitta* deformations that result in a bias in the reconstructed track
 1295 momentum.

1296 These sagitta distortions consist of detector movements orthogonal to the trajectory of the outgoing
 1297 particle. The effect on the reconstructed track curvature is different for positively and negatively
 1298 charged particles, resulting in a charge-antisymmetric bias. This effect is illustrated in the curl
 1299 deformation shown in Figure 4.16.

1300 In the plane transverse to ATLAS's magnetic field, outgoing particle tracks form circular arcs.
 1301 The sagitta is defined as the distance from the center of this arc to the center of its base, as shown in
 1302 Figure 4.17, and it represents the "amount of bending" in the track. In the case where the sagitta s
 1303 is considerably smaller than the detector radius R_0 , which is a valid assumption when working with

1304 high momentum tracks, the transverse momentum of a particle of charge q can be written as [64]:

$$p_T \propto qB \frac{R_0^2}{8s} \quad (4.13)$$

1305 where B is the strength of the detector's magnetic field. If a sagitta bias is present, the track's
1306 transverse momentum shifts by [63]:

$$q/p_T \rightarrow q/p_T + \delta_s \quad \text{or} \quad p_T \rightarrow p_T \cdot (1 + qp_T\delta_s)^{-1} \quad (4.14)$$

1307 where δ_s is a universal bias parameter that uniquely defines the deformation. Finally, since the
1308 reconstructed polar angle does not change under a sagitta deformation, the longitudinal component
1309 of the momentum scales along with the transverse component, and an equivalent equation can be
1310 written for the total momentum:

$$p \rightarrow p \cdot (1 + qp_T\delta_s)^{-1} \quad (4.15)$$

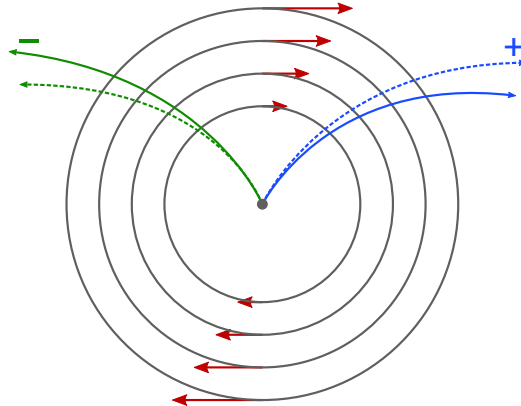


Figure 4.16: Representation of a curl distortion in the detector. The image shows a cutaway in the transverse plane. The deformation is represented by the red arrows, and the impact on the reconstructed positive (blue) and negative (green) tracks are shown. The dashed lines represent the true particle trajectories, and the solid lines represent the reconstructed trajectories.

1311 4.4.1 Sagitta bias monitoring with electron E/p

1312 Since a sagitta bias results in changes in the momentum of particles' tracks as measured by the ID,
1313 they can be identified using independent measurements from other systems in the detector. One
1314 such method involves using the energy-momentum ratio of electrons (E/p). Since the electron's
1315 energy is measured in ATLAS's calorimeter systems, it is not sensitive to any sagitta bias that may
1316 exist in the ID and the corresponding measurement of the track momentum. Under the assumption

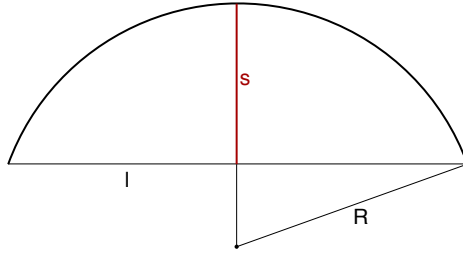


Figure 4.17: Geometric definition of the sagitta s in relation to the length of the chord l and the radius r of a circular arc.

1317 that the calorimeter response is independent of the charge of incoming particles, a charge-dependent
1318 momentum bias in the ID will manifest as a difference in the E/p ratio for electrons and positrons.

1319 In the presence of a sagitta bias, the momentum will change according to Equation 4.15 and the
1320 average measured $\langle E/p \rangle$ can be written as:

$$\langle E/p \rangle^\pm \rightarrow \langle E/p \rangle^\pm \pm \langle E_T \rangle \delta_s \quad (4.16)$$

1321 where the approximation $p_T \approx E_T$ is used. Assuming that $\langle E/p \rangle^+ = \langle E/p \rangle^-$ in the absence of a
1322 bias, the sagitta bias parameter can be written as:

$$\delta_s = \frac{\langle E/p \rangle^+ - \langle E/p \rangle^-}{2\langle E_T \rangle} \quad (4.17)$$

1323 If the kinematic selections for electrons and positrons are identical, the energy scale of the calorimeter
1324 will not factor into the $\langle E/p \rangle$ difference; however, it will affect $\langle E_T \rangle$ which would scale the measured
1325 δ_s . This is expected to be a small effect, as the energy scale for electrons has been measured at
1326 $\sqrt{s} = 13$ TeV with uncertainties on the per-mil level across the entire detector [65].

1327 4.4.1.1 Measuring $\langle E/p \rangle$

1328 The E/p ratio is measured using electrons and positrons from $Z \rightarrow e^\pm e^\mp$ events in order to obtain
1329 a high purity sample of candidate particles. They are required to pass a basic selection criteria to
1330 ensure they are well measured in both the ID and the calorimeters:

- 1331 • $E_T > 25$ GeV
- 1332 • $|\eta| < 2.47$, excluding the calorimeter's barrel-to-endcap transition region in $1.37 < |\eta| < 1.52$
- 1333 • Pass MediumLH identification working point detailed in Section 3.2.4.3

- 1334 ● Pass a selection of quality cuts, including a requirement that the electron be identified using
 1335 cluster information in the calorimeter

 1336 ● The associated track must have at least one hit in the IBL, three in the Pixel detector, and
 1337 five in the SCT detector.

1338 Events with exactly two opposite-charge electrons passing this selection with a dielectron invariant
 1339 mass within 30 GeV of the Z boson mass are then used for the E/p calculation.

1340 Since the size of the sagitta bias δ_s is not expected to be constant across the entire detector,
 1341 a two-dimensional rectangular grid binned in detector η and ϕ is constructed. From the selected
 1342 events, separate distributions of E/p are made for electrons and positrons lying in each bin. Each
 1343 distribution is fit with Crystal Ball function¹¹, and the peak of the distribution is taken as the value
 1344 of $\langle E/p \rangle$. If there is no bias on the track momentum in the bin, the peaks for electrons and positrons
 1345 should agree. Example E/p distributions including the Crystal Ball fits are shown in Figure 4.18.

1346 It is important to emphasize that deviations from one in the *ratio* of $\langle E/p \rangle$ for electrons and
 1347 positrons indicates that a momentum bias may be present. The value of $\langle E/p \rangle$ itself is not expected
 1348 to equal one exactly, as the track momentum on average tends to be slightly lower than the energy
 1349 measurement in the calorimeter. This is due to the fact that if the electron were to radiate a photon,
 1350 its momentum would change slightly, while it is likely that both the electron and the emitted photon
 1351 would leave energy deposits near each other in the calorimeter and be reconstructed into the same
 1352 object.

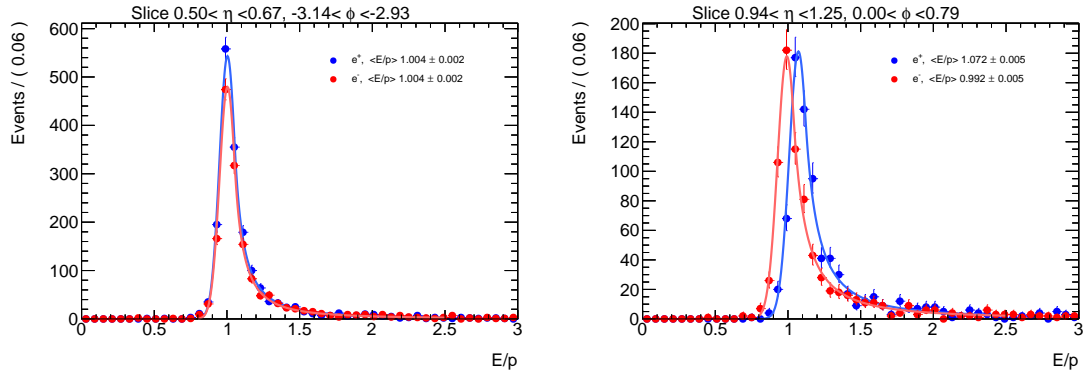


Figure 4.18: E/p distributions of electrons and positrons in two different $\eta\phi$ bins of the detector. The left hand plot is taken from a region with no momentum bias where $\langle E/p \rangle^+ = \langle E/p \rangle^-$, while the right hand plot shows an 8% disagreement in $\langle E/p \rangle$ between electrons and positrons.

¹¹The Crystal Ball function is a probability density function consisting of a Gaussian core and a power-law tail.

1353 Once the $\langle E/p \rangle^\pm$ distributions in each $\eta\text{-}\phi$ bin have been extracted from the fits, a two dimensional map of δ_s can be constructed using Equation 4.17. The map gives an overview of sagitta
 1354 biases that may be present in the detector, and can be used by the alignment algorithm to reduce
 1355 the bias in the next iteration. In this case, the tracks fed to the alignment have their momenta
 1356 corrected according to [63]:

$$q/p_{\text{corr}} = q/p_{\text{reco}}(1 - qp_T\delta_s) \quad (4.18)$$

1358 where p_{reco} is the reconstructed momentum of the track. The corrected momentum is then constrained in the alignment.
 1359

1360 4.4.1.2 Results in 13 TeV data

1361 The E/p method has been used to monitor sagitta biases in the detector several times over the
 1362 course of Run 2. During this time, it has primarily served as an independent cross-check to a
 1363 second method using $Z \rightarrow \mu^\pm\mu^\mp$ events [63]. The $Z \rightarrow \mu^\pm\mu^\mp$ method identifies individual track
 1364 momentum biases through shifts in the reconstructed Z mass, which leaves it relatively insensitive
 1365 to global sagitta biases. For this reason, the sagitta bias maps produced using this technique are
 1366 normalized to those from the E/p method before being used to constrain the alignment. The results
 1367 of two implementations of the E/p method are presented here.

1368 1. The first follows the end-of-year reprocessing of the entire ATLAS 2016 data set. Two sets of
 1369 alignment constants are compared: the *prompt* alignment, which was derived shortly after each
 1370 run was recorded, and the *reprocessed* alignment. The maps of the sagitta bias comparing the
 1371 two alignments calculated using the E/p method are shown in Figure 4.19, and the comparison
 1372 of the η projection of each map is shown in Figure 4.20.

1373 2. The second uses the 2017 data after reprocessing, and compares the effects of multiple it-
 1374 erations of the method. In each iteration, the momenta of the electrons and positrons are
 1375 corrected based on Equation 4.15 using the value of δ_s computed in the previous iteration,
 1376 and a new sagitta bias map is calculated. If the method is indeed characterizing the sagitta
 1377 biases correctly, the corrections should converge quickly. The initial sagitta bias map is com-
 1378 pared to the map after two such iterations in Figure 4.21, and the sagitta bias projected along
 1379 η for each iteration is shown in Figure 4.22. Indeed, after just two iterations, δ_s is consistent
 1380 with zero in nearly all bins.

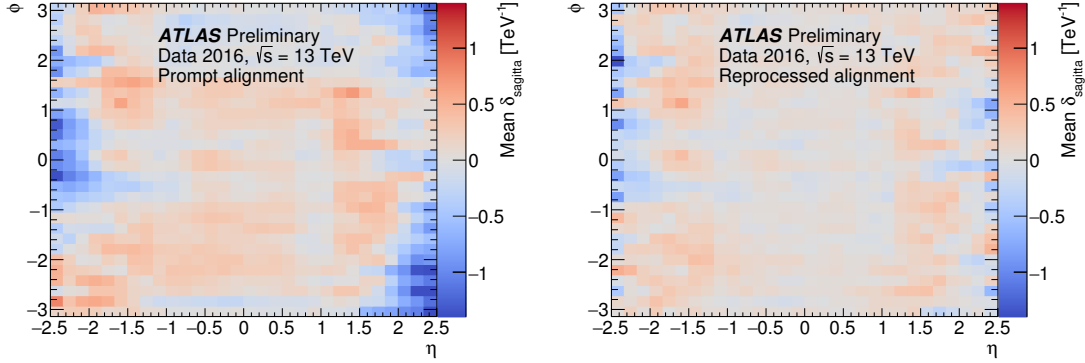


Figure 4.19: Sagitta bias in the $\sqrt{s} = 13 \text{ TeV}$ data collected by ATLAS in 2016 as a function of η and ϕ for the prompt (left) and reprocessed (right) alignments using the E/p method.

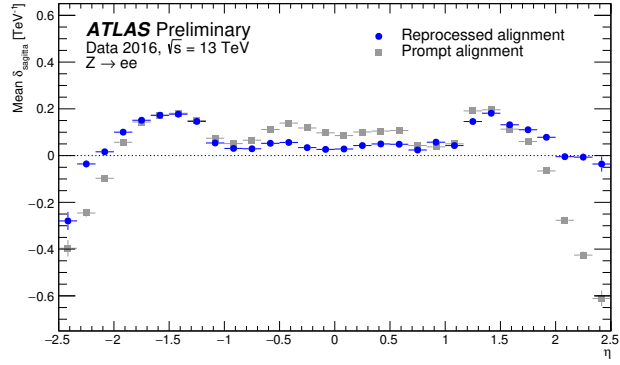


Figure 4.20: Sagitta bias in the $\sqrt{s} = 13 \text{ TeV}$ data collected by ATLAS in 2016 projected along η for the prompt (gray) and reprocessed (blue) alignments using the E/p method.

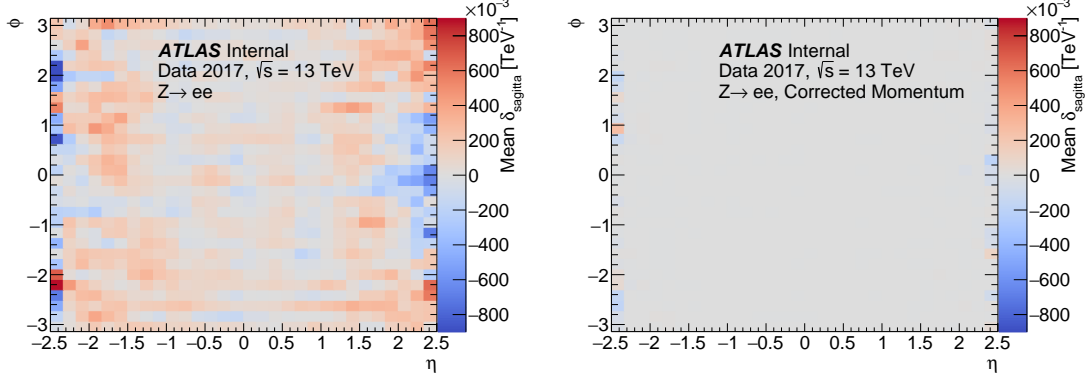


Figure 4.21: Sagitta bias in the $\sqrt{s} = 13 \text{ TeV}$ data collected by ATLAS in 2017 as a function of η and ϕ in reconstructed electrons (left) and after two iterations of momentum corrections (right) from the E/p method.

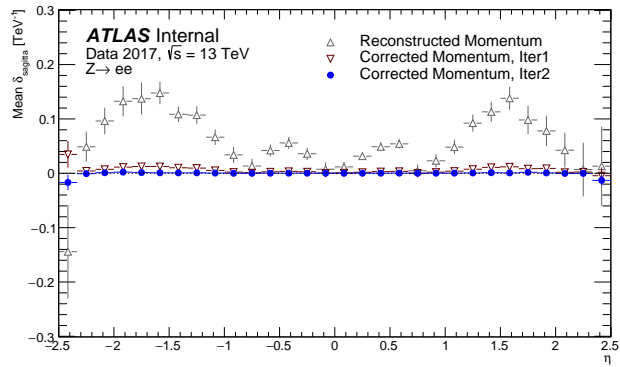


Figure 4.22: Sagitta bias in the $\sqrt{s} = 13$ TeV data collected by ATLAS in 2017 projected along η in reconstructed electrons (gray) and after one (red) and two (blue) iterations of momentum corrections from the E/p method.

1381

CHAPTER 5

1382

1383

Measurement of same-sign WW production at $\sqrt{s} = 13$ TeV with ATLAS

1384 Production of same-sign W boson pairs is a particularly interesting SM process. When produced
1385 via vector boson scattering (VBS), $W^\pm W^\pm jj$ is sensitive to the electroweak symmetry breaking
1386 (EWSB) mechanism as well as potential Beyond the Standard Model (BSM) physics processes.
1387 $W^\pm W^\pm jj$ events can be produced via electroweak-mediated (EWK) diagrams, of which VBS is a
1388 subset, or QCD-mediated diagrams. The biggest advantage of same-sign $W^\pm W^\pm jj$ over other VBS
1389 processes lies in its ratio of electroweak (EWK) to QCD production cross sections. Despite the
1390 opposite-sign $W^\pm W^\mp$ having a larger total cross section, its EWK-mediated diagrams are much
1391 smaller than its QCD-mediated diagrams, while for same-sign $W^\pm W^\pm$ the EWK production is
1392 considerably larger. This makes $W^\pm W^\pm jj$ one of the premier channels for studying VBS at the
1393 LHC.

1394 The first evidence of electroweak (EWK) $W^\pm W^\pm jj$ production was seen by the ATLAS and CMS
1395 experiments at $\sqrt{s} = 8$ TeV with excesses of 3.6σ [66] and 2.0σ [67] over backgrounds, respectively.
1396 More recently, ATLAS and CMS have both observed the EWK process at $\sqrt{s} = 13$ TeV with
1397 significances of 6.9σ [68] and 5.5σ [69], respectively. The ATLAS $\sqrt{s} = 13$ TeV observation and
1398 cross section measurement of EWK-produced $W^\pm W^\pm jj$ is presented in this chapter [68, 70].

1399 5.0.1 Experimental overview of vector boson scattering

1400 VBS processes are very important to understand due to their sensitivity to the EWSB mechanism.
1401 As explained in Section 2.3, in the absence of a light SM Higgs boson, the scattering amplitude of
1402 longitudinally polarized vector bosons grows with center-of-mass energy. However, once the Higgs

1403 is introduced, the divergences cancel and the cross section no longer grows unbounded.

1404 With the discovery of the Higgs boson in 2012 [17, 18], the EWSB mechanism can now be directly
 1405 studied. Due to the potential exchange of a Higgs boson in the VBS diagrams ($W^\pm W^\pm jj$ itself does
 1406 not contain an s -channel Higgs exchange), VBS processes are directly sensitive to properties of the
 1407 Higgs. For example, the high-mass tail in the VV scattering system allows an approximation of the
 1408 effective coupling strength of the Higgs to vector bosons that is independent of any assumptions
 1409 on the Higgs width [71]. Additionally, the center of mass energy dependence of the VV scattering
 1410 can reveal whether the Higgs boson unitarizes the longitudinal scattering amplitude fully or only
 1411 partially [72].

1412 VBS events are characterized by two quarks from the colliding protons each radiating a vector
 1413 boson which then scatter and decay in the detector. The incoming quarks carry a large amount of
 1414 momentum and only deflect a small amount upon emitting the vector boson; as a result, they often
 1415 enter the calorimeters very close to the beam line. Ignoring the decay products of the scattered
 1416 bosons for now, these VBS events result in a final state of two vector bosons (V) and two jets (j)
 1417 at high pseudorapidities (called *forward jets* or *tag jets*) from the outgoing quarks. The shorthand
 1418 $VVjj$ is used to represent this final state.

1419 $VVjj$ events can be produced via two different physical processes. The first involves purely
 1420 electroweak interactions in the tree-level diagrams, of order $\mathcal{O}(\alpha_{\text{EWK}}) = 6$ in the electroweak coupling
 1421 constant, and will be referred to as *EWK production*. This can be further broken down into VBS
 1422 and non-VBS events. In the VBS EWK production, the scattering occurs via triple or quartic gauge
 1423 couplings, as well as the exchange of a Higgs boson. The non-VBS EWK production contains the
 1424 same final state of two vector bosons and two outgoing quarks, but the bosons do not scatter. Due to
 1425 gauge invariance, it is not possible to separate the VBS from the non-VBS productions [73]; therefore,
 1426 both are included in the signal generation and are indistinguishable from one another. The second
 1427 process involves a mix of the EWK and strong interactions, of order $\mathcal{O}(\alpha_s) = 2 \otimes \mathcal{O}(\alpha_{\text{EWK}}) = 4$, and
 1428 will be referred to as *QCD production*. The tree-level Feynman diagrams for VBS EWK, non-VBS
 1429 EWK, and QCD $VVjj$ production are found in Figures 5.1, 5.2, and 5.3, respectively.

1430 5.0.2 Same-sign $W^\pm W^\pm$ scattering

1431 Same-sign $W^\pm W^\pm jj$ scattering is considered to be one of the best channels for studying VBS at the
 1432 LHC due to its favorable ratio of EWK to QCD production [71]. Since the VBS diagrams (which are
 1433 a subset of the total EWK production) are the primary source of interest for an analysis, the QCD

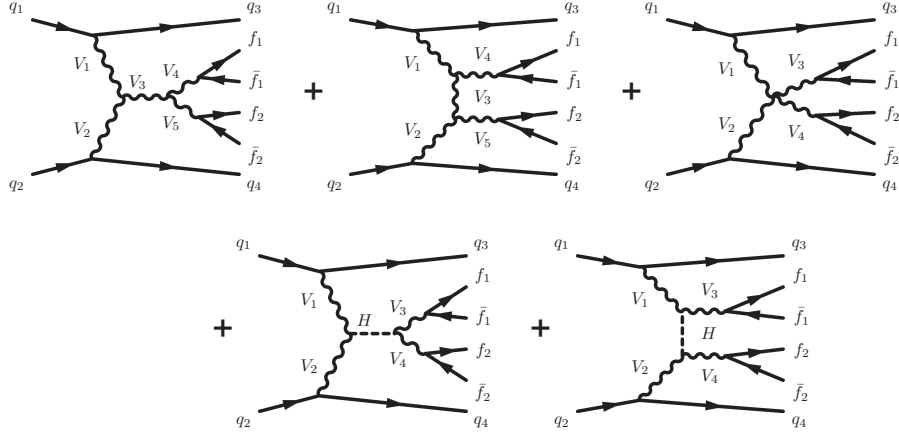


Figure 5.1: Tree-level Feynman diagrams for VBS EWK $VVjj$ production including triple gauge couplings involving W and/or Z bosons (top left and top middle), quartic gauge coupling (top right), or the exchange of a Higgs boson (s -channel bottom left and t -channel bottom right). The labels are quarks (q), fermions (f), and gauge bosons ($V = W, Z$).

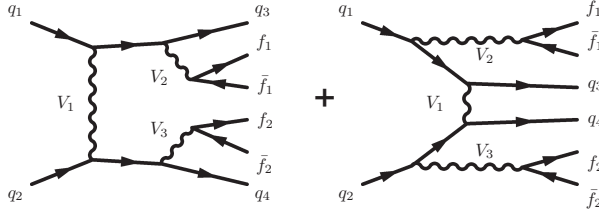


Figure 5.2: Tree-level Feynman diagrams for non-VBS EWK $VVjj$ production. The labels are quarks (q), fermions (f), and gauge bosons ($V = W, Z$).

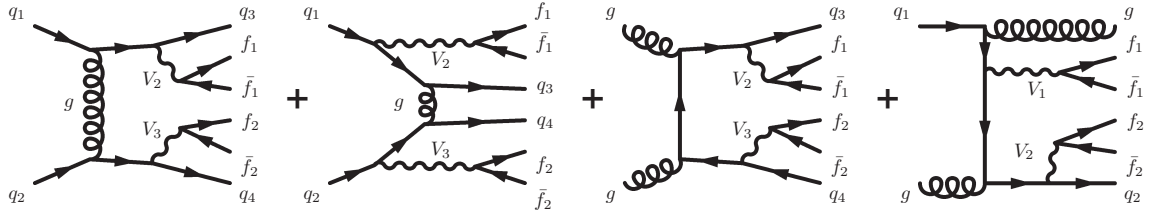


Figure 5.3: Tree-level Feynman diagrams for QCD $VVjj$ production. The labels are quarks (q), fermions (f), and gauge bosons ($V = W, Z$).

1434 production would be considered a background in an analysis. Therefore a higher EWK-to-QCD
 1435 ratio results in increased sensitivity to VBS. EWK and QCD cross sections at $\sqrt{s} = 13$ TeV for
 1436 six leptonic $VVjj$ final states were calculated using the **SHERPA** MC generator in a VBS-enriched
 1437 fiducial phase space in [74]. Despite its relatively low total cross section compared to some other
 1438 $VVjj$ processes, the EWK-to-QCD ratio for $W^\pm W^\pm jj$ is 10-20 times higher than for other processes
 1439 after applying VBS-enhancing selection criteria.

Final state	Process	σ_{EWK} [fb]	σ_{QCD} [fb]	$\sigma_{\text{EWK}}/\sigma_{\text{QCD}}$
$l^\pm l^\mp l^\pm l^\mp jj$	ZZ	0.098	0.100	0.98
$l^\pm l^\pm l^\mp \nu jj$	$W^\pm Z$	2.34	4.38	0.53
$l^\pm l^\mp \nu \nu jj$	$W^\pm W^\mp, ZZ$	12.3	21.8	0.56
$l^\pm l^\pm \nu \nu jj$	$W^\pm W^\pm$	3.97	0.346	11.47
$l^\pm \nu \nu \nu jj$	$W^\pm Z$	7.64	15.5	0.49
$\nu \nu \nu \nu jj$	ZZ	1.68	1.38	1.22

Table 5.1: Predicted cross sections for EQK and QCD production of diboson processes relevant to VBS at $\sqrt{s} = 13$ TeV using the **SHERPA** MC generator. The numbers for the $W^\pm W^\pm jj$ process are bolded. Leptons are required to have $p_T \geq 25$ GeV and lie within $|\eta| \leq 2.5$ with $m_l > 20$ GeV, and at least two jets are required with $p_T \geq 30$ GeV and $|\eta| < 4.5$. The VBS contributions are enhanced by requiring the dijet invariant mass $m_{jj} > 500$ GeV and dijet separation $\Delta y_{jj} > 2.4$. Numbers taken from [74].

1440 This analysis studies $W^\pm W^\pm jj$ scattering where both W bosons decay leptonically to $e\nu$ or $\mu\nu$ ¹².
 1441 The $W^\pm W^\pm jj$ VBS final state consists of two leptons with the same electric charge, two neutrinos,
 1442 and two high energy forward jets with a large invariant mass. Tree-level Feynman diagrams of VBS
 1443 $W^\pm W^\pm jj$ production can be found in Figure 5.4 and a visual representation of the VBS topology
 1444 can be found in Figure 5.5.

1445 The two tag jets in the characteristic VBS signature also serve as a powerful tool to suppress
 1446 the QCD production mode. In EWK events, the two jets tend to have much higher separation and
 1447 a larger combined invariant mass than the two leading jets in a QCD event. The two plots shown
 1448 in Figure 5.6 highlight the differences in these dijet quantities between the two production modes.
 1449 Finally, an ATLAS event display of a real $W^\pm W^\pm jj$ candidate event is shown in Figure 5.7.

1450 5.0.3 Overview of backgrounds

1451 In addition to QCD production of $W^\pm W^\pm jj$ events, there are several other processes with a final
 1452 state of two same-sign leptons, two neutrinos, and two jets. However, due to the ± 2 final state charge,

¹²Throughout the rest of this chapter, unless stated otherwise, l denotes either electrons (e) or muons (μ), and ν denotes a neutrino. Additionally, e , μ , and ν with no charge or anti-particle designation refer interchangeably to either the particle or anti-particle.

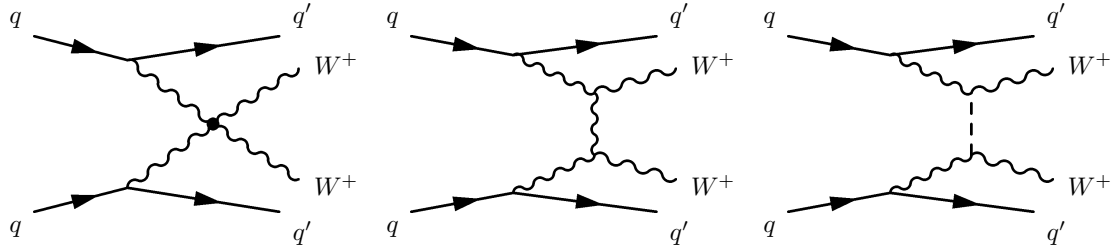


Figure 5.4: Leading order Feynman diagrams for VBS EWK production of $W^\pm W^\pm jj$ events. The leftmost diagram contains a quartic gauge coupling vertex, and the rightmost diagram contains an exchange of a Higgs boson.

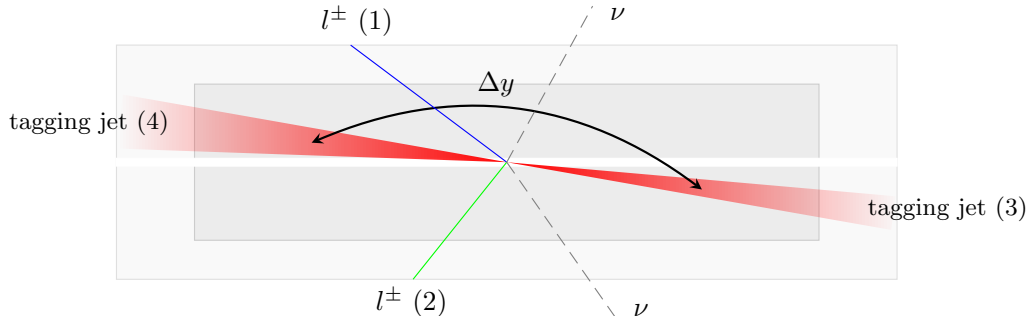


Figure 5.5: $W^\pm W^\pm jj$ VBS event topology containing two leptons (1 and 2) with the same electric charge, two neutrinos, and two forward tagging jets (3 and 4) with large rapidity separation Δy .

1453 there is a considerable reduction in SM backgrounds (such as Z boson events) when compared to
 1454 an analysis like opposite-sign $W^\pm W^\mp jj$.

1455 One of the largest sources of background involves processes with prompt leptons¹³. These are
 1456 events that contain two leptons with the same electric charge and one or more additional leptons that
 1457 are “lost”, either by failing the selection criteria or falling outside of the detector’s acceptance. The
 1458 number of processes that can contribute is limited by the requirement of same-sign leptons, and as a
 1459 result this background is dominated by multi-boson processes, with the largest contribution coming
 1460 from WZ events and smaller contributions from ZZ and $t\bar{t} + V$ events. Triboson events where one
 1461 boson decays hadronically also contribute to this background; however, the jets are generally softer
 1462 and more central than in a typical VBS event, and the cuts applied on the forward jets suppress
 1463 these contributions.

¹³Prompt leptons are those that are produced in the primary collision and are a direct decay product of the process of interest. Non-prompt leptons originate from some secondary process, such as a b -hadron decay, or are jets that get mis-reconstructed as a lepton.

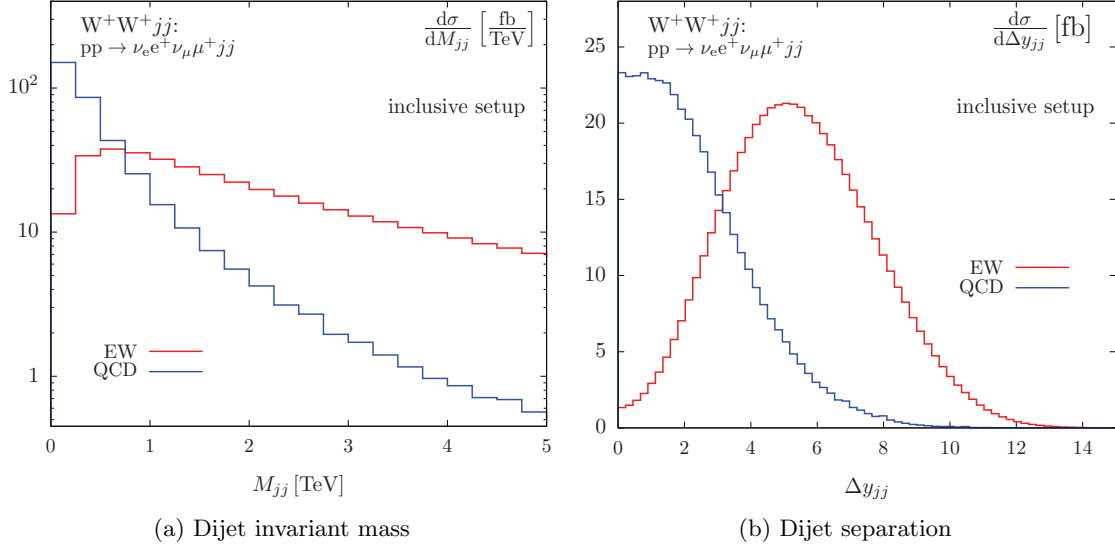


Figure 5.6: Generator level comparisons at $\sqrt{s} = 7$ TeV of dijet invariant mass (M_{jj} , left) and dijet rapidity (Δy_{jj} , right) in EWK (red) and QCD (blue) $W^\pm W^\pm jj$ events with no selection cuts applied. Plots taken from [75].

1464 The other dominant background comes from non-prompt, or “fake”, leptons. Here one or more
 1465 leptons originate from the decay of another particle unrelated to the signal process, such as a heavy-
 1466 flavor decay or photon conversion, or come from a jet that is misidentified as a lepton. This back-
 1467 ground is mostly made up of events from $t\bar{t}$ and $W+jets$ processes, with a much smaller contribution
 1468 from conversions in $V\gamma$ events.

1469 Finally, opposite-sign lepton pairs can enter the signal region if one of the leptons is reconstructed
 1470 with the wrong charge (called *charge misidentification*¹⁴). In practice, this only affects events with
 1471 electrons, as the charge misidentification rate for muons is negligible [76]. This is a major background
 1472 in events with two electrons, but it is a much smaller contribution for events with one electron and
 1473 one muon.

1474 5.1 Data and Monte Carlo samples

1475 This analysis uses 36.1 fb^{-1} of $\sqrt{s} = 13$ TeV proton-proton collisions recorded by ATLAS during
 1476 the 2015 and 2016 data taking periods. The uncertainty in the combined integrated luminosity is
 1477 2.1%. It is derived following a methodology similar to that detailed in [77] and using the LUCID-2

¹⁴Charge misidentification is also referred to interchangeably as *charge mis-ID* and *charge flip*.

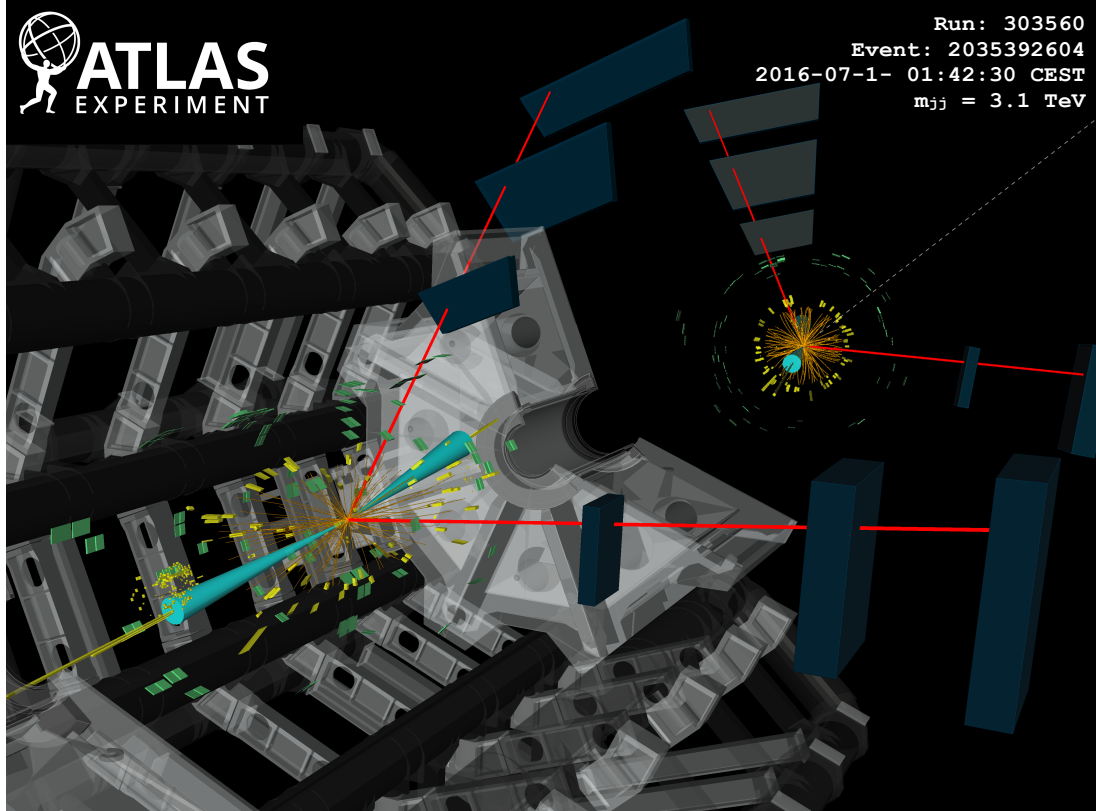


Figure 5.7: ATLAS event display of a $pp \rightarrow W^+W^+ \rightarrow \mu^+\nu_\mu\mu^+\nu_\mu jj$ event. The muons are represented by the red lines travelling from the ID through the MS, and the forward jets are represented by the blue cones with yellow energy deposits in the calorimeters. The direction of the E_T^{miss} in the transverse plane is indicated by the gray dashed line in the inset image. Event display taken from [68].

1478 detector for the baseline luminosity measurements [78] from calibration of the luminosity scale using
 1479 x - y beam-separation scans.

1480 **5.1.1 Monte Carlo samples**

1481 A number of Monte Carlo (MC) simulations are employed to model signal and background processes.
 1482 In order to model the real collision data as closely as possible, each MC sample has been passed
 1483 through a full simulation of the ATLAS detector in GEANT4 [79, 80], and events have been recon-
 1484 structed using the same algorithms as the data. The simulation reproduces as closely as possible
 1485 the momentum resolutions and calorimeter responses of the detector, and also includes the effects
 1486 of pileup by including soft QCD interactions using PYTHIA v8.1 [81]. The MC samples used in this

Process	Generator	Comments
$W^\pm W^\pm jj$ (EWK)	SHERPA v2.2.2	Signal sample
$W^\pm W^\pm jj$ (EWK)	POWHEG-BOX v2	Systematics sample
$W^\pm W^\pm jj$ (QCD)	SHERPA v2.2.2	
Diboson	SHERPA v2.2.2	Both bosons decay leptonically ($llll$, $ll\nu\nu$, $l\nu\nu\nu$)
	SHERPA v2.2.1	One boson decays leptonically, the other hadronically
Triboson	SHERPA v2.1.1	
$W+jets$	SHERPA v2.2.1	
$Z+jets$	Madgraph5_aMC@NLO	
$V\gamma$	SHERPA v2.1.1	
$V\gamma jj$ (EWK)	SHERPA v2.2.4	
$t\bar{t}V$	Madgraph5_aMC@NLO	
$t\bar{t}$	POWHEG-BOX v2	
Single top	POWHEG-BOX v1	EWK t -, s -, & Wt -channels

Table 5.2: Summary of MC samples used in the analysis.

1487 analysis are detailed in this section and summarized in Table 5.2.

1488 The $W^\pm W^\pm jj$ samples are modeled using SHERPA v2.2.2 [82, 83, 84] with the NNPDF3.0 PDF
 1489 set [85]. The EWK signal samples were generated by fixing the electroweak coupling constant to
 1490 $\mathcal{O}(\alpha_W) = 6$, and a QCD background sample was also generated with $\mathcal{O}(\alpha_W) = 4$. SHERPA includes
 1491 up to one parton at next-to-leading order (NLO) and up to three at leading order (LO) in the strong
 1492 coupling constant α_s . A second $W^\pm W^\pm jj$ EWK sample was generated using POWHEG-BOX v2 [86]
 1493 with the NNPDF3.0 PDF set and at NLO accuracy. This sample is only used for systematic studies,
 1494 as POWHEG-BOX does not include resonant triboson contributions in its matrix element, which are
 1495 non-negligible at NLO [87].

1496 Diboson processes (VV where $V = W, Z$) are simulated with SHERPA v2.2.2 for mixed hadronic
 1497 and leptonic decays and SHERPA v2.2.1 for fully leptonic decays of the bosons. Similarly, triboson
 1498 (VVV) and $V\gamma$ processes are simulated using SHERPA v2.1.1 with up to one parton at NLO and up
 1499 to three at LO. $W+jets$ processes are simulated with SHERPA v2.2.1 with up to two partons at NLO
 1500 and four at LO. All the above SHERPA samples use the NNPDF3.0 PDF set and SHERPA's own parton
 1501 showering. The $Z+jets$ events are generated with Madgraph5_aMC@NLO [88] at LO and interfaced
 1502 with PYTHIA v8.1 for parton showering.

1503 $t\bar{t}V$ events are generated using POWHEG-BOX v2 with the CT10 PDF set [89]. $t\bar{t}V$ samples are
 1504 generated at NLO with Madgraph5_aMC@NLO and the NNPDF3.0 PDF set interfaced with PYTHIA v8
 1505 for parton showering. Finally, single top events are generated with POWHEG-BOX v1 and the CT10f4
 1506 PDF set interfaced with PYTHIA v6 [90] for parton showering.

1507 5.2 Object and event selection

1508 This section details the selection criteria for objects used in the analysis as well as the selection for
1509 signal events.

1510 5.2.1 Object selection

1511 Muons, electrons, and jets all must pass strict selection requirements to ensure that only high quality,
1512 well measured objects are used. For leptons, a baseline selection is defined (called the *preselection*),
1513 which all leptons must pass in order to be considered for the analysis. This preselection is an
1514 intentionally loose set of criteria designed to have high acceptance in order to reject backgrounds
1515 with additional leptons (i.e. $WZ \rightarrow 3l\nu jj$). Signal leptons are then required to satisfy a much
1516 tighter *signal selection* aimed at suppressing backgrounds from non-prompt or fake leptons. A third
1517 set of lepton selection criteria, the *loose selection*, defines a sample enriched in non-prompt leptons,
1518 and it is used in the fake-factor method for estimating the non-prompt background, discussed in
1519 detail in Section 5.3.4. Jets are only required to pass one set of selection criteria. These selections
1520 are detailed in the following sections and summarized in Table 5.3 for muons, Table 5.4 for electrons,
1521 and Table 5.5 for jets.

1522 5.2.1.1 Muon candidate selection

1523 Cuts on muon p_T serve to reject low momentum leptons from background processes and additional
1524 collisions from pileup events. Preselected muons must have transverse momentum $p_T > 6$ GeV, and
1525 the signal muons must pass $p_T > 27$ GeV. The p_T requirement for loose muons is lower than for
1526 signal muons, at $p_T > 15$ GeV, for reasons that are discussed in Section 5.3.4.3. Muons are required
1527 to fall within the detector's η acceptance: $|\eta| < 2.7$ for preselected muons, which is tightened to
1528 $|\eta| < 2.5$ for the signal muons.

1529 Cuts on the transverse and longitudinal impact parameters are applied to ensure that the can-
1530 didate muon originated from the primary particle interaction and not some other source, such as a
1531 heavy flavor decay. The preselection and the loose selection both have relaxed requirements on the
1532 transverse impact parameter significance (d_0/σ_{d_0}) than the signal selection; all three have the same
1533 requirement on the transverse impact parameter ($|z_0 \times \sin \theta|$).

1534 Finally, the muon candidates are required to pass a particle identification and an isolation criteria
1535 as defined in [91]. The methods used in constructing the identification and isolation working points
1536 are described in more detail in Section 3.2.4.2. The muon identification serves to select prompt

1537 muons with high efficiency and well measured momenta. This analysis uses two different working
 1538 points: **Loose** for preselected muons and **Medium** for loose and signal muons, where **Medium** muons
 1539 are a tighter subset of those that pass the **Loose** requirement. Muon isolation is a measurement
 1540 of detector activity around the muon candidate, and it is measured with both track-based and
 1541 calorimeter-based variables. The isolation working point used for the signal muons, **Gradient**, is
 1542 defined such that there is 90% or better background rejection efficiency for 25 GeV muons, and 99%
 1543 efficiency at 60 GeV. There is no minimum isolation requirement for preselected or loose muons.
 1544 Loose muons are additionally required to fail one or both of the signal transverse impact parameter
 1545 cut and signal isolation requirement.

Muon preselection	
Momentum cut	$p_T > 6$ GeV
Angular acceptance	$ \eta < 2.7$
Longitudinal impact parameter	$ z_0 \times \sin \theta < 0.5$ mm
Transverse impact parameter	$d_0/\sigma_{d_0} < 10$
Particle identification	Loose

Muon signal selection	
Momentum cut	$p_T > 27$ GeV
Angular acceptance	$ \eta < 2.5$
Longitudinal impact parameter	$ z_0 \times \sin \theta < 0.5$ mm
Transverse impact parameter	$d_0/\sigma_{d_0} < 3$
Particle identification	Medium
Particle isolation	Gradient

Muon loose selection	
Momentum cut	$p_T > 15$ GeV
Angular acceptance	$ \eta < 2.5$
Longitudinal impact parameter	$ z_0 \times \sin \theta < 0.5$ mm
Transverse impact parameter	$d_0/\sigma_{d_0} < 10$
Particle identification	Medium
Fail signal transverse impact parameter and/or isolation cuts	

Table 5.3: Muon selection criteria. All muons are required to pass the preselection (top), and then either the signal (middle) or loose (bottom) criteria is applied to the preselected electrons.

1546 5.2.1.2 Electron candidate selection

1547 The electron candidate selections are very similar to those for muons. The p_T cut starts at $p_T >$
 1548 6 GeV for the preselection, increases to $p_T > 20$ GeV for loose electrons, and finally to $p_T > 27$ GeV

for signal electrons. The $|\eta|$ cut for electrons requires $|\eta| < 2.47$ for all electrons, with the region $1.37 \leq |\eta| \leq 1.52$ removed from loose and signal electrons. This is where the electromagnetic calorimeter transitions from the barrel to the endcaps and is not fully instrumented. Both the transverse and longitudinal impact parameter cuts are the same for all electron selections.

The electron particle identification uses a multivariate likelihood technique (LH) [92] detailed in Section 3.2.4.3. Preselected electrons must pass the `LooseLH` working point with an additional requirement that there be a reconstructed track hit in the first layer of the pixel detector (a so-called B -layer hit). The LH requirement for the loose and signal electrons increases in tightness using `MediumLH` and `TightLH` electrons, respectively. As for isolation, the `Gradient` working point is required for signal electrons only. The loose electrons must fail one or both of the signal identification and isolation requirements.

Electron preselection	
Momentum cut	$p_T > 6$ GeV
Angular acceptance	$ \eta < 2.47$
Longitudinal impact parameter	$ z_0 \times \sin \theta < 0.5$ mm
Transverse impact parameter	$d_0/\sigma_{d_0} < 5$
Particle identification	<code>LooseLH</code> + B -layer hit

Electron signal selection	
Momentum cut	$p_T > 27$ GeV
Angular acceptance	$ \eta < 2.47$, excluding $1.37 \leq \eta \leq 1.52$
Longitudinal impact parameter	$ z_0 \times \sin \theta < 0.5$ mm
Transverse impact parameter	$d_0/\sigma_{d_0} < 5$
Particle identification	<code>TightLH</code>
Particle isolation	<code>Gradient</code>

Electron loose selection	
Momentum cut	$p_T > 20$ GeV
Angular acceptance	$ \eta < 2.47$, excluding $1.37 \leq \eta \leq 1.52$
Longitudinal impact parameter	$ z_0 \times \sin \theta < 0.5$ mm
Transverse impact parameter	$d_0/\sigma_{d_0} < 5$
Particle identification	<code>MediumLH</code>
Fail signal identification and/or isolation cuts	

Table 5.4: Electron selection criteria. All electrons are required to pass the preselection (top), and then either the signal (middle) or loose (bottom) criteria is applied to the preselected electrons.

1560 **5.2.1.3 Jet candidate selection**

1561 The final objects that need to pass selection are jets. Jets are clustered using the anti- k_t algo-
 1562 rithm [93] within a radius of $\Delta R = 0.4$. The jets are then calibrated using E_T - and η -dependent
 1563 correction factors that are trained using MC simulations [94]. The calibrated jets are required to have
 1564 $p_T > 30$ GeV if they lie in the forward regions of the detector ($2.4 < |\eta| < 4.5$) and $p_T > 25$ GeV in
 1565 the central region ($|\eta| \leq 2.4$). In order to suppress pileup jets, the so-called jet-vertex-tagger (JVT)
 1566 discriminant associates a jet with the primary interaction vertex [95]; central jets with $p_T > 60$ GeV
 1567 are required to pass the `Medium` JVT working point, which corresponds to an average efficiency
 1568 of over 92%. Finally, the jets are required to be separated from the selected leptons by at least
 1569 $\Delta R(j, l) > 0.3$.

Jet selection	
Momentum cut	$p_T > 30$ GeV for $2.4 < \eta < 4.5$ $p_T > 60$ GeV for $ \eta < 2.4$
JVT cut	<code>Medium</code>
Jet-lepton separation	$\Delta R(j, l) > 0.3$

Table 5.5: Jet selection criteria. All jets are required to pass the above selection in order to be used in the analysis.

1570 **5.2.1.4 Treatment of overlapping objects**

1571 In the event that one or more objects are reconstructed very close to each other, there is the possibility
 1572 for double-counting if both originated from the same object. The procedure by which this ambiguity
 1573 is resolved is called *overlap removal* (OR). The standard ATLAS recommendation for OR [96, 97]
 1574 is implemented in this analysis and is summarized in Table 5.6.

1575 Since electrons leave a shower in the EM calorimeter, every electron has a jet associated with
 1576 it. Therefore, any jets close to an electron (within $\Delta R(e, j) < 0.2$) are rejected due to the high
 1577 probability that they are the same object. On the other hand, when jets and electrons overlap
 1578 within a larger radius of $0.2 < \Delta R(e, j) < 0.4$, it is likely that the electron and jet both are part of
 1579 a heavy-flavor decay, and the electron is rejected.

1580 High energy muons can produce photons via bremsstrahlung radiation or collinear final state
 1581 radiation which result in nearby energy deposits in the calorimeters. Non-prompt muons from
 1582 hadronic decays produce a similar signature; however, in this case the jet has a higher track multi-
 1583 plicity in the ID. It is possible to address both cases simultaneously by rejecting the jet when the ID

1584 track multiplicity is less than three—and otherwise rejecting the muon—for jets and muons within
 1585 $\Delta R(\mu, j) < 0.4$.

1586 In addition to the case above where muon bremsstrahlung results in a nearby reconstructed jet,
 1587 the ID track from the muon and the calorimeter energy deposit can lead to it being reconstructed
 1588 as an electron. In this case, if both a muon and an electron share a track in the ID, the muon is
 1589 kept and the electron is rejected, unless the muon is calorimeter-tagged¹⁵, in which case the muon
 1590 is removed in favor of the electron.

Overlap	Check	Result (remove → keep)
Electron & Jet	$\Delta R(e, j) < 0.2$	Jet → Electron
	$0.2 < \Delta R(e, j) < 0.4$	Electron → Jet
Muon & Jet	$\Delta R(\mu, j) < 0.4$ and Jet N_{ID} tracks < 3	Jet → Muon
	$\Delta R(\mu, j) < 0.4$ and Jet N_{ID} tracks ≥ 3	Muon → Jet
Electron & Muon	Shared ID track	Electron → Muon
	Shared ID track & muon is calo-tagged	Muon → Electron

Table 5.6: Summary of the overlap removal procedure used in the analysis. If the criteria in the “check” column is met, in the “result” column, the object on the left of the arrow is removed in favor of the object on the right.

1591 5.2.2 Signal event selection

1592 After the objects have been selected, cuts are applied on a per-event level to select $W^\pm W^\pm jj$ signal
 1593 events. The event selection is summarized in Table 5.8.

1594 The initial event selection chooses events that pass one or more of the trigger requirements listed
 1595 in Table 5.7. At least one signal lepton is “matched” to a passed trigger in order to ensure that
 1596 it was indeed a signal lepton that fired the trigger. A collection of *event cleaning* cuts must also
 1597 be passed in order to remove events collected during periods in which one or more components of
 1598 the detector was not operating optimally. Finally, the events are required to contain at least one
 1599 interaction vertex. An event can have multiple reconstructed vertices from additional proton-proton
 1600 collisions that occurred in the same bunch crossing. In this case, the *primary vertex* is determined
 1601 by choosing the vertex with the largest sum of the p_T^2 of its associated tracks.

1602 Events are then required to contain exactly two signal leptons with the same electric charge.
 1603 The dilepton pair must have a combined invariant mass of $m_{ll} \geq 20$ GeV in order to suppress low
 1604 mass Drell-Yan backgrounds. Two additional selections are applied to events in the ee-channel:

¹⁵A calorimeter-tagged (CT) muon is a muon that is identified by matching an ID track to a calorimeter energy deposit. CT muons have relatively low reconstruction efficiency compared to those measured by the MS, but can be used to recover acceptance in regions of the detector where the MS does not have full coverage [91].

	2015 data	2016 data
Electrons	$p_T > 24$ GeV and Medium ID	$p_T > 26$ GeV and Tight ID and Loose isolation
	$p_T > 60$ GeV and Medium ID	$p_T > 60$ GeV and Medium ID
	$p_T > 120$ GeV and Loose ID	$p_T > 140$ GeV and Loose ID
Muons	$p_T > 20$ GeV and Loose isolation $p_T > 50$ GeV	$p_T > 26$ GeV and Medium isolation $p_T > 50$ GeV

Table 5.7: Summary of trigger requirements for electrons and muons for $\sqrt{s} = 13$ TeV data collected in 2015 and 2016. At least one of the triggers must be satisfied.

1605 both electrons are required to have $|\eta| < 1.37$ with an invariant mass at least 15 GeV away from
 1606 the Z -boson mass to reduce events where one electron is reconstructed with the wrong charge (this
 1607 background will be discussed in more detail in Section 5.3.3). To suppress backgrounds from final
 1608 states with more than two leptons, such as WZ or ZZ , events with more than two leptons passing
 1609 the preselection are vetoed.

1610 Missing transverse energy (E_T^{miss}) represents any particles that escape the detector without being
 1611 measured, such as neutrinos, and it is defined as the magnitude of the vector sum of transverse
 1612 momenta of all reconstructed objects. It can be difficult to calculate accurately, as it involves
 1613 measurements from all subsystems within the detector, and it is sensitive to any corrections that
 1614 may be applied to the reconstructed physics objects [98]. These corrections, including the momentum
 1615 smearing for muons, energy scale and smearing for electrons, and jet calibrations, are propagated
 1616 to the E_T^{miss} calculation. Events are required to contain $E_T^{\text{miss}} > 30$ GeV in order to account for the
 1617 two neutrinos from the W boson decays.

1618 At least two jets are required. The leading and subleading jets must have $p_T > 65$ GeV and
 1619 $p_T > 35$ GeV, respectively, and are referred to as the *tagging jets*. Events are vetoed if they contain
 1620 one or more jets that have been tagged as a b -jet to suppress backgrounds from heavy flavor decays
 1621 (especially top quark events). The b -tagging algorithm used by ATLAS is a boosted decision tree
 1622 (BDT) called MV2c10, and this analysis uses a working point with 85% efficiency [99].

1623 Finally, cuts are applied on the VBS signature outlined in Section 5.0.2. The tagging jets are
 1624 required to have a dijet invariant mass $m_{jj} > 200$ GeV and be separated in rapidity by $|\Delta y_{jj}| > 2.0$.
 1625 This preferentially selects the VBS EWK events over the QCD-produced $W^\pm W^\pm jj$ events.

1626 5.3 Background estimations

1627 The major sources of background events are summarized in Section 5.0.3, and the methods used to
 1628 estimate them are detailed in this section. Prompt backgrounds from ZZ and $t\bar{t} + V$ are estimated

Event selection	
Event preselection	Pass at least one trigger with a matched lepton Pass event cleaning At least one reconstructed vertex
Lepton selection	Exactly two leptons passing signal selection Both signal leptons with the same electric charge Dilepton mass $m_{ll} > 20$ GeV $ \eta < 1.37$ and $ M_{ee} - M_Z > 15$ GeV (ee-channel only) Veto events with more than two preselected leptons
Missing transverse energy	$E_T^{\text{miss}} \geq 30$ GeV
Jet selection	At least two jets Leading jet $p_T > 65$ GeV Subleading jet $p_T > 35$ GeV $m_{jj} > 200$ GeV $N_{b\text{-jet}} = 0$ $ \Delta y_{jj} > 2.0$

Table 5.8: The signal event selection.

1629 directly from MC simulations. The shape of the WZ and $V\gamma$ backgrounds are taken from MC, and
 1630 the predicted yeilds are normalized to the data predictions in dedicated control regions, as outlined
 1631 in Sections 5.3.1 and 5.3.2, respectively. Opposite sign events with a charge misidentified electron
 1632 are estimated by a data-driven background method which is summarized in Section 5.3.3. Finally, a
 1633 *fake-factor* method is used to estimate the contributions from non-prompt backgrounds and is the
 1634 subject of Section 5.3.4.

1635 5.3.1 Estimation of the WZ background

1636 The dominant background involving prompt leptons comes from $WZ + \text{jets}$ events. The contribution
 1637 is estimated from MC simulation and normalized to data in a control region enriched in WZ events.
 1638 This region is defined by the same event selection as the signal region in Table 5.8, with the following
 1639 changes applied to increase the purity of the WZ process:

- 1640 • The third lepton veto is inverted, requiring a third lepton with $p_T > 15$ GeV
- 1641 • Two of the leptons must make a same-flavor opposite-sign pair. If more than one pair exists,
 1642 the one with m_{ll} closest to the Z boson mass is chosen.
- 1643 • The trilepton invariant mass is required to be $m_{lll} > 106$ GeV to reduce contributions from
 1644 $Z\gamma$ and $Z + \text{jets}$

Once the event yields in the control region are calculated, they are propagated to the final signal region fit, detailed in Section 5.4.1, in a single bin combining all the lepton channels. The systematic uncertainties of the WZ background are also calculated at this time. The event yields for the WZ control region are listed in Table 5.9, and distributions of the leading lepton p_T and η as well as trilepton invariant mass m_{lll} are found in Figures 5.9 and 5.8, respectively.

Event yields in the WZ control region	
WZ	197.9 ± 1.4
ZZ	14.1 ± 0.3
Triboson	1.26 ± 0.1
top	10.8 ± 1.1
$Z\gamma$	3.1 ± 1.1
$Z+jets$	2.5 ± 1.4
Total prediction	229.7 ± 2.5
Data	201 ± 14.2

Table 5.9: Event yields in the WZ control region before normalization. All lepton flavor channels are combined.

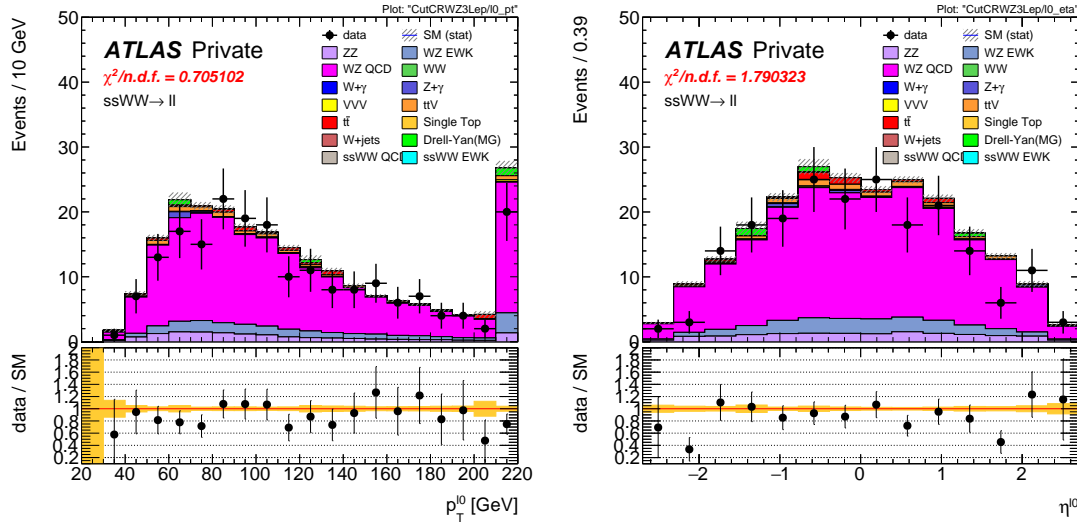


Figure 5.8: Leading lepton p_T (left) and η (right) distributions in the WZ control region before normalization. All lepton channels are combined.

5.3.2 Estimation of the $V\gamma$ background

Events from $V\gamma$ processes can pass selection if the photon converts into an e^+e^- pair and one of the electrons passes the selection criteria. The background is estimated from MC simulations which are

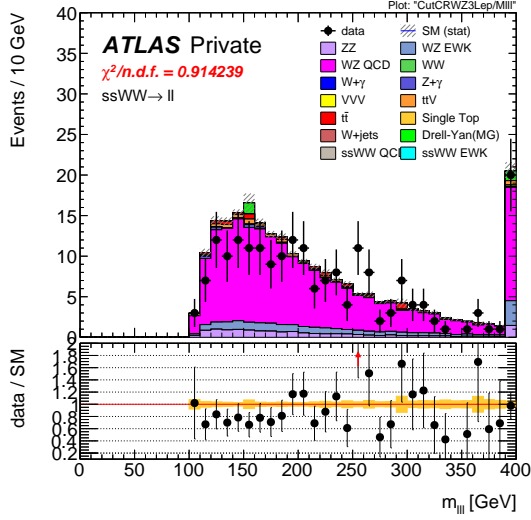


Figure 5.9: Trilepton invariant mass m_{lll} distribution in the WZ control region before normalization. All lepton channels are combined.

1653 then scaled by a normalization factor calculated from a control region enriched in $Z(\mu^+\mu^-)\gamma$ events.
 1654 This control region selects two opposite-sign muons and an additional electron that is assumed to
 1655 come from the photon conversion. The full event selection is detailed in Table 5.10.

$V\gamma$ control region
Exactly two muons with $p_T > 27$ GeV and $p_T > 20$ GeV
Exactly one additional electron with $p_T > 15$ GeV
Remove overlap between $Z+jets$ and $Z\gamma$
Di-muon + photon invariant mass $75 < M_{\mu\mu\gamma} < 100$ GeV
$E_T^{\text{miss}} < 30$ GeV

Table 5.10: Selection criteria for the $V\gamma$ control region.

1656 The $Z\gamma$ MC samples available do not cover the full range of p_T^γ and $\Delta R(\gamma, l)$; thus, additional
 1657 Drell-Yan samples ($Z+jets$) are used to fill out the phase space. Overlap between the two samples
 1658 are removed based to avoid double counting. Events with final state photons are checked at truth
 1659 level¹⁶ to ensure that the photon did not originate from a hadronic decay. Cuts on $p_T^\gamma > 10$ GeV and
 1660 $\Delta R(\gamma, l) > 0.1$ are then applied at generator level, and $Z\gamma$ events that fail this additional selection
 1661 and $Z+jets$ events that pass it are removed.

1662 The normalization factor is calculated directly from the event yields in the $V\gamma$ control region

¹⁶Truth particles are the particles produced directly by the MC generator before being passed through the full detector simulation, at which point they are considered *reconstruction-level* (or *reco-level*) particles.

rather than in the signal fit, as is done for the WZ background. The event yields are listed in Table 5.11, and the normalization factor is determined to be 1.77. No MC events from $Z\gamma$ processes survive the full event selection; thus, the scaling is only applied to the $W\gamma$ background in the signal region. A systematic uncertainty of 44% is assigned to the background based off of the uncertainties in the calculation of the normalization factor.

Event yields in the $V\gamma$ control region	
$Z\gamma$	24.6 ± 3.3
$Z+jets$	3.0 ± 1.5
diboson + triboson	6.7 ± 0.3
top	1.5 ± 0.5
Total prediction	35.8 ± 3.7
Data	57 ± 7.6

Table 5.11: Event yields in the $V\gamma$ control region. The $V\gamma$ scale factor of 1.77 is calculated by scaling up the $Z\gamma$ and $Z+jets$ backgrounds to account for the difference between the data and predicted total background.

5.3.3 Estimation of backgrounds from charge misidentification

If an electron's charge is mis-reconstructed, it can lead to a real opposite-sign lepton pair passing the same-sign requirement in the event selection. There are two primary reasons this can occur:

1. An electron emits a photon via bremsstrahlung which then converts into an electron-positron pair, and the conversion track with the wrong electric charge is matched to the original electron. This is the dominant process leading to charge flip, and it is highly dependent on the electron η due to the different amount of detector material the electron passes through.
2. The curvature of the electron's track is mis-measured, resulting in the wrong charge being assigned. This process is dependent on the momentum of the electron, as its track becomes more straight as the momentum of the electron increases.

In order to estimate this background, the rate at which an electron's charge is misidentified is calculated from $Z \rightarrow e^+e^-$ MC simulation. It is known that the MC does not perfectly model the material effects leading to charge flip; as a result, scale factors are applied to the MC in order for it to better reflect the real performance. These scale factors are obtained from the ratio of charge mis-ID rates in data and uncorrected MC in [70] following the method outlined in [100]. Once the scale factors are applied, the charge misidentification rate ε can be extracted by comparing the

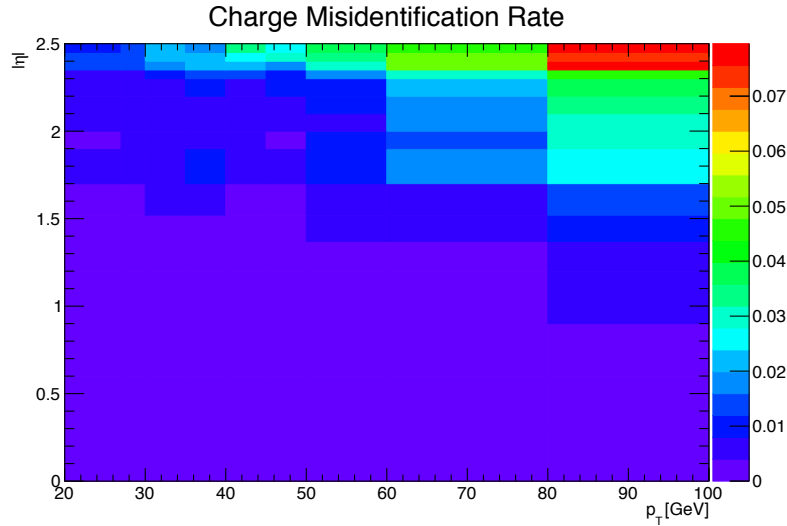


Figure 5.10: Charge misidentification rates for electrons as a function of $|\eta|$ and p_{T} . Rates are calculated from $Z \rightarrow e^+e^-$ MC after applying scale factors to approximate the charge mis-ID rates in data.

1684 electron's reconstructed charge with the charge of its truth particle:

$$\varepsilon(\eta, p_{\text{T}}) = \frac{N_{\text{wrong charge}}}{N_{\text{prompt electrons}}} \quad (5.1)$$

1685 The charge mis-ID rate is calculated in bins of electron $|\eta|$ and p_{T} , and it varies from below 0.1%
 1686 in the central region of the detector up to 8% in the forward regions for high p_{T} (above 90 GeV)
 1687 electrons. A two-dimensional plot of ε can be found in Figure 5.10.

1688 Given the charge flip rate $\varepsilon(\eta, p_{\text{T}})$, the rate at which an electron has its charge correctly recon-
 1689 structed is $(1 - \varepsilon)$. Thus there are three possible combinations of charge identification, assuming a
 1690 two-electron event:

- 1691 1. Both electrons are reconstructed correctly: $(1 - \varepsilon)^2$
- 1692 2. Both electrons are mis-reconstructed: ε^2
- 1693 3. Only one electron is mis-reconstructed: $2\varepsilon(1 - \varepsilon)$

1694 In order to estimate the size of the background from charge misidentification, opposite-sign events
 1695 are selected using the default event selection for a given signal or control region with the same-sign
 1696 requirement inverted. These events are then weighted by the probability for one of the electrons to

1697 be reconstructed with the wrong charge:

$$\omega = \frac{\varepsilon_1(1 - \varepsilon_2) + \varepsilon_2(1 - \varepsilon_1)}{(1 - \varepsilon_1)(1 - \varepsilon_2) + \varepsilon_1\varepsilon_2} \quad (5.2)$$

1698 where the subscripts 1 and 2 refer to the leading and subleading electrons, respectively, and ε_i is a
 1699 function of the η and p_T of the i^{th} electron. In the case of an event with only one electron and one
 1700 muon, Equation 5.2 simplifies:

$$\omega = \frac{\varepsilon}{1 - \varepsilon} \quad (5.3)$$

1701 This method assumes that there is little contamination from fake electrons in the opposite-sign
 1702 sample, and this has been verified with MC simulation.

1703 Additionally, charge-flipped electrons tend to be reconstructed with lower energy when compared
 1704 to electrons with the correct charge. This is due to energy loss from the material interactions that
 1705 can cause the charge to be misidentified in the first place. A correction factor is calculated from
 1706 MC simulations, comparing the p_T of the truth electron to its reconstructed counterpart:

$$\alpha = \frac{\left(\frac{p_T^{\text{reco}}}{p_T^{\text{truth}}} - 1\right)_{\text{correct charge}}}{\left(\frac{p_T^{\text{reco}}}{p_T^{\text{truth}}} - 1\right)_{\text{wrong charge}}} \quad (5.4)$$

1707 The correction is then applied to the p_T of the charge-flipped electron via

$$p_T = p_T^0 / (1 + \alpha) + dE \quad (5.5)$$

1708 where p_T^0 is the uncorrected p_T of the electron and dE is a gaussian smearing factor centered at zero
 1709 with a width related to the energy resolution. Since which electron is mis-reconstructed is never
 1710 determined in this method, in the case of a two-electron event, the energy correction is applied
 1711 randomly to one of the two electrons based on the probabilities for them to be charge-flipped. This
 1712 also determines the overall sign of the event; the charge of the electron that does not receive the
 1713 correction is taken to be the charge for both.

1714 Systematic uncertainties on the charge mis-ID rates are calculated by generating two additional
 1715 sets of rates with the uncertainties on the scale factors varied up and down. The size of the esti-
 1716 mated charge flip background without the energy correction applied is also taken as a systematic
 1717 uncertainty. These systematic uncertainties are estimated to be approximately $\pm 15\%$.

1718 5.3.3.1 Validation of the charge misidentification estimate

1719 The performance of the charge misidentification estimation is tested in the same-sign inclusive
 1720 validation region (VR), defined in Table 5.12. For ee events, the mass of the dilepton pair is required

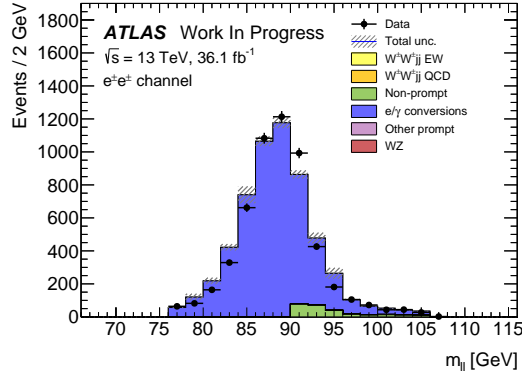


Figure 5.11: Dilepton invariant mass distribution m_{ll} for the ee channel in the same-sign inclusive VR.

1721 to lie within 15 GeV of the Z boson mass to increase the purity of the charge flip background.
 1722 $t\bar{t}$ production, which can contribute to both the charge mis-ID and fake lepton backgrounds, is
 1723 suppressed by the b -jet veto. The di-electron invariant mass is shown in Figure 5.11, and distributions
 1724 of the leading and subleading electron p_T in the ee -channel are shown in Figure 5.12 with the Z
 1725 mass cut inverted. Agreement between data and prediction is seen within the total statistical and
 1726 systematic uncertainties in the VR.

Same-sign inclusive VR
Exactly 2 same-sign signal leptons
$p_T > 27 \text{ GeV}$ for both leptons
$m_{ll} > 20 \text{ GeV}$
$ m_{ee} - m_Z > 15 \text{ GeV}$ ($e^\pm e^\pm$ -channel only)
$N_{b\text{-jet}} = 0$

Table 5.12: Selection criteria for the same-sign inclusive validation region.

1727 5.3.4 Estimation of non-prompt backgrounds with the fake-factor method

1728 Events with one prompt lepton produced in association with hadronic jets can pass the event selection
 1729 if a jet is misidentified as a charged lepton or if a non-prompt lepton from the decay of a heavy
 1730 flavor particle (such as b - and c -hadrons) passes the signal lepton criteria. These misidentified jets
 1731 and non-prompt leptons are collectively referred to as *fake leptons*, or simply *fakes*. The rate at
 1732 which a fake lepton is misidentified is generally not modelled well enough by the MC to accurately
 1733 estimate their contributions directly from simulation. Therefore, a data-driven technique called the

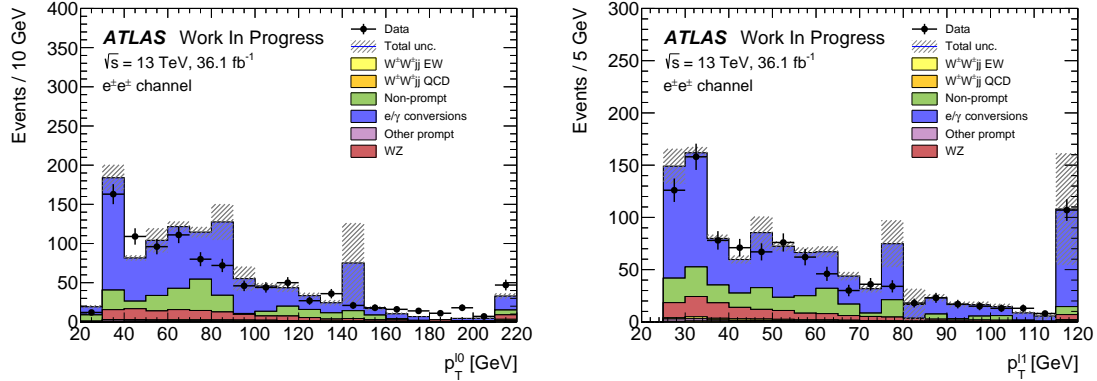


Figure 5.12: p_T distributions for the leading (left) and subleading (right) electron for the ee channel in the same-sign inclusive VR. In these plots, the cut requiring m_{ee} to fall within the Z mass window has been inverted in order to test the modelling away from the Z peak.

1734 *fake-factor* is used to estimate the size and shape of background processes from fake leptons. In
 1735 this analysis, a new modification to the fake-factor is used involving the particle isolation variables;
 1736 the method is outlined in the context of the *default* fake-factor in Section 5.3.4.1, and the modified
 1737 fake-factor is outlined in Section 5.3.4.2.

1738 5.3.4.1 Overview of the default fake-factor method

1739 The goal of the fake-factor method is to measure the fake rate from real collision events in a region
 1740 enriched in fake leptons and use it to estimate the size of the fake lepton background in a chosen
 1741 signal or control region. This is done by creating two samples using different lepton definitions:

- 1742 1. The *nominal* sample is made up of leptons passing the signal selection.
 1743 2. The *loose* sample is made up of leptons that fail the signal selection while still passing a
 1744 loosened set of criteria. This sample is enriched in fake leptons and is orthogonal to the set of
 1745 signal leptons.

1746 Using the sets of nominal and loose leptons, a fake-factor f can be calculated in a region enriched
 1747 in processes that are prone to producing fake leptons:

$$f = \frac{N_{\text{nominal}}}{N_{\text{loose}}} \quad (5.6)$$

1748 Since the fake rate is not expected to be constant over the entire phase space, the fake-factor can
 1749 be divided into bins:

$$f(b) = \frac{N_{\text{nominal}}(b)}{N_{\text{loose}}(b)} \quad (5.7)$$

1750 where b represents the bin number. In this analysis, the fake-factor is binned in lepton p_T .

1751 In order to estimate the fake background contribution in a given signal or control region, the
 1752 fake-factor is applied to a second control region with a selection identical to the region of interest
 1753 except one of the leptons required to satisfy the loose criteria. The region for which the background
 1754 is estimated contains two nominal leptons and is referred to as *nominal+nominal* (*NN*), and the
 1755 associated control region where the fake-factor is applied contains one nominal and one loose lepton
 1756 and is referred to as *nominal+loose* (*NL*). The fake background in a *NN* region can then be
 1757 calculated as:

$$N_{NN}^{\text{fake bkg.}} = \sum_b f(b) N_{NL}(b) \quad (5.8)$$

1758 Backgrounds containing two prompt leptons can also enter the *NL* region if one of the leptons
 1759 passes the nominal selection and the other passes the loose selection. Since the fake-factor method
 1760 estimates the fake background by scaling the amount of non-prompt events in the *NL* region, if these
 1761 prompt contributions are not removed, they will be included in the scaling and the background
 1762 will be overpredicted. The final estimate of the fake background becomes:

$$N_{NN}^{\text{fake bkg.}} = \sum_b f(b) (N_{NL}(b) - N_{NL}^{\text{prompt}}(b)) \quad (5.9)$$

1763 A visual representation of the fake background estimation process is shown in Figure 5.13.

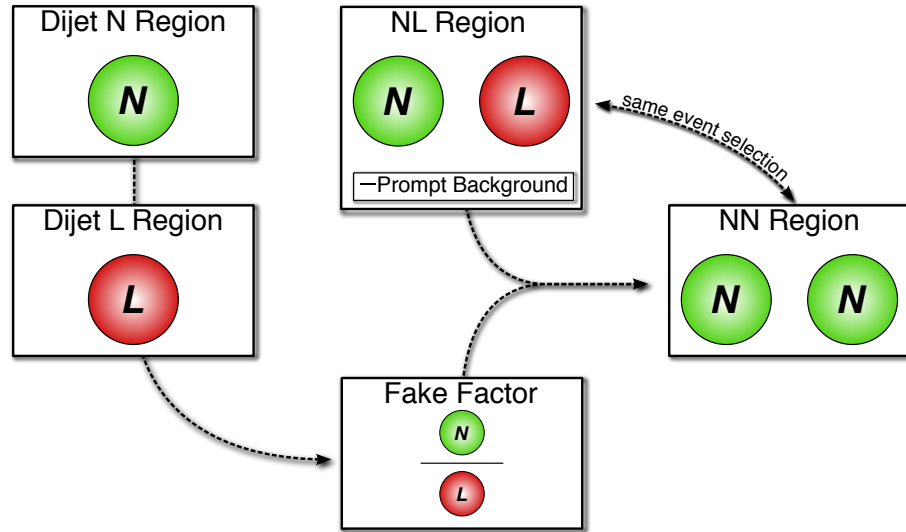


Figure 5.13: Graphical representation of how the fake factor method is used to estimate the fake background in a given *NN* region.

1764 **5.3.4.2 The fake-factor with p_T^{cone}**

1765 When a jet produces a non-prompt lepton, that lepton only carries a fraction of the underlying jet's
 1766 total momentum. Due to the isolation cut applied to the nominal leptons, they typically carry a
 1767 much larger percentage of the underlying jet momentum than the loose leptons. Since the isolation
 1768 essentially sets a limit on the amount of detector activity allowed around the lepton, if other nearby
 1769 particles carried a significant amount of momentum, the lepton would likely fail this cut.

1770 This discrepancy in the underlying jet momentum fraction can cause problems in the calculation
 1771 of the fake-factor f . Consider the case where two separate events have jets of identical momentum,
 1772 but one produces a non-prompt lepton that passes the nominal selection, and the other produces a
 1773 non-prompt lepton that passes the loose selection. The loose lepton on average will have lower p_T
 1774 than the nominal lepton despite both originating from jets with the same momentum. This can be
 1775 seen explicitly when comparing the p_T of a muon to its associated truth jet:

$$\Delta p_T(\mu, j) = \frac{p_T(j) - p_T(\mu)}{p_T(j) + p_T(\mu)} \quad (5.10)$$

1776 Since muons are not included in the jet reconstruction algorithm, Δp_T approximates the momentum
 1777 of the muon compared to the rest of the jet. For muons that carry more than 50% of the jet's
 1778 momentum, Δp_T will be negative and vice-versa. The Δp_T distributions for nominal and loose
 1779 muons in $t\bar{t}$ MC events is shown Figure 5.14, where a 50 GeV jet on average corresponds to a
 1780 35 GeV nominal muon and a 20 GeV loose muon¹⁷.

1781 Since the default fake-factor defined in Equation 5.7 is binned in lepton p_T , within a given bin,
 1782 the underlying jet p_T spectrum can differ substantially between the numerator and the denominator.
 1783 Additionally, these differences can vary depending on the process producing the non-prompt leptons
 1784 or on the specific kinematic selections of the signal or control regions where the fake-factor is applied.

1785 Fortunately, the majority of the jet momentum not carried by the non-prompt lepton (excluding
 1786 neutrinos) can be recovered using isolation variables. A track-based isolation is chosen, referred to
 1787 as p_T^{cone} , and it contains the sum of the p_T of all particle tracks originating from the primary vertex
 1788 within a cone of $\Delta R < 0.3$ around the lepton. Thus, the sample of loose leptons in the denominator
 1789 of the fake-factor calculation is binned in $p_T + p_T^{\text{cone}}$ rather than simply lepton p_T . Adding the
 1790 isolation cone greatly reduces the difference in the fraction of the underlying jet momentum carried
 1791 by the nominal and loose leptons. To check this, a new Δp_T is calculated between a lepton and its

¹⁷To better illustrate the point, here the muon is added back into the jet p_T , and the corresponding muon p_T is obtained via $\Delta p_T(\mu, j) = \frac{(p_T(j) - p_T\mu) - p_T(\mu)}{(p_T(j) - p_T\mu) + p_T(\mu)} = \frac{p_T(j) - 2p_T(\mu)}{p_T(j)}$.

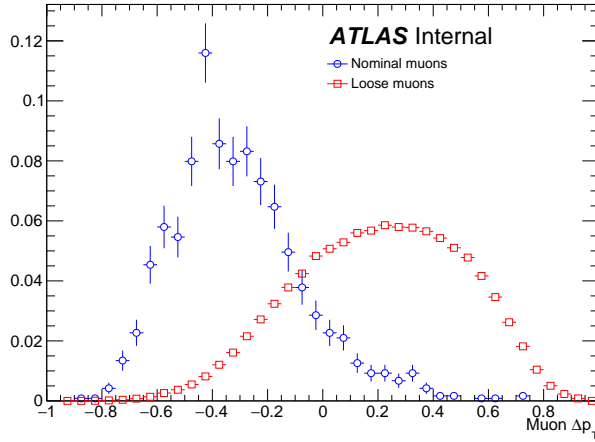


Figure 5.14: Δp_{T} distributions for nominal (blue) and loose (red) muons in simulated $t\bar{t}$ events. Each muon has been matched to a truth-level jet. Both distributions are normalized to unit area.

1792 matched truth jet, where the truth jet p_{T} has been corrected to include all muons within a cone of
 1793 $\Delta R < 0.4$:

$$p_{\mathrm{T}}(j) = p_{\mathrm{T}}(j_{\mathrm{truth}}) + \sum_{\Delta R < 0.4} p_{\mathrm{T}}(\mu_{\mathrm{truth}}) \quad (5.11)$$

1794 The Δp_{T} distributions comparing p_{T} and $p_{\mathrm{T}} + p_{\mathrm{T}}^{\mathrm{cone}}$ for nominal and loose leptons using the corrected
 1795 jet p_{T} are found in Figure 5.15, and better agreement is seen between the numerator (nominal) and
 1796 denominator (loose with $p_{\mathrm{T}} + p_{\mathrm{T}}^{\mathrm{cone}}$) distributions.

1797 The numerator remains binned in lepton p_{T} , due to the fact that it is meant to mirror the signal
 1798 region as closely as possible, and the signal lepton selection does not use $p_{\mathrm{T}} + p_{\mathrm{T}}^{\mathrm{cone}}$. The impact of
 1799 this is expected to be negligible due to the $p_{\mathrm{T}}^{\mathrm{cone}}$ isolation being small for signal leptons, as shown
 1800 for muons in Figure 5.16. Finally, the fake-factor f becomes:

$$f(b) = \frac{N_{\mathrm{nominal}}(b(p_{\mathrm{T}}))}{N_{\mathrm{loose}}(b(p_{\mathrm{T}} + p_{\mathrm{T}}^{\mathrm{cone}}))} \quad (5.12)$$

1801 5.3.4.3 Application of the fake-factor

1802 The fake-factor itself is measured from a sample data events passing a dijet selection requiring
 1803 exactly one lepton (either passing the nominal or loose selections) and at least one jet. The leading
 1804 jet must also be b -tagged and approximately back-to-back with the lepton in order to enhance non-
 1805 prompt lepton contributions while reducing contributions from processes involving W and Z bosons.

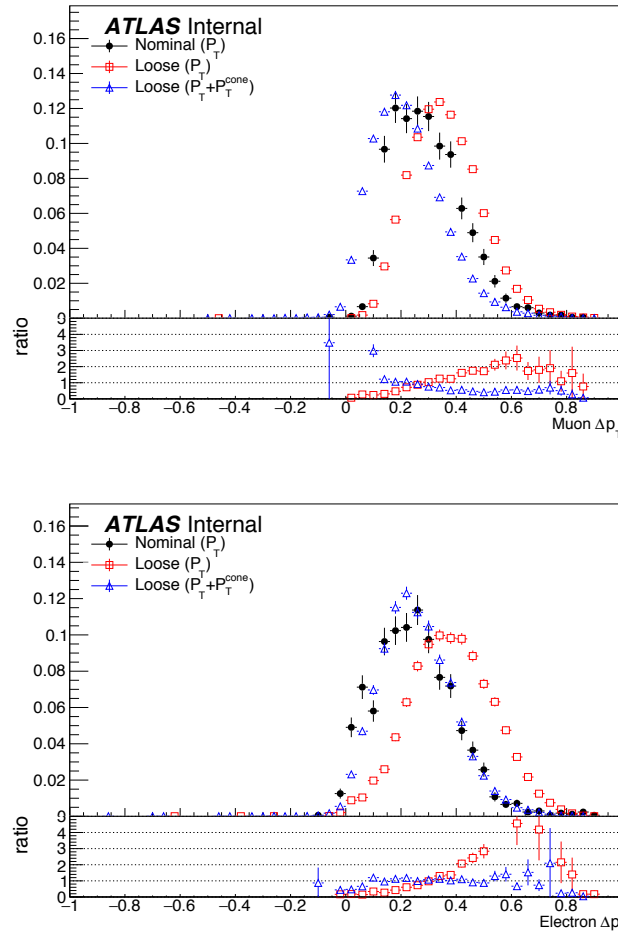


Figure 5.15: Δp_T distributions for muons (top) and electrons (bottom) in simulated $t\bar{t}$ events. Each lepton has been matched to a truth-level jet, and that truth jet has had its p_T corrected to include all truth muons within a cone of $\Delta R < 0.4$. The nominal leptons are in black. Δp_T is calculated for the loose leptons using p_T (red) and $p_T + p_T^{\text{cone}}$ (blue).

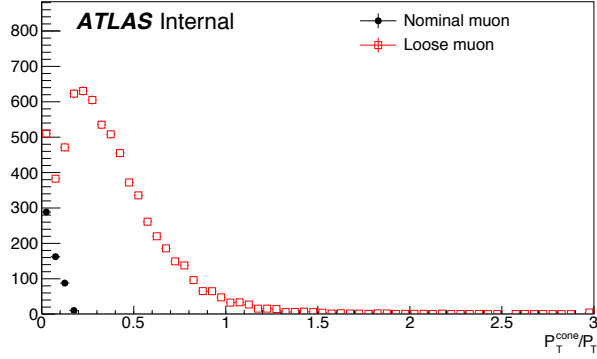


Figure 5.16: Distributions of p_T^{cone}/p_T for nominal (black) and loose (red) muons in simulated $t\bar{t}$ events.

1806 W boson events are further suppressed by requiring the sum of the E_T^{miss} and the transverse mass
 1807 of the lepton to be less than 50 GeV. The full event selection for the dijet region is summarized in
 1808 Table 5.13.

Dijet event selection	
Event preselection	
Exactly one lepton with $p_T > 15$ GeV	
$N_{\text{jet}} > 0$	
Leading jet is b -tagged	
$p_T^{\text{lead. jet}} > 25$ GeV	
$p_T^{\text{lead. jet}} > 30$ GeV if $ \eta_j > 2.5$	
$ \Delta\phi(l, \text{lead. jet}) > 2.8$	
$m_T(l, E_T^{\text{miss}}) + E_T^{\text{miss}} < 50$ GeV	

Table 5.13: Event selection for the dijet region used for calculating the fake-factor. The selected lepton can pass either the nominal (signal) or loose selections. In the case of the nominal leptons, the $p_T > 27$ GeV requirement is replaced with $p_T > 15$ GeV.

1809 The numerator sample is constructed from dijet events in which the lepton passes the nominal
 1810 (signal) selection and is binned in the lepton p_T . Similarly, the denominator sample is made up of
 1811 the remaining dijet events where the lepton passes the loose selection and is binned in the lepton
 1812 $p_T + p_T^{\text{cone}}$. The nominal and loose leptons pass the signal selection¹⁸ and loose selection, respectively,
 1813 defined earlier in Table 5.3 for muons and Table 5.4 for electrons. Backgrounds from W +jets,
 1814 Z +jets, $t\bar{t}$, and single top processes are estimated from MC simulations requiring one lepton to be
 1815 prompt using the truth information; these contributions are subtracted from the dijet data. The

¹⁸The $p_T > 27$ GeV cut in the signal lepton selection is dropped in favor of the $p_T > 15$ GeV requirement in the dijet selection.

fake-factor is then calculated using Equation 5.12 for muons and for central and forward electrons separately. The muon fake-factor is shown in Figure 5.17, and the two electron fake-factors are shown in Figure 5.18. The numerical values of the fake-factors, including their systematic uncertainties which will be discussed in Section 5.3.4.4, are listed in Table 5.14.

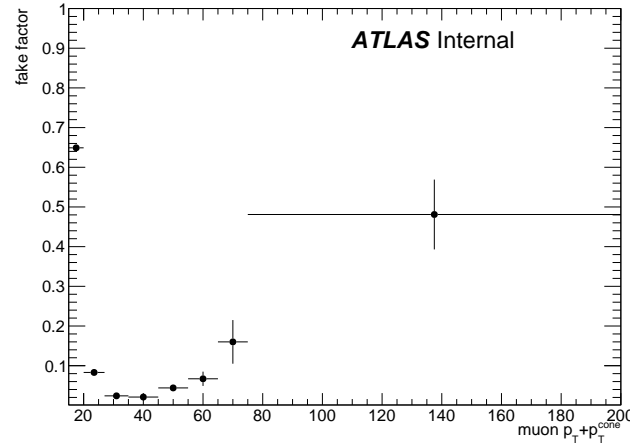


Figure 5.17: The measured fake-factor as a function of muon $p_T + p_T^{\text{cone}}$. The error bars represent the statistical uncertainty only.

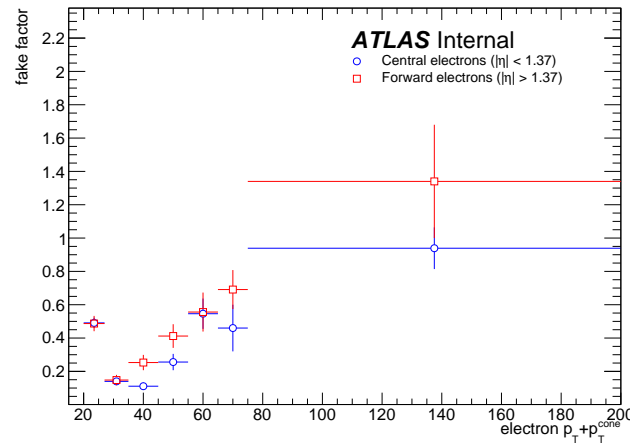


Figure 5.18: The measured fake-factor as a function of electron $p_T + p_T^{\text{cone}}$ in the central ($|\eta| < 1.37$, blue) and forward ($|\eta| > 1.37$, red) regions of the detector. The error bars represent the statistical uncertainty only.

In order to properly account for the denominator being binned in $p_T + p_T^{\text{cone}}$, special care needs

1821 to be taken when estimating the fake background from the *NL* regions. For the purposes of the
 1822 fake-factor calculation, it is perhaps more intuitive to consider a loose *object* with $p_T = p_T + p_T^{\text{cone}}$
 1823 instead of simply a loose *lepton*, as the lepton and the underlying jet are treated as a whole with this
 1824 method. When the lepton p_T cuts required by a particular signal or control region are applied to
 1825 nominal and loose leptons, the cut is applied to the p_T of the nominal lepton and to the $p_T + p_T^{\text{cone}}$
 1826 of the loose object. Similarly, when looking up the fake-factor weight for a given *NL* event, the
 1827 value taken from the bin corresponding to the $p_T + p_T^{\text{cone}}$ of the loose object. Finally, when applying
 1828 the weight to the event, $p_T + p_T^{\text{cone}}$ is assigned as the p_T of the loose object. Figure 5.19 contains a
 1829 graphical representation of this procedure.

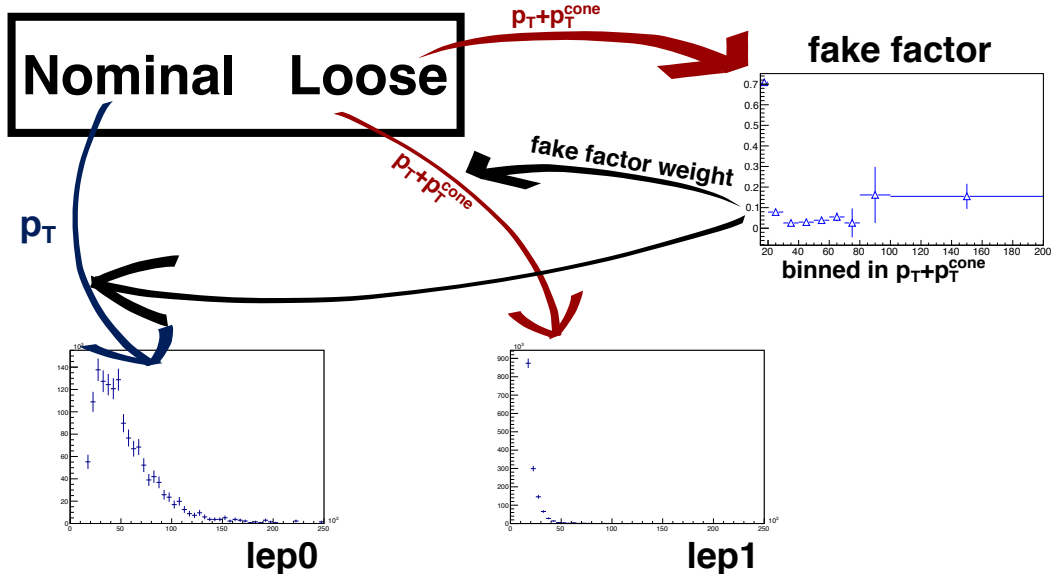


Figure 5.19: Graphical representation of the fake-factor application using $p_T + p_T^{\text{cone}}$. The value of $p_T + p_T^{\text{cone}}$ for the loose lepton is used to “look up” the fake-factor weight which is then applied to the event. The loose lepton’s p_T becomes $p_T + p_T^{\text{cone}}$ for the purpose of the fake background estimation.
 TODO: Update figure to match style of Fig. 5.13.

1830 Finally, it should be noted that the addition of p_T^{cone} to the loose object may cause the loose
 1831 leptons in the denominator sample to migrate into higher bins. This results in an overall decrease in
 1832 the number of loose objects in the lower $p_T + p_T^{\text{cone}}$ bins due to there not being additional leptons at
 1833 lower p_T to replace them. Since the fake-factor is a ratio of the number of events in a bin, this effect
 1834 causes the first few bins of the fake-factor to increase, as can be seen clearly in Figure 5.17. However,
 1835 the signal and control regions (and their corresponding *NL* regions) contain a $p_T > 27$ GeV cut that
 1836 prevents these migrations from negatively impacting the fake estimation.

1837 **5.3.4.4 Systematic uncertainties**

1838 Four sources of systematic uncertainty are considered: the dijet event selection, the prompt back-
1839 ground subtraction, the jet flavor composition, and residual dependence on the underlying jet p_T
1840 spectrum. In order to measure the impact of these systematics, new fake-factors are computed
1841 with each of the systematic variations and the differences from the nominal values are taken as the
1842 uncertainty.

- 1843 1. In order to estimate uncertainties due to the dijet selection, the cut on $M_T + E_T^{\text{miss}}$ is varied
1844 by ± 5 GeV, the jet-lepton separation $\Delta\phi(l, j)$ by ± 0.1 , and the jet p_T cut by $+5$ GeV.

1845 2. To estimate the systematic uncertainty on the prompt background subtraction, the MC pre-
1846 diction in a $W+\text{jets}$ control region is compared to data. The discrepancy between data and
1847 MC is found to be approximately 10% [70]. Therefore, the prompt background used for the
1848 subtraction is scaled up and down by $\pm 10\%$.

1849 3. The difference in the jet flavor composition between the dijet events and the events in the
1850 NL regions can affect the accuracy of the fake background estimation. The dijet sample is
1851 dominated by light jets, while the NL regions tend to be dominated by heavy flavor from $t\bar{t}$.
1852 To account for this, the fake-factor is computed with a b -jet veto.

1853 4. To measure any residual dependence on the underlying jet p_T spectrum, the leading jet p_T
1854 distribution is reweighted to match the p_T spectrum of truth jets that produce fake leptons
1855 in MC simulations. This results in an increase in the number of nominal and loose leptons at
1856 high momentum [70].

1857 **5.3.4.5 Results of the fake-factor**

1858 The fake background contribution in the signal region is estimated by applying the fake-factors
1859 to the equivalent NL region using Equation 5.9, where the fake-factor used corresponds to the
1860 flavor of the loose lepton in the event. As usual, the prompt background is subtracted from the
1861 NL events using MC simulation. Charge misidentification is handled using the same method as
1862 in Section 5.3.3, with an additional set of charge flip rates calculated for loose leptons. The fake
1863 background yields in the signal region are listed in Table 5.15. An overall uncertainty of 50% is
1864 assigned to the fake background estimation in $\mu^\pm\mu^\pm$ events, and between 40% to 90% for $e^\pm e^\pm$ and
1865 $\mu^\pm e^\pm$ events, including both statistical and systematic effects.

fake-factor	$p_T[15, 20]$	$p_T[20, 27]$	$p_T[27, 35]$	$p_T[35, 45]$	$p_T[45, 55]$	$p_T[55, 65]$	$p_T[65, 75]$	$p_T[75, 200]$
nominal	0.649 ± 0.007	0.083 ± 0.002	0.024 ± 0.002	0.021 ± 0.003	0.044 ± 0.007	0.067 ± 0.018	0.160 ± 0.055	0.481 ± 0.088
MT+MET	0.649 ± 0.007	0.082 ± 0.002	0.082 ± 0.002	0.020 ± 0.003	0.045 ± 0.007	0.068 ± 0.018	0.207 ± 0.062	0.523 ± 0.086
$\Delta\phi(\ell, j)$	0.645 ± 0.008	0.083 ± 0.003	0.024 ± 0.002	0.021 ± 0.004	0.045 ± 0.008	0.064 ± 0.021	0.064 ± 0.058	0.438 ± 0.092
Jet p_T	0.650 ± 0.007	0.083 ± 0.002	0.024 ± 0.002	0.021 ± 0.003	0.045 ± 0.007	0.069 ± 0.018	0.159 ± 0.018	0.481 ± 0.088
$N_{b\text{-jet}} = 0$	0.724 ± 0.003	0.094 ± 0.001	0.035 ± 0.001	0.025 ± 0.002	0.022 ± 0.004	0.060 ± 0.015	0.026 ± 0.053	0.044 ± 0.134
Bkg. subtraction	0.648 ± 0.007	0.083 ± 0.002	0.024 ± 0.002	0.019 ± 0.003	0.037 ± 0.007	0.044 ± 0.019	0.096 ± 0.062	0.370 ± 0.082
Jet p_T Reweighting	0.649 ± 0.007	0.083 ± 0.002	0.025 ± 0.002	0.022 ± 0.003	0.050 ± 0.007	0.090 ± 0.017	0.224 ± 0.052	0.591 ± 0.099
	0.539 ± 0.077	0.093 ± 0.007	0.025 ± 0.004	0.043 ± 0.019	0.063 ± 0.014	0.085 ± 0.025	0.141 ± 0.110	1.962 ± 0.492

(a) fake-factor for muons.

fake-factor	$p_T[20, 27]$	$p_T[27, 35]$	$p_T[35, 45]$	$p_T[45, 55]$	$p_T[55, 65]$	$p_T[65, 75]$	$p_T[75, 200]$
nominal	0.491 ± 0.031	0.140 ± 0.020	0.111 ± 0.023	0.256 ± 0.049	0.546 ± 0.091	0.460 ± 0.140	0.939 ± 0.125
MT+MET	0.493 ± 0.030	0.138 ± 0.019	0.115 ± 0.022	0.261 ± 0.045	0.559 ± 0.084	0.656 ± 0.091	0.802 ± 0.016
$\Delta\phi(\ell, j)$	0.488 ± 0.032	0.137 ± 0.020	0.110 ± 0.025	0.283 ± 0.053	0.503 ± 0.097	0.351 ± 0.149	1.117 ± 0.255
Jet p_T	0.489 ± 0.035	0.134 ± 0.021	0.105 ± 0.025	0.224 ± 0.048	0.593 ± 0.093	0.356 ± 0.144	0.928 ± 0.177
$N_{b\text{-jet}} = 0$	0.506 ± 0.029	0.140 ± 0.018	0.111 ± 0.022	0.260 ± 0.046	0.545 ± 0.084	0.546 ± 0.120	0.882 ± 0.103
Jet p_T	0.493 ± 0.032	0.146 ± 0.021	0.115 ± 0.024	0.259 ± 0.049	0.550 ± 0.091	0.460 ± 0.140	0.939 ± 0.125
$N_{b\text{-jet}} = 0$	0.387 ± 0.009	0.130 ± 0.008	0.321 ± 0.012	0.473 ± 0.015	0.716 ± 0.180	0.716 ± 0.180	0.716 ± 0.180
Bkg. subtraction	0.488 ± 0.031	0.138 ± 0.020	0.106 ± 0.023	0.248 ± 0.049	0.529 ± 0.092	0.434 ± 0.143	0.888 ± 0.115
Jet p_T Reweighting	0.493 ± 0.031	0.142 ± 0.020	0.115 ± 0.023	0.264 ± 0.049	0.563 ± 0.090	0.485 ± 0.136	0.989 ± 0.132
	0.445 ± 0.055	0.137 ± 0.037	0.065 ± 0.023	0.115 ± 0.033	0.603 ± 0.047	0.104 ± 0.105	0.299 ± 0.260

(b) fake-factor for central electrons ($|\eta| < 1.37$).

fake-factor	$p_T[20, 27]$	$p_T[27, 35]$	$p_T[35, 45]$	$p_T[45, 55]$	$p_T[55, 65]$	$p_T[65, 75]$	$p_T[75, 200]$
nominal	0.487 ± 0.046	0.148 ± 0.031	0.253 ± 0.046	0.412 ± 0.071	0.556 ± 0.117	0.691 ± 0.117	1.340 ± 0.340
MT+MET	0.483 ± 0.045	0.152 ± 0.031	0.241 ± 0.043	0.443 ± 0.070	0.565 ± 0.106	0.668 ± 0.117	1.075 ± 0.189
$\Delta\phi(\ell, j)$	0.495 ± 0.047	0.156 ± 0.033	0.271 ± 0.052	0.364 ± 0.074	0.664 ± 0.107	0.749 ± 0.056	0.885 ± 0.084
Jet p_T	0.471 ± 0.051	0.158 ± 0.035	0.247 ± 0.051	0.474 ± 0.085	0.283 ± 0.107	0.546 ± 0.149	1.189 ± 0.266
$N_{b\text{-jet}} = 0$	0.478 ± 0.042	0.170 ± 0.031	0.274 ± 0.046	0.389 ± 0.066	0.645 ± 0.104	0.757 ± 0.102	1.319 ± 0.326
Jet p_T	0.523 ± 0.048	0.149 ± 0.033	0.235 ± 0.045	0.429 ± 0.073	0.555 ± 0.117	0.691 ± 0.117	1.340 ± 0.340
$N_{b\text{-jet}} = 0$	0.525 ± 0.011	0.234 ± 0.013	0.644 ± 0.016	0.710 ± 0.014	0.274 ± 0.316	0.274 ± 0.316	0.274 ± 0.316
Bkg. subtraction	0.484 ± 0.046	0.146 ± 0.031	0.248 ± 0.046	0.406 ± 0.071	0.545 ± 0.118	0.676 ± 0.118	1.317 ± 0.337
Jet p_T Reweighting	0.489 ± 0.046	0.151 ± 0.031	0.257 ± 0.046	0.419 ± 0.071	0.568 ± 0.117	0.705 ± 0.115	1.363 ± 0.342
	0.328 ± 0.068	0.124 ± 0.048	0.297 ± 0.100	0.234 ± 0.061	0.680 ± 0.092	0.452 ± 0.138	2.385 ± 1.729

(c) fake-factor for forward electrons ($1.37 < |\eta|$).Table 5.14: Values of the fake-factor in each p_T bin and for each individual systematic source.

	estimated yield	f_e stat. up	f_e stat. dn	f_e syst. up	f_e syst. dn	f_μ stat. up	f_μ stat. dn	f_μ syst. up	f_μ syst. dn
$e^\pm e^\pm$	11.42 ± 3.13	—	—	—	—	—	—	—	—
$\mu^\pm \mu^\pm$	4.82 ± 0.77	—	—	—	—	0.65	-0.65	3.64	-0.61
$\mu^\pm e^\pm$	37.08 ± 5.16	4.90	-4.90	5.59	-14.34	1.39	-1.39	16.10	-1.98

Table 5.15: Estimated yields for the fake lepton background. The estimated yield is shown in the first column together with the statistical uncertainty followed by the systematic uncertainties from variations of the the fake-factors within their statistical (stat.) and systematic (syst.) uncertainties. The labels f_e and f_μ indicate the fake-factors for electrons and muons, respectively.

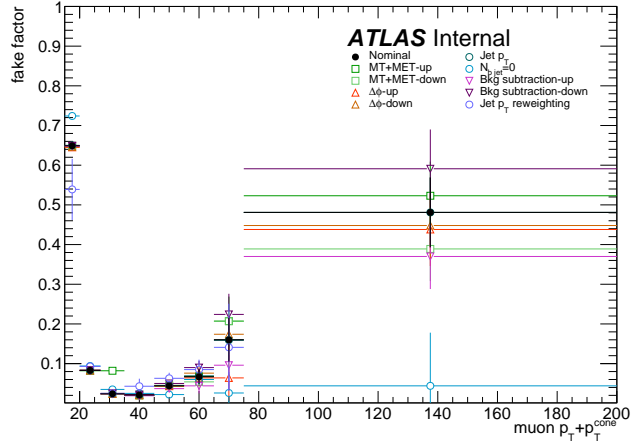


Figure 5.20: Systematic variations in the fake-factor as a function of muon $p_T + p_T^{\text{cone}}$. The individual fake-factors obtained for each systematic variation are displayed with their statistical uncertainties.

1866 5.3.4.6 Validation of the fake-factor

1867 The accuracy of the fake-factor method is tested in several validation regions, the most sensitive
 1868 of which is the same-sign top fakes VR (SS top VR), defined in Table 5.16. This region inverts
 1869 the signal region's b -jet veto to accept events with exactly one b -jet. Due to this requirement, the
 1870 dominant source of events comes from the $t\bar{t}$ process where a b -jet fakes an isolated lepton. The
 1871 distribution of the subleading lepton p_T in this VR is shown in Figure 5.22 for all lepton flavor
 1872 combinations. There is good agreement between the data and the prediction, even when only taking
 1873 into account the statistical uncertainty and not the large systematic uncertainties assigned to the
 1874 fake estimation.

Same-sign top fakes VR
Exactly 2 same-sign signal leptons
$p_T > 27$ GeV for both leptons
$m_{ll} > 20$ GeV
$ m_{ee} - m_Z > 15$ GeV ($e^\pm e^\pm$ -channel only)
$N_{b\text{-jet}} = 1$
$N_{\text{jet}} \geq 2$
Leading jet $p_T > 65$ GeV
Subleading jet $p_T > 35$ GeV

Table 5.16: Selection criteria for the same-sign top fakes validation region.

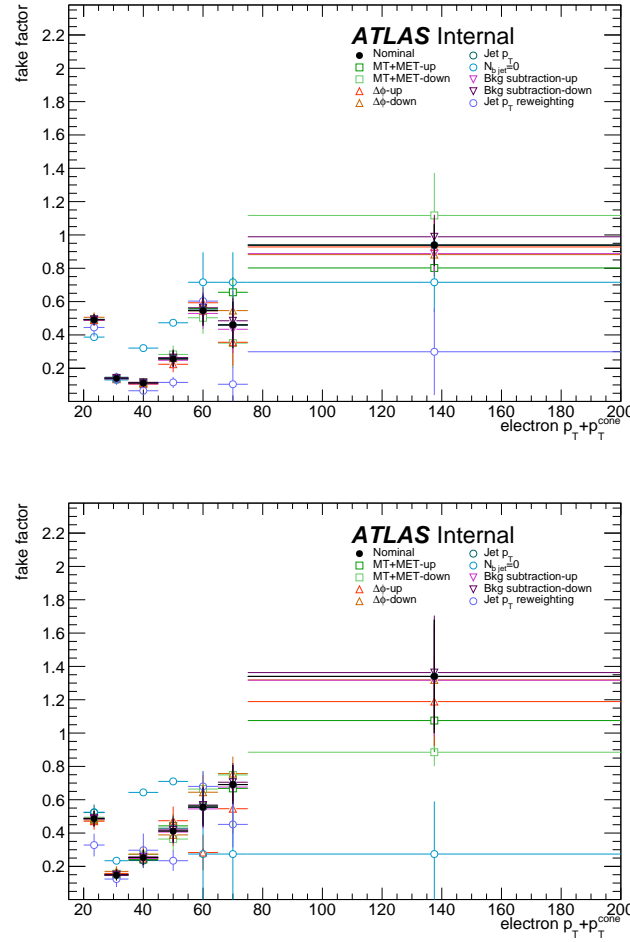


Figure 5.21: Systematic variations in the fake-factor as a function of electron $p_T + p_T^{\text{cone}}$ in the central ($|\eta| < 1.37$, top) and forward ($|\eta| > 1.37$, bottom) regions of the detector. The individual fake-factors obtained for each systematic variation are displayed with their statistical uncertainties.

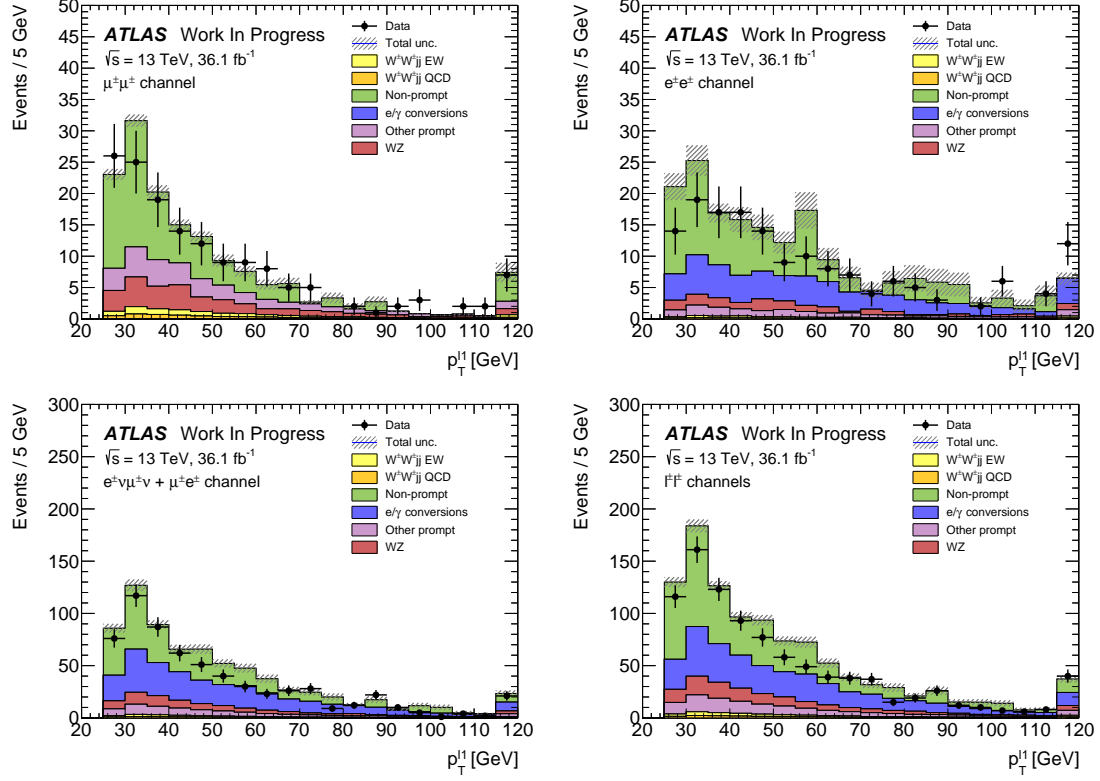


Figure 5.22: Distributions of the subleading lepton p_T in the same-sign top fakes VR for $\mu^\pm\mu^\pm$ events (top right), $e^\pm e^\pm$ events (top left), $\mu^\pm e^\pm$ events (bottom left), and all events combined (bottom right). All errors are statistical only.

1875 5.3.5 Reduction of WZ background using custom overlap removal

1876 The dominant source of prompt background in this analysis comes from WZ events where both
 1877 bosons decay leptonically. Traditionally, the background is dealt with by imposing a veto on any
 1878 event with a third lepton passing some loose identification criteria (the so-called *trilepton veto*).
 1879 In the case of this analysis, if one or more leptons in addition to the two signal leptons pass the
 1880 preselection criteria, the event is rejected. However, WZ events can still enter the signal region if
 1881 one of the leptons fails the preselection or falls outside of the detector’s acceptance.

1882 In order to understand the sources of WZ events that are not removed by the trilepton veto, a
 1883 study was performed on truth-level leptons in $W^\pm W^\pm jj$ and WZ MC samples. Events with three
 1884 truth leptons were selected, and each was matched to its reconstruction-level partner by finding the
 1885 closest $\Delta R(\text{truth}, \text{reco})$ and $\Delta p_T(\text{truth}, \text{reco})$ match. For events surviving the trilepton veto, the
 1886 two signal leptons were removed, and the remaining leptons represent real leptons that failed to

be selected for the veto. Between 40-50% of these leptons fall outside of the eta acceptance of the analysis (see Figure 5.23) and are unrecoverable. The second largest source of leptons failing the preselection is the OR, defined in Section 5.2.1.4. The standard OR procedure appears to be too aggressive in removing leptons in favor of jets, causing many three lepton events to “lose” their third lepton and pass the trilepton veto. Therefore a *custom OR* is investigated which would replace the standard OR in the preselection and allow for better WZ rejection by removing fewer third leptons.

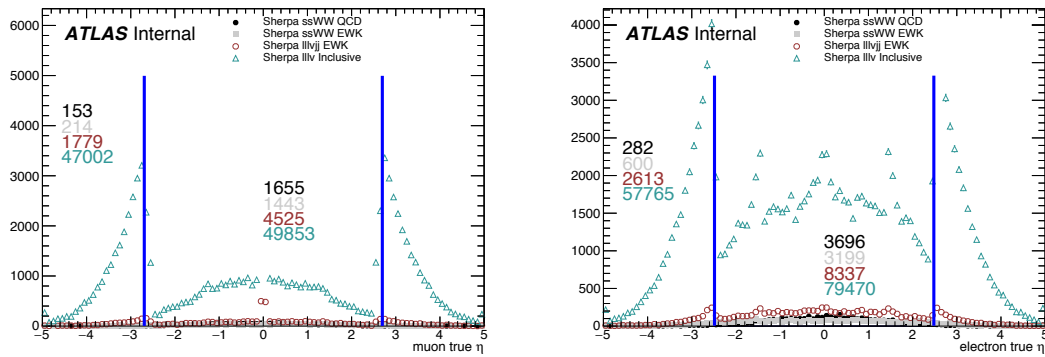


Figure 5.23: Pseudorapidity (η) distributions of truth muons (top) and electrons (bottom) for Sherpa $W^\pm W^\pm jj$ and WZ MC samples. The blue vertical lines represent the allowed η range for each lepton flavor. The numbers correspond to the number of raw MC events that fall within and outside of the allowed η range for each MC sample.

In order to construct this custom OR, a new quantity is defined between a lepton (l) and a nearby jet (j)

$$p_{T,\text{ratio}}(l, j) = \frac{p_{Tl}}{p_{Tj}} \quad (5.13)$$

which, along with $\Delta R(l, j)$, will make up the custom OR criteria. The idea behind including $p_{T,\text{ratio}}$ is to be able to preferentially remove background leptons originating from jets (i.e. those that carry a low percentage of the total jet momentum) instead of removing *any* lepton near a jet. The distributions of $p_{T,\text{ratio}}$ and the associated efficiency curves for muons and electrons can be found in Figures 5.24 and 5.26, respectively, and the distributions for $\Delta R(\mu, j)$ for muons can be found in Figure 5.25. Since all electrons have an associated jet in the calorimeters, the $\Delta R(e, j)$ variable is not a good quantity to use for this custom OR.

A working point for the Custom OR was chosen by requiring 90% signal retention for muons and 90% background rejection for electrons. The cut on electrons was allowed to be much tighter because the number of signal events with a third electron is considerably smaller than for muons. It should be emphasized that the signal events present in Figures 5.24-5.26 do not represent the full

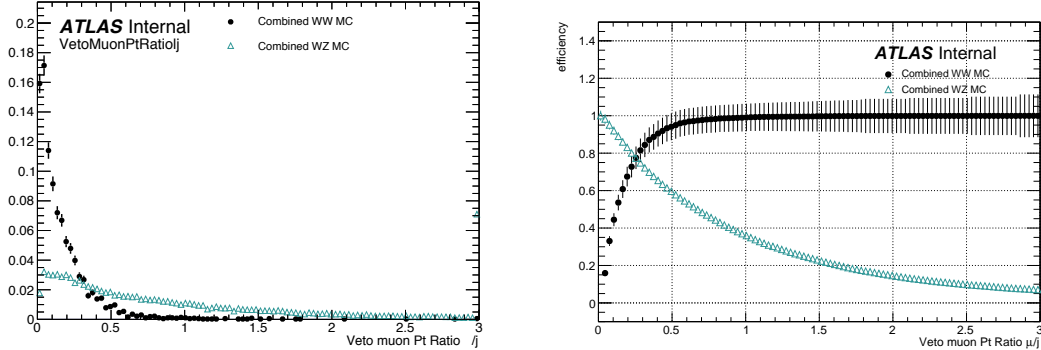


Figure 5.24: Distributions of $p_{T,\text{ratio}}(\mu, j)$ for EWK and QCD $W^\pm W^\pm jj$ signal (black) and WZ background (teal) for truth-matched third muons in events that pass the trilepton veto. Both distributions are normalized to unit area. The associated efficiency curves are on the right where efficiency is defined as the percentage of total events that would pass a cut on $p_{T,\text{ratio}}(\mu, j)$ at a given value on the x -axis.

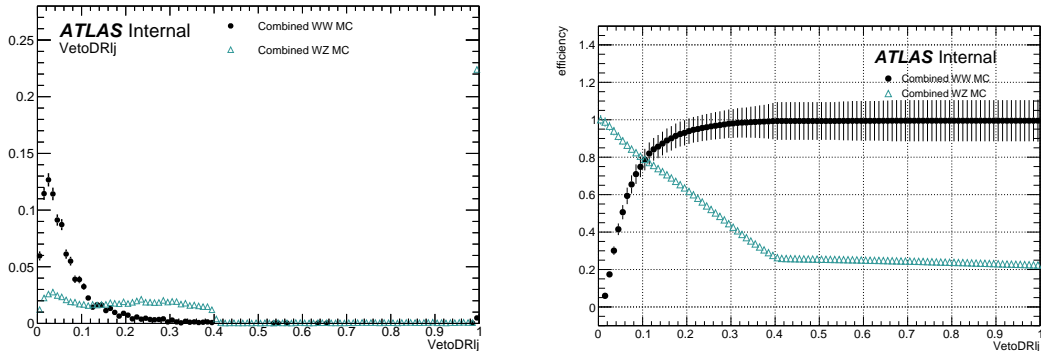


Figure 5.25: Distributions of $\Delta R(\mu, j)$ for EWK and QCD $W^\pm W^\pm jj$ signal (black) and WZ background (teal) for truth-matched third muons in events that pass the trilepton veto. Both distributions are normalized to unit area. The associated efficiency curves are on the right where efficiency is defined as the percentage of total events that would pass a cut on $\Delta R(\mu, j)$ at a given value on the x -axis.

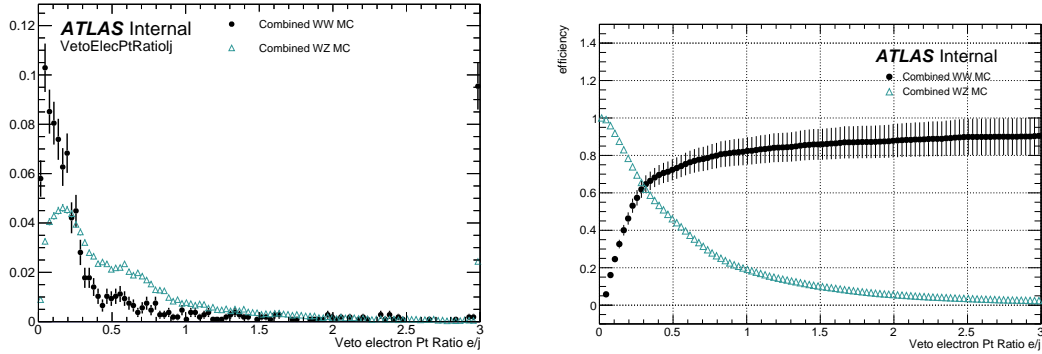


Figure 5.26: Distributions of $p_{T,\text{ratio}}(e,j)$ for EWK and QCD $W^\pm W^\pm jj$ signal (black) and WZ background (teal) for truth-matched third electrons in events that pass the trilepton veto. Both distributions are normalized to unit area. The associated efficiency curves are on the right where efficiency is defined as the percentage of total events that would pass a cut on $p_{T,\text{ratio}}(e,j)$ at a given value on the x -axis.

1906 set of signal events, but only those with a real third lepton (which must come from some source
 1907 other than the signal $W^\pm W^\pm jj$ process). For muons, a logical ‘or’ of $p_{T,\text{ratio}}(\mu,j)$ and $\Delta R(\mu,j)$ is
 1908 used to maximize the third lepton acceptance due to correlations between the quantities, as shown
 1909 in Figure 5.27; for electrons, only a cut on $p_{T,\text{ratio}}(e,j)$ is used. The Custom OR working point is
 1910 defined in Table 5.17.

Custom OR Definition	
Muons	$p_{T,\text{ratio}}(\mu,j) > 0.40$ or $\Delta R(\mu,j) > 0.15$
Electrons	$p_{T,\text{ratio}}(e,j) > 0.18$

Table 5.17: Custom OR definition. Leptons must pass this selection in order to be counted for the trilepton veto.

1911 Initial tests of the performance of the Custom OR yielded promising results, with approximately
 1912 20% reduction in WZ background compared to less than 2% signal loss in the signal region. Unfor-
 1913 tunately, due to differences between the primary analysis framework and the one used for testing,
 1914 in practice the gains in WZ rejection were not nearly as substantial, and ultimately the Custom
 1915 OR was not included in the final analysis. However, it is still a potentially useful tool for improving
 1916 background rejection based on lepton counting in analyses with overly aggressive OR procedures.

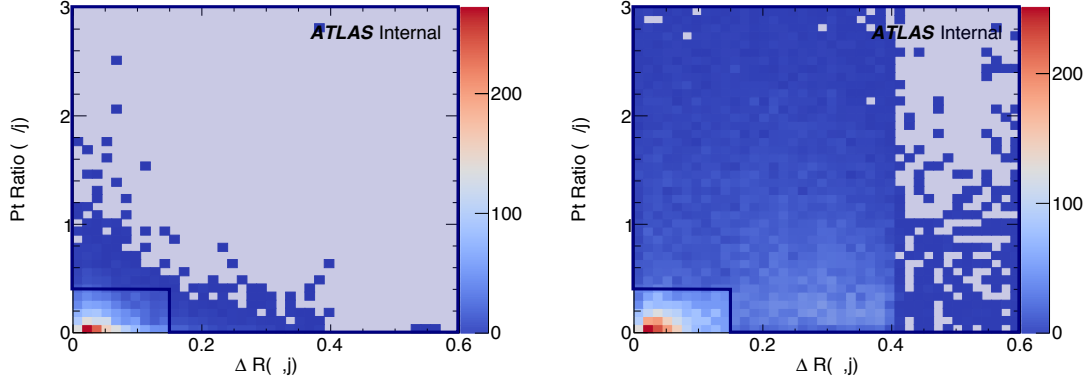


Figure 5.27: Two-dimensional plots of $p_{T,\text{ratio}}(\mu, j)$ vs $\Delta R(\mu, j)$ for truth-matched third muons in events that pass the trilepton veto for EWK and QCD $W^\pm W^\pm jj$ signal (left) and WZ background (right). The blue overlay indicates the area in which the third leptons will pass the custom OR and result in the event failing the trilepton veto.

1917 5.4 Cross section measurement

1918 The $W^\pm W^\pm jj$ EWK cross section is extracted from the signal region using a maximum-likelihood
 1919 fit applied simultaneously to four m_{jj} bins in the signal region as well as to the low- m_{jj} and WZ
 1920 control regions. For the fit and cross section extraction, the signal region is defined as in Table 5.8
 1921 with the dijet invariant mass requirement raised to $m_{jj} > 500$ GeV. The low- m_{jj} region is defined
 1922 to mirror the signal region exactly with the dijet invariant mass inverted to $200 < m_{jj} < 500$ GeV,
 1923 and the WZ control region is defined previously in Section 5.3.1.

1924 The signal and low- m_{jj} regions are split into six channels based on the flavor and charge of
 1925 the dilepton pair: $\mu^+\mu^+$, $\mu^-\mu^-$, μ^+e^+ , μ^-e^- , e^+e^+ , and e^-e^- . This split by charge increases the
 1926 sensitivity of the measurement due to the W^+/W^- charge asymmetry at hadron colliders favoring
 1927 the production of W^+ bosons [101]. Since the signal events contain two W bosons, the signal
 1928 strength compared to charge-symmetric backgrounds is much greater in the $++$ channels for both
 1929 charges combined. The WZ control region is included in the fit as a single bin ($l^\pm l^\mp l^\pm$).

1930 The maximum likelihood fit and cross section extractions are outlined in Sections 5.4.1 and
 1931 5.4.3, respectively. The results of the cross section measurement and of the analysis as a whole are
 1932 presented in Section 5.6.

1933 **5.4.1 Maximum likelihood fit**

1934 The number of predicted signal events in each channel c and m_{jj} bin b can be calculated from the SM
 1935 predicted total production cross section $\sigma_{\text{theo}}^{\text{tot}}$ scaled by the total integrated luminosity \mathcal{L} , the signal
 1936 acceptance \mathcal{A} , and the efficiency corrections $\mathcal{C}(\theta)$. Here θ represents the set of nuisance parameters
 1937 that parameterize the effects of each systematic uncertainty on the signal and background expec-
 1938 tations. The acceptance and efficiency corrections will be covered in more detail in Section 5.4.2.

1939

$$N_{cb}^{\text{sig}}(\theta) = \sigma_{\text{theo}}^{\text{tot}} \mathcal{A}_b \mathcal{C}_b(\theta) \mathcal{L} \quad (5.14)$$

1940 A signal strength parameter μ is defined as the ratio of the measured cross section to the SM
 1941 predicted cross section. The expected number of events in a given channel and bin can then be
 1942 expressed as the sum of the estimated background ($N_{cb}^{\text{bkg}}(\theta)$) and the number of predicted signal
 1943 events scaled by μ :

$$\begin{aligned} N_{cb}^{\text{exp}}(\theta) &= \mu N_{cb}^{\text{sig}}(\theta) + N_{cb}^{\text{bkg}}(\theta) \\ &= \mu \sigma_{\text{theo}}^{\text{tot}} \mathcal{A}_b \mathcal{C}_b(\theta) \mathcal{L} + N_{cb}^{\text{bkg}}(\theta) \end{aligned} \quad (5.15)$$

1944 The nuisance parameters are constrained by Gaussian probability distribution functions, and
 1945 the normalization of the WZ background mentioned in Section 5.3.1 is included in the fit as a free
 1946 parameter. The expected yields for signal and background processes are adjusted by the set of
 1947 nuisance parameters within the constraints of the systematic uncertainties. The yields after the fit
 1948 correspond to the value that best matches the observed data.

1949 The number of events per channel and bin after the fit can be written as a sum of the predicted
 1950 event yields for each sample s :

$$\nu_{cb}(\phi, \theta, \gamma_{cb}) = \gamma_{cb} \sum_s [\eta_{cs}(\theta) \phi_{cs}(\theta) \lambda] h_{cbs}(\theta) \quad (5.16)$$

1951 In this equation, the fitted number of events in a given channel and bin is obtained by weighting
 1952 the histogram of predicted yields h_{cbs} by the product of a given luminosity λ and any normaliza-
 1953 tion factors ϕ_{cs} that may be given for each channel and sample. The input histogram and the normal-
 1954 ization factors may depend on the nuisance parameters θ taking into account sources of systematic
 1955 uncertainty. Uncertainties on the normalization factors $\eta_{cs}(\theta)$ are also included. Finally, bin-by-bin
 1956 scale factors γ_{cb} are included to parameterize the statistical uncertainties of the MC predictions.

1957 The binned likelihood function is given by a product of Gaussian functions for the luminosity
 1958 and for the background uncertainties and a product of Poisson functions for the number of observed

1959 events in each bin and channel:

$$L(\mu|\theta) = \mathcal{G}(\mathcal{L}|\theta_{\mathcal{L}}, \sigma_{\mathcal{L}}) \cdot \prod_c \prod_b \mathcal{P}(N_{cb}^{\text{meas.}} | \nu_{cb}(\mu)) \prod_p \mathcal{G}(\theta_p^0 | \theta_p) \quad (5.17)$$

1960 where \mathcal{G} and \mathcal{P} are the Gaussian and Poisson functions, respectively. As before, \mathcal{L} represents the
 1961 integrated luminosity with uncertainty $\sigma_{\mathcal{L}}$ and associated nuisance parameter $\theta_{\mathcal{L}}$. The number of
 1962 measured events in a given bin and channel is represented by $N_{cb}^{\text{meas.}}$, and $\nu_{cb}(\mu)$ is the predicted
 1963 number of events defined in Equation 5.16 expressed as a function of the signal strength μ . Finally,
 1964 the set of nuisance parameters θ and any auxiliary measurements used to constrain them (θ^0) are
 1965 multiplied for each parameter p .

1966 The profile likelihood ratio is defined as

$$q_{\mu} = -2 \ln \frac{L(\mu, \hat{\theta}_{\mu})}{L(\hat{\mu}, \hat{\theta})} \quad (5.18)$$

1967 where $\hat{\mu}$ and $\hat{\theta}$ are the unconditional maximum likelihood estimates, and $\hat{\theta}$ is the conditional maxi-
 1968 mum likelihood estimate for a given value of μ . The fitted signal strength $\hat{\mu}$ is obtained by maximiz-
 1969 ing the likelihood function with respect to all parameters. The compatibility of the observed data
 1970 with the background-only hypothesis can then be calculated by setting $\mu = 0$. Observation of the
 1971 $W^{\pm}W^{\pm}jj$ EWK process is claimed if the data is found to be inconsistent with the background-only
 1972 hypothesis by more than 5σ .

1973 5.4.2 Definition of the fiducial volume

1974 Before extracting the cross section, it is necessary to define the fiducial volume, or the phase space
 1975 of measureable events. It is a subset of the total phase space defined by selection requirements
 1976 designed to mirror those applied in the analysis as closely as possible. The selection criteria for the
 1977 fiducial volume are listed in Table 5.18.

1978 In MC simulations the total phase space is generated, providing the total theoretical cross section
 1979 $\sigma_{\text{theo}}^{\text{tot}}$ and the total number of signal events $\mathcal{N}_{\text{sig}}^{\text{tot}}$ ¹⁹. After applying the fiducial selection at truth
 1980 level, the total number of signal events in the fiducial region $\mathcal{N}_{\text{sig}}^{\text{fid}}$ is obtained. An acceptance factor
 1981 \mathcal{A} is used to represent the efficiency of events falling inside the fiducial region at truth level:

$$\mathcal{A} = \frac{\mathcal{N}_{\text{sig}}^{\text{fid}}}{\mathcal{N}_{\text{sig}}^{\text{tot}}} \quad (5.19)$$

¹⁹For the purpose of clarity, the number of events at truth level is represented by a script \mathcal{N} , and the number of events at reconstruction level uses a regular N .

Fiducial region selection	
Lepton selection	Two prompt leptons (e, μ) $p_T > 27$ GeV and $ \eta < 2.5$ for both leptons Both leptons with the same electric charge Dilepton invariant mass $m_{ll} > 20$ GeV Dilepton separation $\Delta R(ll) > 0.3$
Missing transverse energy	Two neutrino system with $p_T^{\nu\nu} > 30$ GeV
Jet selection	At least two jets Leading jet $p_T > 65$ GeV Subleading jet $p_T > 35$ GeV Leading and subleading jet $ \eta < 4.5$ Jet-lepton separation $\Delta R(l, j) > 0.3$ Dijet invariant mass $m_{jj} > 500$ GeV Dijet separation $\Delta y_{jj} > 2.0$

Table 5.18: Definition of the fiducial volume.

1982 A correction factor \mathcal{C} is also necessary to translate from the truth level fiducial volume to the
 1983 reconstruction level signal region and is defined in terms of the number of reconstruction level MC
 1984 events in the signal region $N_{\text{sig},\text{MC}}^{\text{SR}}$:

$$\mathcal{C} = \frac{N_{\text{sig},\text{MC}}^{\text{SR}}}{N_{\text{sig}}^{\text{fid}}} \quad (5.20)$$

1985 Since the fit is binned in m_{jj} , the acceptance and efficiency correction factors must be as well.
 1986 Therefore, \mathcal{A}_i and \mathcal{C}_{ij} are written in terms of truth m_{jj} bins i and reconstruction m_{jj} bins j . A
 1987 graphical representation of these regions and the use of the acceptance and correction factors can
 1988 be seen in Figure 5.28.

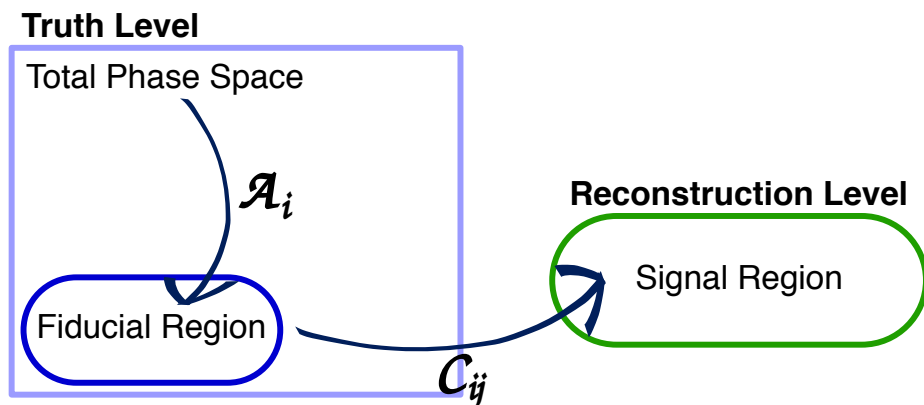


Figure 5.28: Visual representation of the different kinematic regions relevant to the cross section measurement. The acceptance factor \mathcal{A} converts from the truth level total phase space to the truth level fiducial region, and the efficiency correction \mathcal{C} translates the fiducial region into the reconstruction level signal region.

1989 **5.4.3 Cross section extraction**

1990 The $W^\pm W^\pm jj$ EWK fiducial cross section is measured using the signal strength parameter μ that is
 1991 determined by the maximum likelihood fit. This parameter is dependent on the nuisance parameters
 1992 θ and can be written explicitly in terms of the measured and theoretical cross sections as:

$$\mu(\theta) = \frac{\sigma_{\text{meas}}^{\text{SR}}}{\sigma_{\text{theo}}^{\text{SR}}} \quad (5.21)$$

1993 In the simple case with only one bin, the equation for the total number of expected events in the
 1994 signal region first introduced in Equation 5.15 can be written as:

$$N_{\text{exp}}^{\text{SR}}(\theta) = \mu(\theta) \cdot \sigma_{\text{theo}}^{\text{tot}} \cdot \mathcal{L} \cdot \mathcal{A} \cdot \mathcal{C}(\theta) + N_{\text{bkg}}^{\text{SR}}(\theta) \quad (5.22)$$

1995 with the non-binned versions of \mathcal{A} and \mathcal{C} defined in Equations 5.19 and 5.20, respectively.

1996 If the measured fiducial cross section is written as:

$$\sigma_{\text{meas}}^{\text{fid}} = \mu \cdot \mathcal{A} \cdot \sigma_{\text{theo}}^{\text{tot}} \quad (5.23)$$

1997 then Equation 5.22 can be rearranged to read:

$$\sigma_{\text{meas}}^{\text{fid}} = \frac{N_{\text{exp}}^{\text{SR}}(\theta) - N_{\text{bkg}}^{\text{SR}}(\theta)}{\mathcal{L} \cdot \mathcal{C}(\theta)} \quad (5.24)$$

1998 The measured fiducial cross section can finally be rewritten in terms of $\hat{\mu}$, which is the best estimator
 1999 of the signal strength as extracted from the fit:

$$\begin{aligned} \sigma_{\text{meas}}^{\text{fid}} &= \hat{\mu}(\theta) \cdot \sigma_{\text{theo}}^{\text{tot}} \cdot \mathcal{A} \\ &= \hat{\mu}(\theta) \cdot \sigma_{\text{theo}}^{\text{fid}} \end{aligned} \quad (5.25)$$

2000 In practice, however, the cross section is not extracted from a single bin, and Equation 5.22
 2001 becomes:

$$N_{\text{exp}}^{\text{SR}}(\theta) = \mu(\theta) \cdot \sigma_{\text{theo}}^{\text{tot}} \cdot \mathcal{L} \cdot \sum_i \mathcal{A}_i \cdot \sum_j \mathcal{C}_{ij} + \sum_j N_{\text{bkg},j}^{\text{SR}}(\theta) \quad (5.26)$$

2002 for a single channel in truth and reconstruction level m_{jj} bins i and j , respectively, where the binned
 2003 versions of \mathcal{A}_i and \mathcal{C}_{ij} are used. This equation can be extended to include all the analysis channels
 2004 by increasing the number of bins i and j . Additionally, it can be shown that Equation 5.25 holds
 2005 for this more complex case as well [70], provided care is taken to ensure that all the uncertainties
 2006 are handled properly.

2007 5.5 Summary of uncertainties

2008 Systematic uncertainties enter the final fit as nuisance parameters which can impact the estimated
 2009 signal and background yields and the shapes of the m_{jj} distributions. These uncertainties can arise
 2010 from the experimental methods or from the theoretical calculations used in the analysis. This section
 2011 summarizes the systematic uncertainties; the experimental uncertainties are detailed in Section 5.5.1,
 2012 and the theoretical uncertainties are covered in Section 5.5.2. The impacts of the systematic uncer-
 2013 tainties on the final cross section measurement are summarized in Table 5.19.

Source	Impact [%]
Reconstruction	± 4.0
Electrons	± 0.5
Muons	± 1.2
Jets and E_T^{miss}	± 2.8
b -tagging	± 2.0
Pileup	± 1.5
Background	± 5.0
Misid. leptons	± 3.9
Charge misrec.	± 0.3
WZ	± 1.3
$W^\pm W^\pm jj$ QCD	± 2.8
Other	± 0.8
Signal	± 3.6
Interference	± 1.0
EW Corrections	± 1.3
Shower, Scale, PDF & α_s	± 3.2
Total	± 7.4

Table 5.19: Impact of various systematic effects on the fiducial cross section measurement. The impact of a given source of uncertainty is computed by performing the fit with the corresponding nuisance parameter varied up or down by one standard deviation from its nominal value.

2014 5.5.1 Experimental uncertainties

2015 Experimental uncertainties include detector effects as well as uncertainties on the background es-
 2016 timation methods. Sources of systematic uncertainty on the measurement of physics objects are
 2017 listed in Table 5.20, grouped by the relevant object type. For backgrounds estimated from MC
 2018 simulations, variations in these sources of uncertainty are propagated through the analysis to obtain
 2019 the corresponding uncertainties on the event yields. Additional experimental uncertainties include
 2020 the integrated luminosity, the photon conversion rate from Section 5.3.2, and the data driven charge

2021 misidentification and fake lepton background estimations from Sections 5.3.3 and 5.3.4.5, respec-
2022 tively.

2023 The largest sources of experimental uncertainty on the MC estimations come from the jet-related
2024 uncertainties and the b -tagging efficiency, while the largest uncertainty on the background estimation
2025 comes from the fake-factor. The effects of the uncertainties on the $W^\pm W^\pm jj$ EWK signal and the
2026 dominant MC estimated background, WZ , are listed in Tables 5.21 and 5.22, respectively. Since
2027 the overall contributions from other processes estimated with MC are small, the uncertainties on
2028 these backgrounds have a lesser impact on the final measurement; these tables can be found in
2029 Appendix A.1.

Experimental uncertainties	
Electrons	Energy resolution
	Energy scale
	Identification efficiency
	Isolation efficiency
	Reconstruction efficiency
	Trigger efficiency
Muons	Energy scale
	Identification efficiency
	Inner detector track resolution
	Muon spectrometer resolution
	Trigger efficiency
E_T^{miss}	Resolution
	Scale
Jets	Energy resolution
	Energy scale
	JVT cut efficiency
	b -tagging efficiency
	Jets from pileup

Table 5.20: List of sources of experimental uncertainties on the reconstruction of physics objects.

$W^\pm W^\pm jj$ EWK	$e^\pm e^\pm$ % Yield	$\mu^\pm e^\pm$ % Yield	$\mu^\pm \mu^\pm$ % Yield
Jet-related Uncertainties	2.28	2.22	2.28
b -tagging efficiency	1.81	1.76	1.74
Pile-up	0.48	0.97	2.42
Trigger efficiency	0.02	0.08	0.47
Lepton reconstruction/ID	1.45	1.14	1.83
MET reconstruction	0.26	0.17	0.21

Table 5.21: Impact of experimental uncertainties for the $W^\pm W^\pm jj$ EWK processes in all channels.

WZ	$e^\pm e^\pm$ % Yield	$\mu^\pm e^\pm$ % Yield	$\mu^\pm \mu^\pm$ % Yield
Jet-related Uncertainties	9.58	5.03	8.45
b-tagging efficiency	2.49	2.23	2.40
Pile-up	2.99	3.49	3.33
Trigger efficiency	0.03	0.09	0.43
Lepton reconstruction/ID	1.52	1.24	3.07
MET reconstruction	0.93	0.79	1.63

Table 5.22: Impact of experimental uncertainties for the WZ process in all channels.2030 **5.5.2 Theoretical uncertainties**

2031 It is also necessary to consider uncertainties on the theoretical predictions in the fiducial region. They
 2032 include the choice of PDF set, the value of the strong coupling constant α_s , the renormalization
 2033 scale μ_R , the factorization scale μ_F , and the parton showering. The size of these uncertainties
 2034 are measured by generating new samples with variations in a chosen parameters and comparing
 2035 them to samples using the nominal choice of the parameter. Internal variations on the PDF sets
 2036 and using a different set entirely results in a relative uncertainty of up to 2.25% on the nominal
 2037 sample. The impact from varying α_s is very small, on the order of < 0.01%. The factorization and
 2038 renormalization scales are independently varied between 0.5-2.0 from their nominal values of 1.0.
 2039 This results in relative uncertainties on the prediction of up to 15%. Finally, varying the parameters
 2040 in the parton showering results in up to 8% uncertainty.

2041 **5.5.2.1 Uncertainties from EWK-QCD interference**

2042 As mentioned in Section 5.0.1, $W^\pm W^\pm jj$ production consists of both EWK processes. The two
 2043 production modes cannot be naively separated due to cross terms in the matrix element calculation.
 2044 These cross terms are referred to as *interference* terms. Since the $W^\pm W^\pm jj$ EWK production is
 2045 the focus of the analysis, and the signal region is designed to preferentially select those events, it is
 2046 important to measure the size of the EWK-QCD interference contributions.

2047 The interference effects are estimated using the `MadGraph` MC generator, as it has a feature that
 2048 allows direct modelling of the interference term. This allows four samples to be generated:

- 2049 1. Inclusive: All available diagrams are used in the matrix element calculation
- 2050 2. EWK only: Only EWK diagrams ($\mathcal{O}(\alpha_{\text{EWK}}) = 4$) are used
- 2051 3. QCD only: Only QCD diagrams ($\mathcal{O}(\alpha_s) = 2 \otimes \mathcal{O}(\alpha_{\text{EWK}}) = 2$) are used

2052 4. Interference: Only the interference terms are used

2053 A minimal set of generator level cuts, listed in Table 5.23, is applied in order to avoid biasing the
 2054 sample towards either production mode. The cross sections for each of the four channels can be
 2055 found in Table 5.24. The size of the interference is found to be approximately 6% of the total cross
 2056 section and is taken as a systematic uncertainty.

Generator level cuts
$\Delta\eta_{jj} < 10$
Jet $p_T > 20$ GeV
$M_{jj} > 10$ GeV

Table 5.23: The set of generator level cuts used for generating the interference samples with **MadGraph**.

Sample	σ (fb)
Inclusive	3.646 ± 0.0012
EWK only	2.132 ± 0.0005
QCD only	1.371 ± 0.0008
Interference	0.227 ± 0.0002

Table 5.24: Cross sections for each different $W^\pm W^\pm jj$ production mode (inclusive, EWK only, QCD only, and interference only) generated using **MadGraph**. The cross sections are calculated using a minimal set of generator level cuts from events where the W decays to a muon.

2057 5.6 Results

2058 After running the full analysis chain, the event yields in the signal region, low- m_{jj} control region,
 2059 and WZ control region as well as associated nuisance parameters representing the uncertainties are
 2060 passed to the maximum likelihood fit. From this fit, the normalization factor for the WZ control
 2061 region μ_{WZ} and the signal strength parameter in the signal region μ_{obs} are determined, and the
 2062 predicted yields in each input bin have been shifted according to the process detailed in Section 5.4.1.

2063 The WZ normalization factor is measured to be:

$$\mu_{WZ} = 0.88^{+0.07}_{-0.07}(\text{stat})^{+0.31}_{-0.21}(\text{theory})^{+0.22}_{-0.11}(\text{sys}) \quad (5.27)$$

2064 and is constrained primarily by the number of data events in the WZ control region. The observed
 2065 signal strength of $W^\pm W^\pm jj$ EWK production, defined in Equation 5.21, is extracted from the fit
 2066 and measured with respect to the prediction of the **SHERPA v2.2.2** MC generator:

$$\mu_{\text{obs}} = 1.45^{+0.25}_{-0.24}(\text{stat})^{+0.06}_{-0.08}(\text{theory})^{+0.27}_{-0.22}(\text{sys}) \quad (5.28)$$

2067 This corresponds to a rejection of the background-only hypothesis with a significance of 6.9σ .

2068 The observed number of data events are compared to the predicted signal and background yields
 2069 in the signal region in Table 5.25 before applying the fit and in Table 5.26 after the fit. 122 candidate
 2070 events are observed compared to a prediction of 60 signal and 69 background events.

2071 The m_{jj} distributions for data and prediction are shown in Figure 5.29 after the fit, and the
 2072 fitted event yields in the low- m_{jj} and WZ control regions are shown in Figure 5.30. Additional
 2073 distributions can be found in Appendix A.

	e^+e^+	e^-e^-	μ^+e^+	μ^-e^-	$\mu^+\mu^+$	$\mu^-\mu^-$	combined
WZ	1.9 ± 0.6	1.3 ± 0.4	14 ± 4	8.9 ± 2.6	5.5 ± 1.6	3.6 ± 1.1	35 ± 10
Non-prompt	4.1 ± 2.3	2.3 ± 1.7	9 ± 5	6 ± 4	0.57 ± 0.15	0.67 ± 0.25	23 ± 10
e/γ conversions	1.74 ± 0.29	1.8 ± 0.4	6.1 ± 1.6	3.7 ± 0.8	—	—	13.4 ± 2.5
Other prompt	0.17 ± 0.05	0.14 ± 0.04	0.90 ± 0.19	0.60 ± 0.14	0.36 ± 0.10	0.19 ± 0.05	2.4 ± 0.5
$W^\pm W^\pm jj$ QCD	0.38 ± 0.13	0.16 ± 0.05	3.0 ± 1.0	1.2 ± 0.4	1.8 ± 0.6	0.76 ± 0.25	7.3 ± 2.5
Expected background	8.2 ± 2.4	5.7 ± 1.8	33 ± 7	21 ± 5	8.2 ± 1.8	5.3 ± 1.2	81 ± 14
$W^\pm W^\pm jj$ EWK	3.8 ± 0.6	1.49 ± 0.22	16.5 ± 2.5	6.5 ± 1.0	9.1 ± 1.4	3.5 ± 0.5	41 ± 6
Data	10	4	44	28	25	11	122

Table 5.25: Table of the data and prediction event yields in the signal region before the fit. Numbers are shown for the six lepton flavor and charge channels and for all channels combined. Here the WZ background yields are normalized to the data in the WZ control region. The background estimations from the fake-factor are included in the “Non-prompt” category, and backgrounds from $V\gamma$ production and electron charge misidentification are combined in the “ e/γ conversions” category. Finally, ZZ , VVV , and $t\bar{t} + V$ backgrounds are combined in the “Other prompt” category.

	e^+e^+	e^-e^-	μ^+e^+	μ^-e^-	$\mu^+\mu^+$	$\mu^-\mu^-$	combined
WZ	1.49 ± 0.30	1.10 ± 0.26	11.7 ± 1.7	8.0 ± 1.3	5.0 ± 0.6	3.5 ± 0.6	31 ± 4
Non-prompt	2.2 ± 1.3	1.2 ± 0.7	5.7 ± 2.8	4.5 ± 1.8	0.57 ± 0.06	0.65 ± 0.14	15 ± 6
e/γ conversions	1.6 ± 0.4	1.6 ± 0.5	6.3 ± 1.6	4.3 ± 1.1	—	—	13.8 ± 2.9
Other prompt	0.16 ± 0.04	0.14 ± 0.04	0.90 ± 0.19	0.63 ± 0.13	0.39 ± 0.09	0.22 ± 0.05	2.4 ± 0.5
$W^\pm W^\pm jj$ QCD	0.35 ± 0.13	0.15 ± 0.05	2.9 ± 1.0	1.2 ± 0.4	1.8 ± 0.6	0.76 ± 0.25	7.2 ± 2.4
Expected background	5.8 ± 1.5	4.1 ± 1.1	27 ± 4	18.7 ± 2.6	7.7 ± 0.8	5.1 ± 0.6	69 ± 7
$W^\pm W^\pm jj$ EWK	5.6 ± 1.0	2.2 ± 0.4	24 ± 5	9.4 ± 1.8	13.5 ± 2.5	5.2 ± 1.0	60 ± 11
Data	10	4	44	28	25	11	122

Table 5.26: Table of the data and prediction event yields in the signal region after the fit. Numbers are shown for the six lepton flavor and charge channels and for all channels combined. The background estimations from the fake-factor are included in the “Non-prompt” category, and backgrounds from $V\gamma$ production and electron charge misidentification are combined in the “ e/γ conversions” category. Finally, ZZ , VVV , and $t\bar{t}V$ backgrounds are combined in the “Other prompt” category.

2074 The last ingredient necessary to measure the $W^\pm W^\pm jj$ EWK cross section is the theory predicted
 2075 cross section in the fiducial region defined in Table 5.18. SHERPA v2.2.2 is used for the calculation,
 2076 and the cross section in the total generator phase space is 40.81 ± 0.05 fb, and the fiducial cross section
 2077 is 2.01 ± 0.02 fb. This corresponds to an acceptance factor of $\mathcal{A} = 0.0493 \pm 0.0002$. Uncertainties on

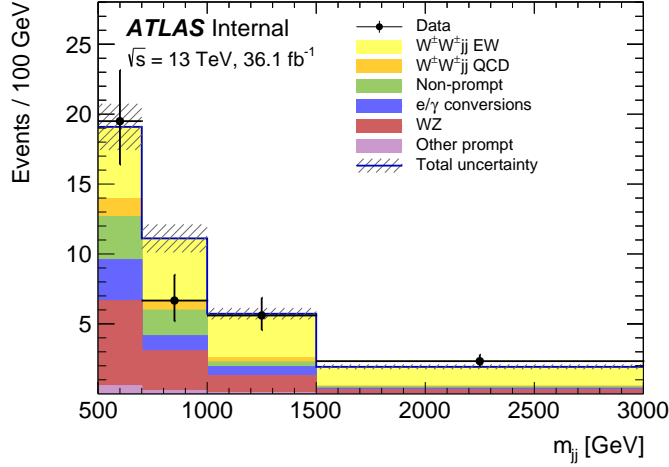


Figure 5.29: The dijet invariant mass m_{jj} distributions for data and predicted signal and background in the signal region after the fit. The shaded band represents the statistical and systematic uncertainties added in quadrature. Note that the bins have been scaled such that they represent the number of events per 100 GeV in m_{jj} . The background estimations from the fake-factor are included in the “Non-prompt” category, and backgrounds from $V\gamma$ production and electron charge misidentification are combined in the “ e/γ conversions” category. Finally, ZZ , VVV , and $t\bar{t} + V$ backgrounds are combined in the “Other prompt” category.

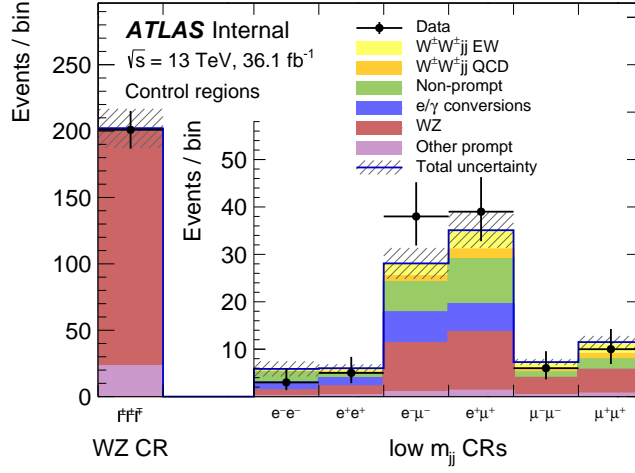


Figure 5.30: The event yields for data and predicted signal and background in the WZ and low- m_{jj} control regions after the fit. The shaded band represents the statistical and systematic uncertainties added in quadrature. The background estimations from the fake-factor are included in the “Non-prompt” category, and backgrounds from $V\gamma$ production and electron charge misidentification are combined in the “ e/γ conversions” category. Finally, ZZ , VVV , and $t\bar{t}V$ backgrounds are combined in the “Other prompt” category.

2078 the simulation are estimated using variations of the scale, parton shower, and PDF set. The final
 2079 prediction used in the cross section measurement including uncertainties from Section 5.5.2 is:

$$\sigma_{\text{SHERPA}}^{\text{fid}} = 2.01 \pm 0.02(\text{stat}) \pm^{+0.29}_{-0.23}(\text{scale}) \pm^{+0.16}_{-0.02}(\text{parton shower}) \pm^{+0.05}_{-0.03}(\text{PDF}) \text{ fb} \quad (5.29)$$

2080 Combining this **SHERPA** prediction with the measured signal strength μ_{obs} from Equation 5.28,
 2081 the measured fiducial cross section $\sigma_{\text{meas}}^{\text{fid}}$ can be calculated using Equation 5.25:

$$\sigma_{\text{meas}}^{\text{fid}} = 2.91 \pm^{+0.51}_{-0.47}(\text{stat}) \pm^{+0.12}_{-0.16}(\text{theory}) \pm^{+0.24}_{-0.23}(\text{sys}) \pm^{+0.08}_{-0.06}(\text{luminosity}) \text{ fb} \quad (5.30)$$

2082 A plot comparing the measured fiducial cross section to two theoretical calculations is shown in
 2083 Figure 5.31. The measured value is compared to the **SHERPA v2.2.2** prediction used to calculate
 2084 μ_{obs} as well as to **POWHEG-BOX v2**. As mentioned in Section 5.1.1, this **POWHEG** sample does not
 2085 include the resonant triboson diagrams and is only used here for a visual comparison.

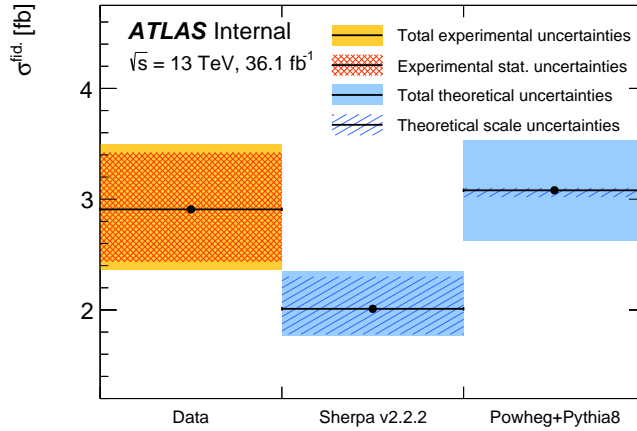


Figure 5.31: Comparison of the measured $W^\pm W^\pm jj$ EWK fiducial cross section with theoretical calculations from **SHERPA v2.2.2** and **POWHEG-BOX v2**. The light orange band represents the total experimental uncertainty on the measured value, and the dark orange hashed band is the statistical uncertainty. For the simulations, the light blue band represents the total theoretical uncertainty, and the dark blue hashed band are the scale uncertainties. The theory predictions do not include the interference between the EWK and QCD production.

2086

CHAPTER 6

2087

Prospects for same-sign WW at the High Luminosity LHC

2088

2089 On December 3, 2018, Run 2 of the LHC officially ended, and the collider was shut down to begin
 2090 the first of two scheduled extended maintenance periods [102]. During these two long shutdowns,
 2091 the Phase-I and Phase-II upgrades of the LHC and ATLAS will occur in order to prepare for the
 2092 High-Luminosity LHC (HL-LHC) which is scheduled to begin operation in 2026 [103].

2093 The HL-LHC is planned to run at a center-of-mass energy of $\sqrt{s} = 14$ TeV with an instantaneous
 2094 luminosity of $\mathcal{L} = 5 \times 10^{34}$ cm $^{-2}$ s $^{-1}$ with up to 200 collisions per beam-crossing. Over the course
 2095 of operation, the HL-LHC is expected to collect a total integrated luminosity of $\mathcal{L} = 3000$ fb $^{-1}$ by
 2096 2035 [104].

2097 These run conditions will be much harsher than what ATLAS has experienced so far, and there
 2098 are several upgrades planned to adapt the detector to the high luminosity environment. Most
 2099 notably, the entire ID will be replaced with an all-silicon tracker which will extend the coverage
 2100 from $|\eta| \leq 2.7$ up to $|\eta| \leq 4.0$. This will allow for forward particle tracks to be reconstructed, which
 2101 can in turn be matched to clusters in the calorimeters for use in electron identification or forward
 2102 jet tagging [105].

2103 The upgraded detector, the higher beam energy, and the increased volume of data to be col-
 2104 lected provides the opportunity to measure rare processes to a much higher precision than what
 2105 is possible with the current LCH dataset. Same-sign $W^\pm W^\pm jj$ production is one such process.
 2106 With greater statistics, the accuracy of the cross section measurement can be improved over the
 2107 13 TeV analysis detailed in Chapter 5, and it also will allow for more detailed physics studies, such
 2108 as measuring the polarization state of the scattered W bosons. A measurement of the cross section

of longitudinally polarized $W^\pm W^\pm jj$ scattering is one of the most enticing extensions of the existing $W^\pm W^\pm jj$ measurements due to its sensitivity to the EWSB mechanism [106], and it is expected to be measurable for the first time at the HL-LHC. The analysis detailed in this chapter is based off of the 2018 ATLAS HL-LHC $W^\pm W^\pm jj$ prospects study [107] which extends upon the results of the previous year's study [108].

6.0.1 Analysis Overview

The experimental signature of interest is identical to the 13 TeV analysis (see Chapter 5): two prompt leptons (either electrons or muons) with the same electric charge, missing transverse energy, and two high energy forward jets. These jets are again required to have a large angular separation and a high combined invariant mass to preferentially select EWK-produced $W^\pm W^\pm jj$ events.

Background processes are not expected to change with respect to the 13 TeV analysis and are summarized here. The dominant source of prompt background comes from $WZ+jets$ events where both bosons decay leptonically. If the lepton from the Z -decay with opposite charge from the W falls outside of the detector acceptance or is not identified, the remaining two leptons will form a same-sign pair, and the event may pass the signal lepton criteria. To a much lesser extent, $ZZ+jets$ events can enter the signal region this way provided two leptons are “lost”. Other prompt sources include $t\bar{t}+V$ and multiple parton interactions, however both contributions are small. Overall, prompt backgrounds are expected to contribute less than in current analyses due to the addition of forward tracking in the upgraded ATLAS detector reducing the probability of leptons falling outside the detector acceptance. Jets mis-reconstructed as leptons or leptons from hadronic decays (such as $t\bar{t}$ and $W+jets$ production) comprise the non-prompt lepton background. Lastly, events with two prompt, opposite-charge electrons can appear as a same-sign event provided one of the electrons is mis-reconstructed and assigned the wrong charge.

In this analysis, the EWK production of $W^\pm W^\pm jj$ is studied in the context of the planned HL-LHC run conditions and upgraded ATLAS detector. An optimized event selection (referred to as the *optimized selection*) is also explored in an effort to gain increased signal significance over the *default selection*. The cross section of the inclusive EWK production is measured for both the default and optimized selections, and the extraction of the expected longitudinal scattering significance is measured with the optimized selection.

2138 **6.1 Theoretical motivation**

2139 The motivation for studying the $W^\pm W^\pm jj$ process as well as VBS in general has been established
 2140 previously in Sections 2.3 and 5.0.1. Since only the longitudinally polarized vector bosons that is
 2141 sensitive to the EWSB mechanism, a direct measurement of this cross section will be very useful for
 2142 understanding how the Higgs unitarizes the scattering amplitude [106].

2143 **6.1.1 Experimental sensitivity to longitudinal polarization**

2144 There are three possible polarization states for a massive vector boson: two transverse (+ or -)
 2145 and one longitudinal (0). Therefore, in a system with two W bosons, the overall polarization can be
 2146 purely longitudinal (00), purely transverse (++, --, and +-), or mixed (+0 and -0). The three
 2147 combinations will be referred to as *LL*, *TT*, and *LT* respectively.

2148 In order extract the longitudinal scattering component, it is necessary to find variables that can
 2149 help distinguish the LL from the TT and LT events. Several were studied, and those with the best
 2150 discriminating power between the different polarization states are the leading and subleading lepton
 2151 transverse momenta as well as the azimuthal separation of the two VBS jets $|\Delta\phi_{jj}|$. Both leptons
 2152 in LL events tend to be softer than the TT and LT events (see Figure 6.1), which motivates keeping
 2153 cuts on the lepton p_T as low as possible in the event selection. In the case of the dijet separation, LL
 2154 events prefer the tag jets to be back-to-back (see Figure 6.2). $|\Delta\phi_{jj}|$ is passed to a binned likelihood
 2155 fit to extract the longitudinal scattering significance.

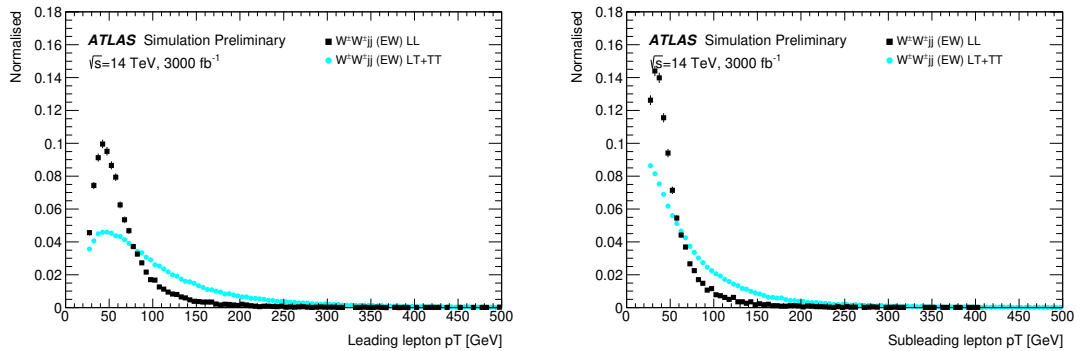


Figure 6.1: Comparison of the leading (left) and subleading (right) lepton p_T distributions for purely longitudinal (LL, black) and mixed polarization (LT+TT, cyan) $W^\pm W^\pm jj$ events.

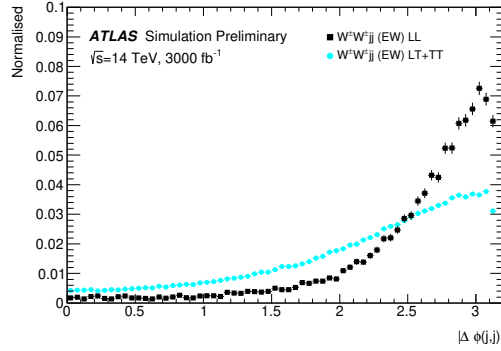


Figure 6.2: Comparison of the azimuthal dijet separation ($|\Delta\phi_{jj}|$) for purely longitudinal (LL, black) and mixed polarization (LT+TT, cyan) $W^\pm W^\pm jj$ events.

2156 6.2 Monte Carlo samples

2157 As this is a prospects study for a future collider, all signal and background processes are modeled
 2158 using MC simulations. The samples are generated at the expected HL-LHC center of mass energy
 2159 $\sqrt{s} = 14$ TeV, and the event yields are scaled to the anticipated integrated luminosity of $\mathcal{L} =$
 2160 3000 fb^{-1} . The MC samples used in the analysis are generated at particle-level and have not been
 2161 run through the full simulation of the ATLAS detector. Instead, smearing functions derived from
 2162 a GEANT4 simulation of the upgraded ATLAS detector are used to estimate detector effects such as
 2163 momentum resolution. In addition, pileup events are fully simulated. The MC samples used in this
 2164 analysis are summarized in Table 6.1.

2165 The signal sample consists of both VBS and non-VBS electroweak (EWK) $W^\pm W^\pm jj$ production,
 2166 and it is simulated with the `Madgraph5_aMC@NLO` generator using the NNPDF3.0 PDF set and in-
 2167 terfaced with PYTHIA v8 [109] for hadronization and parton showering. To study the longitudinal
 2168 polarization more directly, two additional `Madgraph5_aMC@NLO` $W^\pm W^\pm jj$ samples are used: one
 2169 containing only the longitudinal contribution (LL) and a second containing the transverse (TT) and
 2170 mixed (LT) contributions.

2171 There are many other processes that can produce the same final state as the $W^\pm W^\pm jj$ and must
 2172 also be accounted for using MC simulations. WZ events are generated using `SHERPA v2.2.0`, which
 2173 includes up to one parton at NLO in the strong coupling constant and up to three additional partons
 2174 at LO. Both EWK and QCD production are included in these samples. ZZ and triboson VVV
 2175 ($V = W, Z$) events are generated using `SHERPA v2.2.2` with up to two additional partons in the
 2176 final state. For the triboson backgrounds, the bosons can decay leptonically or hadronically. $W+jets$

Process	Generator	Comments
$W^\pm W^\pm jj$ (EWK)	<code>Madgraph5_aMC@NLO</code>	Signal sample
$W^\pm W^\pm jj$ (QCD)	<code>Madgraph5_aMC@NLO</code>	
$W^\pm W^\pm jj$ (LL)	<code>Madgraph5_aMC@NLO</code>	Pure longitudinal polarization sample
$W^\pm W^\pm jj$ (TT+LT)	<code>Madgraph5_aMC@NLO</code>	Mixed and transverse polarization sample
Diboson	<code>SHERPA v2.2.0</code>	WZ events
	<code>SHERPA v2.2.2</code>	ZZ events
Triboson	<code>SHERPA v2.2.2</code>	
$W+jets$	<code>Madgraph5_aMC@NLO</code>	
$Z+jets$	<code>POWHEG-BOX v2</code>	
$t\bar{t}$	<code>POWHEG-BOX</code>	
Single top	<code>POWHEG-BOS</code>	

Table 6.1: Summary of MC samples used in the analysis.

backgrounds are generated for electron, muon, and tau final states at LO with `Madgraph5_aMC@NLO` and the `NNPDF3.0` PDF set with showering from `PYTHIA v8`. $Z+jets$ events are produced using `POWHEG-BOX v2` and the `CT10` PDF set interfaced with `PYTHIA v8`. Finally, $t\bar{t}$ and single-top events are generated using `POWHEG-BOX` with showering from `PYTHIA v6`.

6.3 Background estimations

In this analysis, all background contributions are estimated using MC simulations. Backgrounds from electron charge misidentification and fake electrons from jets, which are traditionally estimated using data-driven techniques, are instead estimated using a set of parameterization functions applied to the MC. These functions calculate the probability that an electron is assigned the wrong charge or a jet is mis-reconstructed as an electron parameterized by the p_T and η of the respective electron or jet. The probabilities are derived from studies on expected electron performance with the upgraded ATLAS detector [110].

Processes involving two W or Z bosons are grouped together as *diboson* backgrounds, with the exception of $W^\pm W^\pm jj$ events produced via QCD interactions, which are kept separate. Similarly, all backgrounds with three vector bosons are combined and labeled as *triboson*. Any $W+jets$ or top events that pass selection and do not contain a fake electron, as well as any $Z+jets$ events without an electron identified as having its charge misidentified are combined as *other non-prompt* backgrounds.

2194 **6.3.1 Truth-based isolation**

2195 The canonical isolation variables used in ATLAS analyses require detailed information from many
 2196 detector subsystems including particle tracks and calorimeter responses. Since the MC samples used
 2197 in this analysis have not been run through a full detector simulation, it is not possible to reproduce
 2198 the official isolation variables. For truth-level analysis, this is generally not a serious concern, as
 2199 high- p_T signal leptons tend to be well isolated to begin with. However, isolation is one of the
 2200 most powerful tools for rejecting leptons from non-prompt sources, such as top events, which are
 2201 produced in association with additional nearby particles from b and c hadron decays. It was seen in
 2202 the early stages of this analysis that without any sort of isolation requirement, contributions from
 2203 top backgrounds (including single top, $t\bar{t}$ and $t\bar{t} + V$) were more than an order of magnitude higher
 2204 than expected.

2205 As a result, it is necessary to find one or more quantities that are comparable to the isolation
 2206 information that is available in fully-simulated samples. Analogues to track- and calorimeter-based
 2207 isolation are constructed by summing the momentum and energy, respectively, of stable truth parti-
 2208 cles with $p_T > 1$ GeV within a specified radius of each signal lepton. For the track-based isolation,
 2209 only charged truth particles are used; both charged and neutral particles (excluding neutrinos) are
 2210 included for the calorimeter-based isolation. Ultimately, a set of isolation cuts are chosen that are
 2211 similar to those recommended by ATLAS for Run 2 analyses. The truth-based isolation requirements
 2212 are listed in Table 6.2.

	Electron Isolation	Muon Isolation
Track-based isolation cone size	$\Delta R < 0.2$	$\Delta R < 0.3$
Track-based isolation requirement	$\sum p_T/p_T^e < 0.06$	$\sum p_T/p_T^\mu < 0.04$
Calorimeter-based isolation cone size	$\Delta R < 0.2$	$\Delta R < 0.2$
Calorimeter-based isolation requirement	$\sum E_T/p_T^e < 0.06$	$\sum E_T/p_T^\mu < 0.15$

Table 6.2: Truth-based isolation requirements for electrons and muons.

2213 With no cut on truth-based isolation, 83% of the total background consists of top events without
 2214 including contributions to the fake electron background. The isolation requirement reduces the top
 2215 background by over 99%, and the percentage of the total background from top events is reduced to
 2216 2%. Additional studies on the truth-based isolation as well as full event yields with and without the
 2217 isolation requirement can be found in Appendix B.1.

2218 **6.4 Object and event selection**

2219 The majority of the default object and event selections were determined in the preceeding $W^\pm W^\pm jj$
 2220 HL-LHC prospects study [108], which focused on the impact of the upgraded detector's forward
 2221 tracking capabilities. Several different combinations of lepton and jet η ranges were tested, and the
 2222 results are used in this study.

2223 **6.4.1 Object selection**

2224 Electrons and muons are preselected to have $p_T > 7$ and 6 GeV, respectively, and lie within $|\eta| \leq 4.0$.
 2225 The likelihood of a given lepton to pass the trigger and identification requirements is estimated by
 2226 calculating an efficiency dependent on the p_T and η of the lepton. The leptons are also required to
 2227 pass the isolation criteria detailed in Table 6.2. Jets that have been tagged as a fake electron by the
 2228 functions described in Section 6.3 are treated as electrons for the purpose of the object selection and
 2229 are subject to the same criteria. In order to be considered a signal lepton, the transverse momentum
 2230 requirement is raised to $p_T > 25$ GeV. The two highest p_T leptons passing this selection are chosen
 2231 to be the leading and subleading signal leptons.

2232 Jets are clustered using the anti- k_t algorithm from final-state particles within a radius of $\Delta R =$
 2233 0.4 (excluding muons and neutrinos). All jets are required to have $p_T > 30$ GeV and lie within $|\eta| <$
 2234 4.5 ; in order to suppress jets from pileup interactions, jets outside of $|\eta| \geq 3.8$ must pass an higher
 2235 momentum cut of $p_T > 70$ GeV. Jets overlapping a preselected electron within $\Delta R(e, j) < 0.05$ are
 2236 removed in order to prevent double counting. The two highest p_T jets are defined as the leading
 2237 and subleading tag jets.

2238 **6.4.2 Event selection**

2239 The default event selection is summarized in Table 6.3 and described here. Exactly two signal
 2240 leptons are required with the same electric charge and separated from each other by $\Delta R(ll) > 0.3$.
 2241 In order to suppress contributions from Drell-Yan backgrounds, the two signal leptons must have
 2242 an invariant mass m_{ll} greater than 20 GeV. Additionally, if both signal leptons are electrons, their
 2243 mass must be at least 10 GeV away from the Z -boson mass in order to reduce background from
 2244 Z -boson decays²⁰. The event is required to have at least 40 GeV of missing transverse energy (E_T^{miss})

²⁰The electron charge misidentification rate in the upgraded ATLAS detector is estimated to be high enough that contributions from $Z \rightarrow ee$ backgrounds are non-negligible.

Selection requirement	Selection value
Lepton kinematics	$p_T > 25 \text{ GeV}$ $ \eta \leq 4.0$
Jet kinematics	$p_T > 30 \text{ GeV}$ for $ \eta \leq 4.5$ $p_T > 70 \text{ GeV}$ for $ \eta > 3.8$
Dilepton charge	Exactly two signal leptons with same charge
Dilepton separation	$\Delta R_{l,l} \geq 0.3$
Dilepton mass	$m_{ll} > 20 \text{ GeV}$
Z boson veto	$ m_{ee} - m_Z > 10 \text{ GeV}$ (ee -channel only)
E_T^{miss}	$E_T^{\text{miss}} > 40 \text{ GeV}$
Jet selection	At least two jets with $\Delta R_{l,j} > 0.3$
b jet veto	$N_{\text{b-jet}} = 0$
Dijet separation	$\Delta \eta_{jj} > 2.5$
Trilepton veto	No additional preselected leptons
Dijet mass	$m_{jj} > 500 \text{ GeV}$
Lepton-jet centrality	$\zeta > 0$

Table 6.3: Summary of the signal event selection.

2245 to account for the two final-state neutrinos. Events with additional preselected leptons are vetoed,
 2246 which greatly reduces WZ and ZZ backgrounds.

2247 Each event must have at least two jets, and both tag jets are required to not overlap with the
 2248 signal leptons. Events with one or more b -jets are vetoed to suppress backgrounds from heavy-flavor
 2249 decays. In order to preferentially select EWK production, the tag jets are required to have a large
 2250 separation between them and a large invariant mass. Finally, a cut on the lepton centrality²¹, ζ ,
 2251 defined in Equation 6.1 further enhances the EWK $W^\pm W^\pm jj$ signal.

$$\zeta = \min[\min(\eta_{\ell 1}, \eta_{\ell 2}) - \min(\eta_{j 1}, \eta_{j 2}), \max(\eta_{j 1}, \eta_{j 2}) - \max(\eta_{\ell 1}, \eta_{\ell 2})] \quad (6.1)$$

2252

2253 6.5 Selection optimization

2254 The default event selection is optimized in order to improve the strength of the $W^\pm W^\pm jj$ EWK
 2255 signal. The expectation is that the increased detector acceptance from the forward tracking combined
 2256 with an increase in center of mass energy and much higher integrated luminosity will allow tighter
 2257 selection cuts without jeopardizing signal statistics.

²¹ ζ is a measurement of whether the two signal leptons lie between the two tagging jets in η , as is preferred by the VBS topology.

2258 **6.5.1 Random grid search algorithm**

2259 The chosen method for optimizing the event selection is a cut-based algorithm known as the Random
 2260 Grid Search (RGS) [111]. Consider a simple case of two variables x and y chosen to differentiate
 2261 signal from background. In order to be considered a signal event, a given event would be required
 2262 to pass a set of selection criteria, called a *cut point*: $c = \{x > x_c, y > y_c\}$. A simple method to
 2263 choose the optimal cut point (i.e. the “best” values of the cuts x_c and y_c) would be to construct an
 2264 $n \times m$ rectangular grid in x and y consisting of points $(x_0, y_0), (x_1, y_1), \dots, (x_n, y_m)$, as Figure 6.3a.
 2265 One can then choose a cut point $c_k = \{x > x_i, y > y_j\}$ that maximizes the signal significance as
 2266 given by a chosen metric. This would be considered a *rectangular grid search*.

2267 While effective in principle, a rectangular grid search comes with two major drawbacks:

- 2268 1. The algorithm scales exponentially as the number of variables to be optimized increases, as
 2269 this is effectively increasing the dimensionality of the grid. In the simple case of a square grid
 2270 with N bins per variable v , the number of cut points to be evaluated grows as N^v .
- 2271 2. Signal and background samples are rarely evenly distributed over the entire grid, resulting
 2272 in many cut points being sub-optimal and evaluating them would be a waste of computing
 2273 resources.

2274 To combat these limitations, the RGS algorithm constructs a grid of cut points directly from
 2275 the signal sample itself. In the two-dimensional example, this means that the variables x_i and y_j
 2276 making up the cut point $c_k = \{x > x_i, y > y_j\}$ take their values directly from a given signal event.
 2277 This has the benefit of creating a *random grid* of cut points that is biased towards regions of high
 2278 signal concentration by construction. This reduces the need for exponentially increasing numbers of
 2279 cut points while ensuring that computing resources are not wasted in regions with few to no signal
 2280 events. An example of a two-dimensional random grid is shown in Figure 6.3b.

2281 Once the random grid of cut points is constructed, the optimal cut point can be chosen using any
 2282 number of metrics, such as signal to background ratio. For the purpose of the $W^\pm W^\pm jj$ upgrade
 2283 study, the optimal cut point is chosen to be the one that maximizes the signal significance Z as
 2284 defined in Equation 6.2 [112]:

$$Z = \sqrt{2 \left[(s+b) \ln \left(\frac{s+b}{b_0} \right) + b_0 - s - b \right] + \frac{(b-b_0)^2}{\sigma_b^2}} \quad (6.2)$$

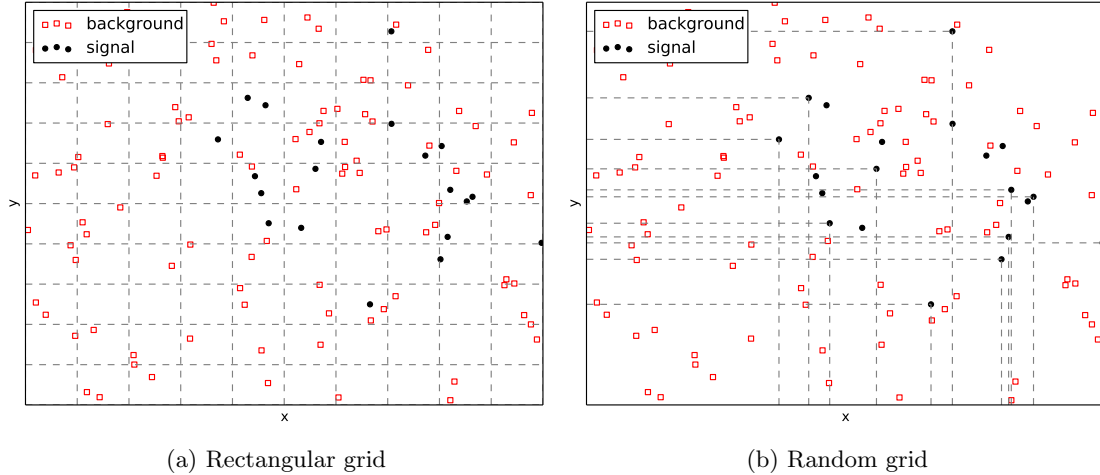


Figure 6.3: A visual representation of a two-dimensional rectangular grid (left) and a random grid (right) in variables x and y . The signal events are the black circles, and the background events. Each intersection of gray dashed lines represents a cut point to be evaluated by the optimization.

2285 where s and b are the number of signal and background events, respectively, σ_b is the total uncertainty
2286 on the background, and b_0 is defined as:

$$b_0 = \frac{1}{2} \left(b - \sigma_b^2 + \sqrt{(b - \sigma_b^2)^2 + 4(s + b)\sigma_b^2} \right) \quad (6.3)$$

2287 In the case where the background is known precisely (i.e. $\sigma_b = 0$), Equation 6.2 simplifies to

$$Z = \sqrt{2 \left(b \left[(1 + s/b) \ln(1 + s/b) - s/b \right] \right)} \quad (6.4)$$

2288 which further reduces to the familiar $Z = s/\sqrt{b}$ for the case when $s \ll b$.

2289 6.5.2 Inputs to the optimization

2290 In order to train the RGS, signal and background samples are prepared from events passing the
2291 event selection outlined in Table 6.3 up through the b -jet veto. The signal sample is chosen to be
2292 the longitudinally polarized $W^\pm W^\pm jj$ EWK events, and the transverse and mixed polarizations
2293 are treated as background along with $W^\pm W^\pm jj$ events from QCD interactions and the traditional
2294 backgrounds listed in Section 6.3. Splitting the inclusive $W^\pm W^\pm jj$ EWK events by polarization
2295 allows the optimization to favor the longitudinally polarized events as much as possible, even though
2296 they both contribute to the EWK signal.

2297 The following variables are chosen for optimization:

- 2298 ● Leading lepton p_T
- 2299 ● Dilepton invariant mass (m_{ll})
- 2300 ● Leading and subleading jet p_T
- 2301 ● Dijet invariant mass (m_{jj})
- 2302 ● Lepton-jet centrality (ζ)

2303 Subleading lepton p_T is omitted as it is desirable to keep the cut value as low as possible due
 2304 to its sensitivity to the longitudinal polarization (as discussed in Section 6.1.1); despite this, the
 2305 leading lepton p_T is still allowed to be optimized as it can have strong background rejection power.
 2306 Additionally, the dijet separation $\Delta\eta_{jj}$ was included in early studies of the optimization, however it
 2307 was dropped due to the cut value being motivated by well-studied differences between EWK- and
 2308 QCD-produced $W^\pm W^\pm jj$ events (as in Figure 5.6b).

2309 Two additional constraints were imposed when selecting the optimal cut point:

- 2310 1. At least 1000 signal events must survive in order to prevent the optimization from being too
 2311 aggressive and unnecessarily reducing signal statistics.
- 2312 2. The dijet invariant mass may only vary within a 50 GeV range of the default value (from
 2313 450–550 GeV) due to the cut being physically motivated by the VBS event topology described
 2314 in Section 5.0.2.

2315 Lastly, the signal significance is calculated without taking into account the uncertainty of the
 2316 background using Equation 6.4. This is due to the fact that the statistical uncertainties of the fake
 2317 electron and charge misidentification backgrounds are quite large, owing to poor MC statistics in a
 2318 few of the samples. If Equation 6.2 were used instead, the optimization would cut unreasonably
 2319 hard against these backgrounds. Since Monte Carlo statistics is not expected to be a limiting factor
 2320 when this analysis is performed at the HL-LHC, it is more realistic to simply ignore these large
 2321 statistical uncertainties for the purpose of the optimization.

2322 6.5.3 Results of the optimization

2323 Ultimately, the random grid is constructed from over 38,000 LL-polarized $W^\pm W^\pm jj$ events in the
 2324 six variables listed above. After applying the constraints, the optimal cut point reduces the total
 2325 background from 9900 to 2310 while reducing the signal from 3489 to 2958. This corresponds to

2326 an increase in signal significance from $Z = 33.26$ to $Z = 52.63$ as calculated by Equation 6.4. The
 2327 updates to the event selection are listed in Table 6.4.

2328 The large reduction in the background is primarily a result of increasing the leading and sub-
 2329 leading jet p_T from 30 GeV to 90 GeV and 45 GeV, respectively. As can be seen in Figure 6.4,
 2330 this increase removes a significant portion of the backgrounds from jets faking electrons and charge
 2331 mis-ID. Additionally, the loosening of the lepton-jet centrality cut ζ allows more signal events to
 2332 survive the event selection (see Figure 6.5). Other changes to the event selection are minor and
 2333 do not individually have a large impact on the signal or background yields; similar distributions of
 2334 these variables are shown in Appendix B.2.

2335 The full event yields after optimization as well as the cross section measurement are detailed
 2336 alongside those using the default selection in Section 6.6.

Selection requirement	Selection value
Lepton kinematics	$p_T > 28$ GeV (leading lepton only)
Jet kinematics	$p_T > 90$ GeV (leading jet) $p_T > 45$ GeV (subleading jet)
Dilepton mass	$m_{ll} > 28$ GeV
Dijet mass	$m_{jj} > 520$ GeV
Lepton-jet centrality	$\zeta > -0.5$

Table 6.4: Updates to the $W^\pm W^\pm jj$ event selection criteria after optimization. Cuts not listed remain unchanged from the default selection in Table 6.3.

2337 6.6 Results

2338 6.6.1 Event yields

2339 After applying the full event selection, the analysis is broken down into four channels based off of
 2340 the flavor of the signal leptons: $\mu\mu$, ee , μe , and $e\mu$. The full signal and background event yields are
 2341 shown in Table 6.5 for each channel separately and combined using the default event selection. 3489
 2342 EWK $W^\pm W^\pm jj$ events are expected compared to 9900 background events. The dominant sources
 2343 of background are jets faking electrons followed by charge misidentification and diboson processes.
 2344 Triboson events, QCD $W^\pm W^\pm jj$, and other non-prompt sources make up approximately 5% of the
 2345 total background combined.

2346 The event yields for the optimized selection detailed in Section 6.5.3 are listed in Table 6.6. After
 2347 optimization, 2958 signal events and just 2310 background events are expected. Diboson events are
 2348 now the primary source of background, as the optimization greatly reduces the fake and charge

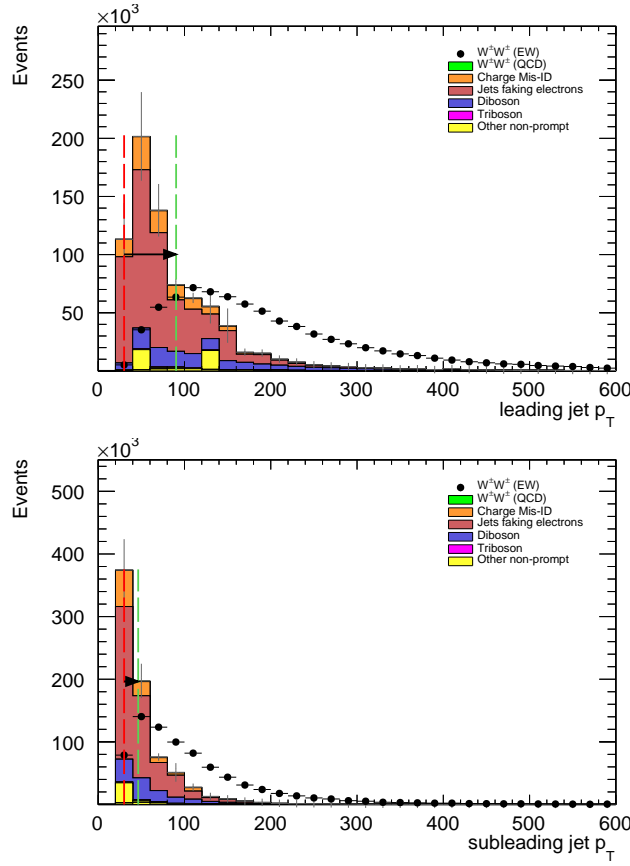


Figure 6.4: Leading (top) and subleading (bottom) jet p_T distributions. The default and optimized cuts are represented by the red and green dashed lines, respectively. The $W^\pm W^\pm jj$ EWK signal (black points) is normalized to the same area as the sum of the backgrounds (colored histogram).

	All channels	$\mu\mu$	ee	μe	$e\mu$
$W^\pm W^\pm jj$ (QCD)	206.4	91.1	22.8	38.4	54.1
Charge Misidentification	2300	0.0	2100	90	160
Jets faking electrons	5000	0.0	3400	1200	340
$WZ + ZZ$	2040	500	438	423	680
Tribosons	115	47	15.4	21.6	31.2
Other non-prompt	210	110	20	60	27
Total Background	9900	750	6000	1900	1290
Signal $W^\pm W^\pm jj$ (EWK)	3489	1435	432	679	944

Table 6.5: Signal and background event yields using the default event selection for an integrated luminosity of $\mathcal{L} = 3000 \text{ fb}^{-1}$. Events containing a fake or charge-flipped electron are removed from their respective sources and combined into a single entry each.

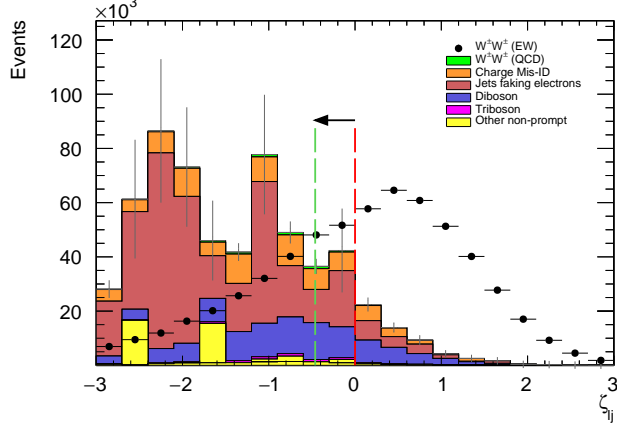


Figure 6.5: Lepton-jet centrality distribution. The default and optimized cuts are represented by the red and green dashed lines, respectively. The $W^\pm W^\pm jj$ EWK signal (black points) is normalized to the same area as the sum of the backgrounds (colored histogram).

mis-ID contributions. As discussed earlier, the increase in the leading and subleading jet p_T cuts as well as the loosening of the centrality cut are most responsible for the changes in the signal and background yields; distributions of these quantities using the default and the optimized event selections can be found in Figures 6.6, 6.7, and 6.8, respectively.

	All channels	$\mu\mu$	ee	μe	$e\mu$
$W^\pm W^\pm jj$ (QCD)	168.7	74.6	19.7	32.2	42.2
Charge Misidentification	200	0.0	11	30	160
Jets faking electrons	460	0.0	130	260	70
$WZ + ZZ$	1286	322	289	271	404
Tribosons	76	30.1	9.6	15.1	21.6
Other non-prompt	120	29	16.6	50	19
Total Background	2310	455	480	660	710
Signal $W^\pm W^\pm jj$ (EWK)	2958	1228	380	589	761

Table 6.6: Signal and background event yields using the optimized event selection for an integrated luminosity of $\mathcal{L} = 3000 \text{ fb}^{-1}$. Events containing a fake or charge-flipped electron are removed from their respective sources and combined into a single entry each.

It is important to note, however, that the MC sample used to estimate $Z+jets$ events suffers from poor statistics which results in large per-event weights once scaled to $\mathcal{L} = 3000 \text{ fb}^{-1}$. This sample contributes heavily to the fake and charge misidentification backgrounds, and a handful of these events being cut out by the optimization is largely responsible for the dramatic reduction of the corresponding backgrounds. As a result, the optimized results presented here are likely overly optimistic. However, given proper MC statistics, it is still expected that this optimization will

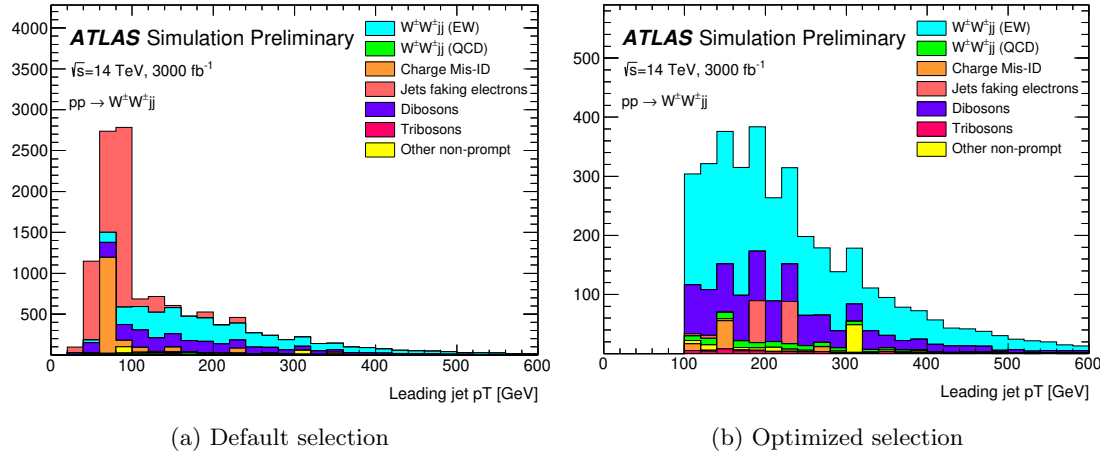


Figure 6.6: p_T distributions for the leading jet using the default (left) and optimized (right) event selections for all channels combined.

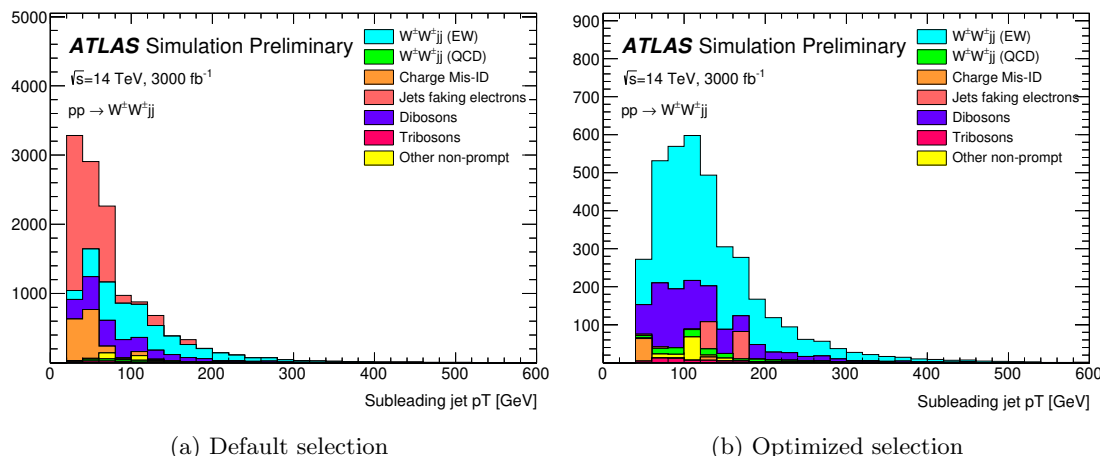


Figure 6.7: p_T distributions for the subleading jet using the default (left) and optimized (right) event selections for all channels combined.

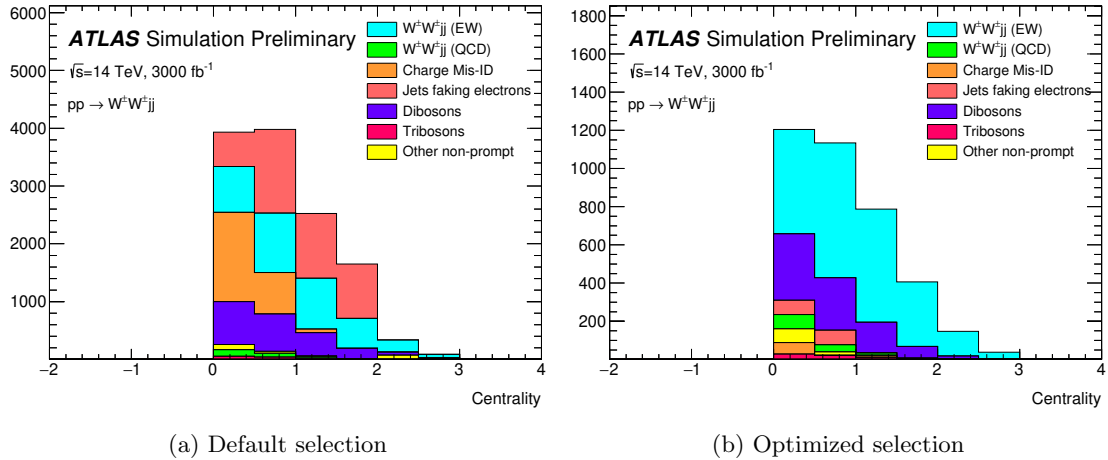


Figure 6.8: p_T distributions for lepton-jet centrality ζ using the default (left) and optimized (right) event selections for all channels combined.

2359 outperform the default selection.

2360 6.6.2 Uncertainties

2361 The uncertainties considered for the analysis are summarized in Table 6.7. Values for experimental
 2362 systematics on the trigger efficiency, lepton and jet reconstruction, and flavor tagging are taken
 2363 directly from the 13 TeV analysis [68]. The rate uncertainties for the background processes are
 2364 halved from the 13 TeV values according to ATLAS recommendations. The uncertainty on the fake
 2365 electron estimation is also halved from the 13 TeV analysis. Finally, a conservative estimate of the
 2366 uncertainty on the charge flip background is used as the electron charge mis-ID rate due to material
 2367 interactions is difficult to predict at this stage.

2368 6.6.3 Cross section measurement

2369 The cross section is calculated using the same method as in the 13 TeV analysis, detailed in Sec-
 2370 tion 5.4. Unlike the previous analysis, however, eight lepton channels are used here instead of six.
 2371 The μe and $e\mu$ channels remain separated in addition to the $\mu\mu$ and ee channels, and each lepton
 2372 flavor channel is further split by charge (i.e. $\mu\mu \rightarrow \mu^+\mu^+ + \mu^-\mu^-$), as this increases the sensitivity
 2373 of the analysis. Each channel's m_{jj} distribution is combined in a profile likelihood fit to extract
 2374 the EWK $W^\pm W^\pm jj$ production cross section. Using the default event selection, the expected cross

Source	Uncertainty (%)
$W^\pm W^\pm jj$ (EWK)	3
Luminosity	1
Trigger efficiency	0.5
Lepton reconstruction and identification	1.8
Jets	2.3
Flavor tagging	1.8
Jets faking electrons	20
Charge misidentification	25
$W^\pm W^\pm jj$ (QCD)	20
Top	15
Diboson	10
Triboson	15

Table 6.7: Summary of estimated experimental and rate uncertainties.

2375 section calculated to be:

$$\sigma_{W^\pm W^\pm jj}^{\text{expected}} = 16.89 \pm 0.36 \text{ (stat)} \pm 0.53 \text{ (theory)} \pm 0.84 \text{ (syst)} \text{ fb} \quad (6.5)$$

2376 and with the optimized event selection:

$$\sigma_{W^\pm W^\pm jj}^{\text{expected}} = 16.94 \pm 0.36 \text{ (stat)} \pm 0.53 \text{ (theory)} \pm 0.78 \text{ (syst)} \text{ fb} \quad (6.6)$$

2377 The optimized selection should not change the measured value of the cross section, and indeed both
 2378 are consistent with within uncertainties. The systematic uncertainty is reduced by approximately
 2379 7% with the optimized selection. The total uncertainty on the cross section measurement is approx-
 2380 imately 6%, compared to approximately 20% on the measured fiducial cross section of the 13 TeV
 2381 analysis reported in Equation 5.30.

2382 Projections of each uncertainty type and the total uncertainty on the cross section as a function of
 2383 integrated luminosity are shown in Figure 6.9. The predictions are made by scaling the event yields
 2384 by different luminosity values and re-running the fitting procedure. As the integrated luminosity
 2385 increases past $\mathcal{L} > 3000 \text{ fb}^{-1}$, the statistical uncertainty continues to reduce; however, the total
 2386 uncertainty becomes limited by the systematics. Additionally, the total uncertainty is expected to
 2387 reduce by less than a percent as the integrated luminosity increases past the planned 3000 fb^{-1} .

2388 6.6.4 Longitudinal scattering significance

2389 The longitudinal scattering significance is extracted in much the same way as the cross section, this
 2390 time using a binned likelihood fit on the $|\Delta\phi_{jj}|$ distribution. In order to increase sensitivity, the

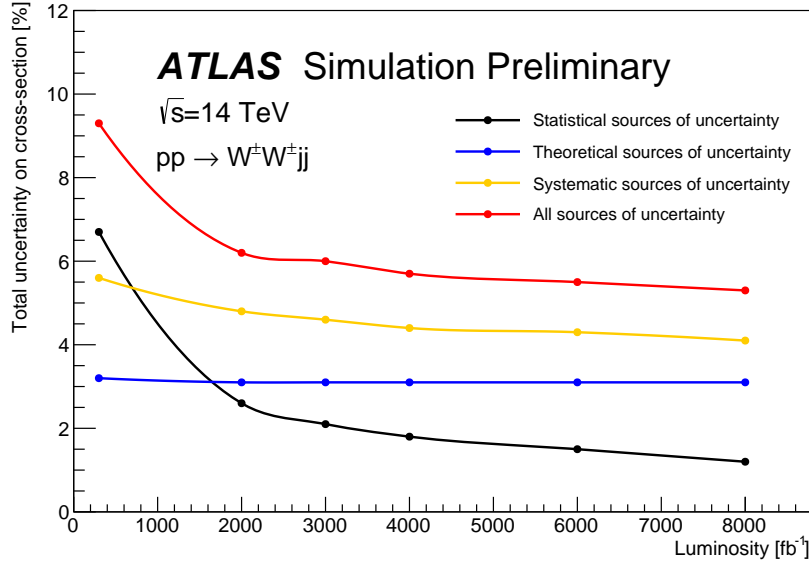


Figure 6.9: Projections of the statistical (black), theoretical (blue), systematic (yellow), and total (red) uncertainties on the measured cross section as a function of integrated luminosity using the optimized event selection.

2391 $|\Delta\phi_{jj}|$ distribution is split into two bins in m_{jj} , and an additional cut on the pseudorapidity of the
 2392 subleading lepton is applied ($|\eta| < 2.5$) to reduce background contributions from fake electrons and
 2393 charge flip. The $|\Delta\phi_{jj}|$ distributions used in the fit are shown in Figure 6.10. Due to limited statistics
 2394 in the LL events, the four lepton flavor channels are not split by charge. The expected significance
 2395 of the $W_L^\pm W_L^\pm jj$ process is 1.8σ with a precision of 47% on the measurement. Projections of the
 2396 expected significance as a function of integrated luminosity is shown in Figure 6.11.

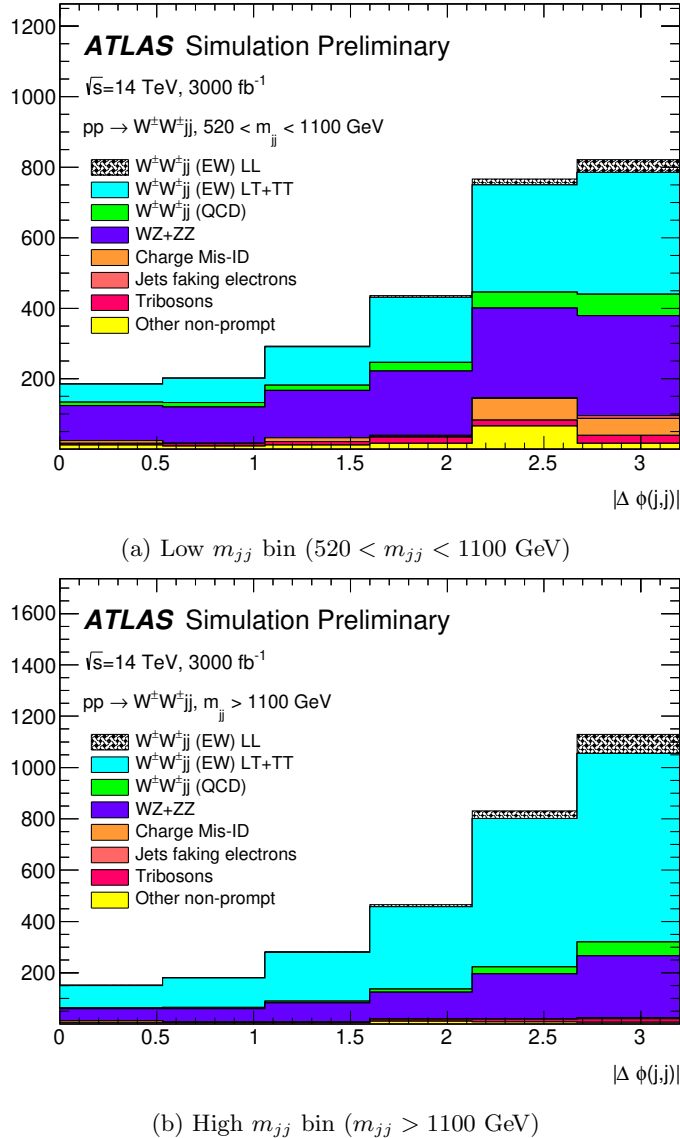


Figure 6.10: Dijet azimuthal separation ($|\Delta\phi_{jj}|$) for the low m_{jj} region ($520 < m_{jj} < 1100$ GeV, top) and the high m_{jj} region ($m_{jj} > 1100$ GeV, bottom). The purely longitudinal (LL, gray) is plotted separately from the mixed and transverse (LT+TT, cyan) polarizations.

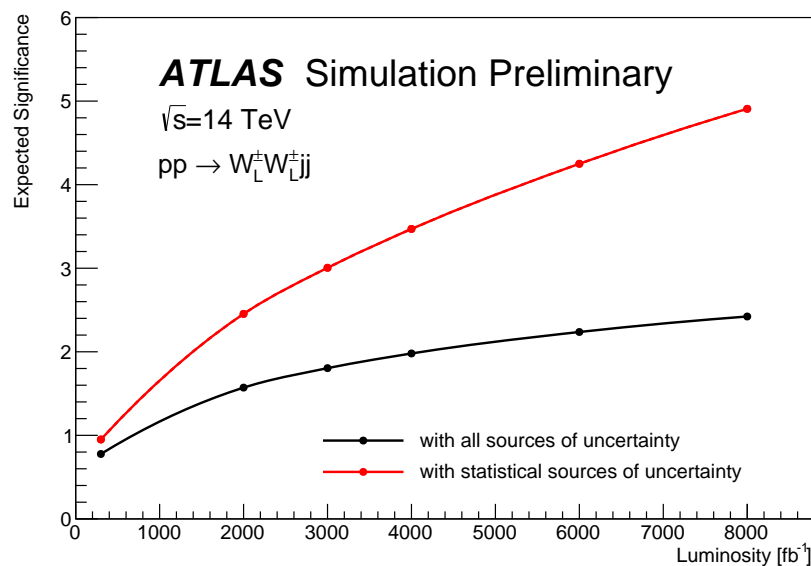


Figure 6.11: Projections of the expected longitudinal scattering significance as a function of integrated luminosity when considering all sources of uncertainties (black) or only statistical uncertainties (red).

2397

CHAPTER 7

2398

Conclusion

2399 Here's where you wrap it up.

2400

APPENDIX A

2401

2402

Additional material on $W^\pm W^\pm jj$ measurement at $\sqrt{s} = 13$ TeV

2403

A.1 Impact of experimental uncertainty on MC background estimations

Tables A.1-A.6 contain the impact of experimental systematic uncertainties for the remaining backgrounds estimated from MC simulation. The $W^\pm W^\pm jj$ EWK signal and WZ background systematics are listed in the main body of the document, in Tables 5.21 and 5.22, respectively. While the percentage of the contributions for some systematics appear large, the size of these backgrounds are quite small compared to the total background.

$W^\pm W^\pm jj$ QCD	ee % Yield	$e\mu$ % Yield	$\mu\mu$ % Yield
Jet-related Uncertainties	3.41	3.04	2.85
b-tagging efficiency	2.56	2.48	2.48
Pile-up	4.99	0.45	0.33
Trigger efficiency	0.02	0.08	0.41
Lepton reconstruction/ID	1.62	1.19	1.89
MET reconstruction	0.41	0.22	0.34

Table A.1: Impact of experimental uncertainties for the $W^\pm W^\pm jj$ QCD processes in all channels.

Triboson	ee % Yield	$e\mu$ % Yield	$\mu\mu$ % Yield
Jet-related Uncertainties	13.09	13.39	16.85
b-tagging efficiency	2.96	3.77	4.95
Pile-up	19.37	24.66	6.87
Trigger efficiency	0.02	0.07	0.47
Lepton reconstruction/ID	1.66	1.27	2.48
MET reconstruction	0.00	0.46	0.00

Table A.2: Impact of experimental uncertainties for triboson process in all channels.

$t\bar{t}V$	ee % Yield	$e\mu$ % Yield	$\mu\mu$ % Yield
Jet-related Uncertainties	17.65	11.97	14.27
b-tagging efficiency	15.02	9.04	13.83
Pile-up	8.73	10.69	4.18
Trigger efficiency	0.03	0.08	0.39
Lepton reconstruction/ID	2.57	3.27	2.66
MET reconstruction	1.75	4.16	1.62

Table A.3: Impact of experimental uncertainties for $t\bar{t}V$ processes in all channels.

$W\gamma$	ee % Yield	$e\mu$ % Yield	$\mu\mu$ % Yield
Jet-related Uncertainties	7.05	33.36	—
b-tagging efficiency	1.97	2.94	—
Pile-up	4.11	14.17	—
Trigger efficiency	0.01	0.14	—
Lepton reconstruction/ID	1.40	1.13	—
MET reconstruction	0.00	0.00	—

Table A.4: Impact of experimental uncertainties for the $W\gamma$ process in all channels.

$Z\gamma$	ee % Yield	$e\mu$ % Yield	$\mu\mu$ % Yield
Jet-related Uncertainties	16.22	370.44	—
b-tagging efficiency	1.08	3.10	—
Pile-up	12.57	11.51	—
Trigger efficiency	0.02	0.07	—
Lepton reconstruction/ID	1.26	22.01	—
MET reconstruction	0.00	0.00	—

Table A.5: Impact of experimental uncertainties for the $Z\gamma$ process in all channels.

ZZ	ee % Yield	$e\mu$ % Yield	$\mu\mu$ % Yield
Jet-related Uncertainties	15.71	15.76	35.18
b-tagging efficiency	2.23	2.35	2.89
Pile-up	1.22	3.20	4.58
Trigger efficiency	0.03	0.10	0.36
Lepton reconstruction/ID	3.59	3.10	5.70
MET reconstruction	4.84	3.26	3.24

Table A.6: Impact of experimental uncertainties for the ZZ process in all channels.

2409 **A.2 Additional signal region plots**

2410

APPENDIX B

2411

2412

Additional material on $W^\pm W^\pm jj$ prospects at the HL-LHC

2413

B.1 Truth isolation

As mentioned in Section 6.3.1, the size of the background contribution from top processes are much larger than expected when no isolation is applied. The event yields using an earlier version of the event selection with no truth-based isolation requirement are listed in Table B.1. Here, top events make up nearly 90% of the total background, and the contributions from fake and charge-flipped electrons are also large. The event yields using the same event selection with the truth-based isolation included are shown in Figure B.2. When comparing the two tables, the considerable reduction in the top background can be clearly seen.

yields by type	all channels	$\mu\mu$	ee	μe	$e\mu$
signal	4011	1583.2	531.7	793.1	1103.1
ww qcd	252.6	105.8	30.4	48	68.4
charge flip	2528.4	0.0	2075.4	255.1	197.8
fakes	7135.4	0.0	4675.1	1904.3	555.9
diboson	2370.4	581.2	491.8	517.9	779.6
triboson	125.5	49.1	17.8	24.6	34.1
top	90150.5	26618	15301.6	25277.9	22953.1
z+jets	241.2	0.0	0.0	0.0	241.2
w+jets	31.4	3.9	7.6	13.2	6.7
total bkg	102803.9	27354	22592	28027.8	24830.1
signal	4011	1583.2	531.7	793.1	1103.1

Table B.1: Event yields prior to applying any form of truth-based isolation criteria.

2420

2421

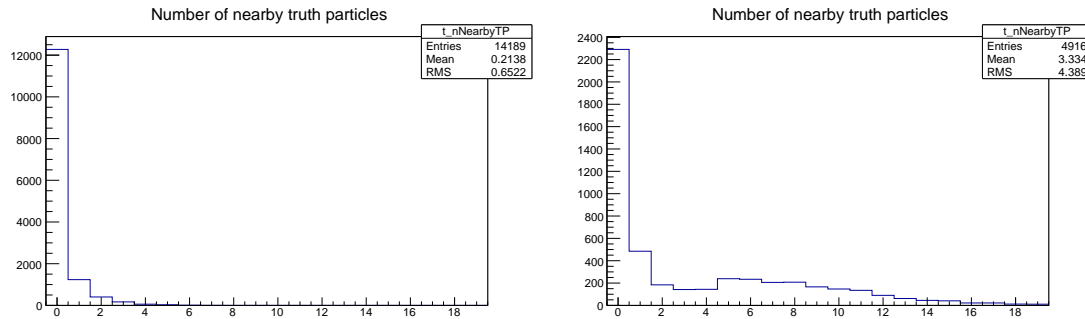
TODO: Add tables for tight vs loose working point, information on the necessity of TRUTH1++

yields by type	all channels	$\mu\mu$	ee	μe	$e\mu$
signal	3470.5	1427.3	428.8	675.8	938.7
ww qcd	205.8	90.8	22.7	38.3	54
charge flip	2398.3	0.0	2104.6	95.8	197.9
fakes	4309.7	0.0	3390.6	750.8	168.3
diboson	1552.4	311.3	355.6	346.8	538.7
triboson	115	46.8	15.4	21.6	31.2
top	156.9	42.3	14.8	76.6	23.3
$z+jets$	0.0	0.0	0.0	0.0	0.0
$w+jets$	0.3	0.0	0.0	0.3	0.0
total bkg	8738.1	491.3	5903.7	1329.8	1013.4
signal	3470.5	1427.3	428.8	675.8	938.7

Table B.2: Event yields after applying a test version of the truth-based isolation.

2422 B.1.1 TRUTH1++ derivations

2423 The ATLAS standard TRUTH1 derivations used for this analysis contain a slimmed truth particle
 2424 container in order to reduce the file size. As a result, many of the truth particles that would be
 2425 included in the isolation variables are missing, and the truth-based isolation will not accurately
 2426 model the reconstruction-level isolation variables. In order to recover the performance of the truth-
 2427 based isolation in the top MC samples (where it is most needed), a custom derivation was produced
 2428 privately that duplicated the default TRUTH1 data structure but includes the full truth particle
 2429 record. The reduced size of the truth particle information in the TRUTH1 derivation compared to the
 2430 TRUTH1++ derivation is shown in Figure B.1.

Figure B.1: Number of truth particles within $\Delta R < 0.4$ of a selected muon or electron using the ATLAS standard TRUTH1 (left) and the custom TRUTH1++ (right) derivations in $t\bar{t}$ simulation. The complete truth record is stored in the TRUTH1++ derivation, and this is best seen in the first bin, where the lepton has no nearby truth particles.

2431 **B.1.2 Check of truth-based isolation**

2432 Since the isolation variables are constructed from truth particles, there is an expectation that the
 2433 efficiency of the isolation selection will be higher than what would be seen in the full simulation.
 2434 In order to test this, a truth-level 13 TeV $t\bar{t}$ MC sample was run through a selection altered to
 2435 mimic the 13 TeV $W^\pm W^\pm jj$ measurement as closely as possible. The results were compared to the
 2436 $t\bar{t}$ background in the 13 TeV analysis extrapolated to 14 TeV and 3000 fb^{-1} , and the truth-based
 2437 isolation reduces the expected events by a factor of approximately 4. However, the statistics in the
 2438 13 TeV truth-level sample are low, and it is therefore difficult to measure precisely how much the
 2439 truth-based isolation overperforms.

2440 **B.1.3 Loose isolation working point**

2441 As another check on the truth-based isolation, a second isolation working point was constructed
 2442 to match the official ATLAS Fixed Cut Loose isolation working point. The definition of this loose
 2443 isolation are found in Table B.3.

2444 The primary impact of loosening the isolation is a substantial increase in the non-prompt back-
 2445 round from top processes, and a moderate increase in the charge mis-ID and fake backgrounds.
 2446 Backgrounds from prompt leptons only did not see major changes. As a result, the tight working
 2447 point is chosen for the analysis. The event yields by sample and by background type using the
 2448 loose working point are in Table B.4, and Table B.5 has the numbers using the tight working point
 2449 (defined in Table 6.2) for comparison.

	Electron Isolation	Muon Isolation
Track-based isolation cone size	$\Delta R < 0.2$	$\Delta R < 0.3$
Track-based isolation requirement	$\sum p_T/p_T^e < 0.15$	$\sum p_T/p_T^\mu < 0.15$
Calorimeter-based isolation cone size	$\Delta R < 0.2$	$\Delta R < 0.2$
Calorimeter-based isolation requirement	$\sum E_T/p_T^e < 0.2$	$\sum E_T/p_T^\mu < 0.3$

Table B.3: Electron and muon isolation requirements for the loose working point.

run number	all channels			mm			ee			me			em		
	events	stat	sys	events	stat	sys	events	stat	sys	events	stat	sys	events	stat	sys
signal	3783.21	22.08	0.00	1524.99	15.00	0.00	484.74	7.01	0.00	740.76	9.01	0.00	1032.72	11.50	0.00
ww qcd	223.95	3.54	44.79	97.17	2.51	19.43	25.51	1.03	5.10	42.23	1.40	8.45	59.04	1.80	11.81
charge flip	3025.40	1276.74	0.00	0.00	0.00	0.00	2615.30	1267.89	0.00	197.20	87.94	0.00	212.90	121.63	0.00
fakes	5315.55	1775.87	0.00	0.00	0.00	0.00	3524.24	1694.39	0.00	1356.74	450.60	0.00	434.57	282.33	0.00
diboson	2195.61	38.10	219.58	548.72	18.54	54.87	451.27	18.29	45.14	470.61	15.71	47.07	725.01	22.95	72.50
triboson	117.43	5.90	17.62	47.55	4.32	7.13	15.83	1.94	2.37	22.11	2.18	3.32	31.94	2.76	4.80
top	554.63	218.75	83.21	229.26	135.53	34.40	61.15	38.23	9.18	232.30	167.28	34.85	31.92	6.43	4.78
z+jets	0.00	0.00	0.00	0.00	0.00	0.00	0.00	0.00	0.00	0.00	0.00	0.00	0.00	0.00	0.00
w+jets	1.21	0.87	0.00	0.00	0.00	0.00	0.00	0.00	0.00	0.00	0.00	0.00	0.00	0.02	0.00
total bkg	11433.78	2198.44	239.70	922.70	136.88	67.99	6693.30	2116.67	46.41	2322.38	488.89	59.27	1495.40	308.36	73.77
signal	3783.21	22.08	0.00	1524.99	15.00	0.00	484.74	7.01	0.00	740.76	9.01	0.00	1032.72	11.50	0.00

Table B.4: Event yields broken down by sample and by background type using the loose isolation workingpoint. Events containing a fake or charge-flipped electron are removed from their respective sample and added to the ‘fakes’ and ‘charge flip’ rows, respectively. Errors include statistical uncertainty and estimated systematic rate uncertainty based on the background process.

run number	all channels			mm			ee			me			em		
	events	stat	sys	events	stat	sys	events	stat	sys	events	stat	sys	events	stat	sys
signal	3489.49	21.23	0.00	1434.85	14.55	0.00	431.75	6.61	0.00	679.09	8.63	0.00	943.8	11.00	0.00
ww qcd	206.42	3.41	41.28	91.12	2.43	18.22	22.84	0.98	4.57	38.37	1.34	7.67	54.09	1.72	10.82
charge flip	2335.73	1163.47	0.00	0.00	0.00	0.00	2087.78	1159.5	0.00	90.37	33.32	0.00	157.58	90.02	0.00
fakes	4979.27	1756.47	0.00	0.00	0.00	0.00	3406.20	1705.03	0.00	1230.80	362.15	0.00	342.27	216.54	0.00
diboson	2039.94	36.93	204.00	499.69	18.04	49.97	437.60	14.12	43.76	422.90	14.18	42.29	679.75	25.25	67.98
triboson	115.03	5.87	17.29	46.84	4.31	7.03	15.40	1.94	2.32	21.55	2.17	3.24	31.24	2.74	4.70
top	211.74	84.14	31.76	107.96	71.12	16.20	19.58	3.76	2.93	57.21	44.47	8.58	26.99	5.40	4.05
z+jets	0.00	0.00	0.00	0.00	0.00	0.00	0.00	0.00	0.00	0.00	0.00	0.00	0.00	0.00	0.00
w+jets	0.30	0.28	0.00	0.00	0.00	0.00	0.00	0.00	0.00	0.28	0.28	0.00	0.02	0.02	0.00
total bkg	9888.43	2108.87	211.25	745.61	73.54	56.04	5898.40	2061.99	44.16	1861.48	366.67	43.95	1291.94	235.95	69.11
signal	3489.49	21.23	0.00	1434.85	14.55	0.00	431.75	6.61	0.00	679.09	8.63	0.00	943.80	11.00	0.00

Table B.5: Event yields broken down by background type using the tight isolation workingpoint. Events containing a fake or charge-flipped electron are removed from their respective sample and added to the “fakes” and “charge flip” rows, respectively. Errors include statistical uncertainty and estimated systematic rate uncertainty based on the background process.

2450 B.2 Plots of other optimization variables

2451 Plots of the remaining optimization variables not shown in Section 6.5.3 are presented here for
 2452 reference. Figures B.2, B.3, and B.4 compare signal and background distributions for the default
 2453 and optimized cuts. None of these cuts change by much in the optimized selection and their impacts
 2454 on the overall event selection is minimal.

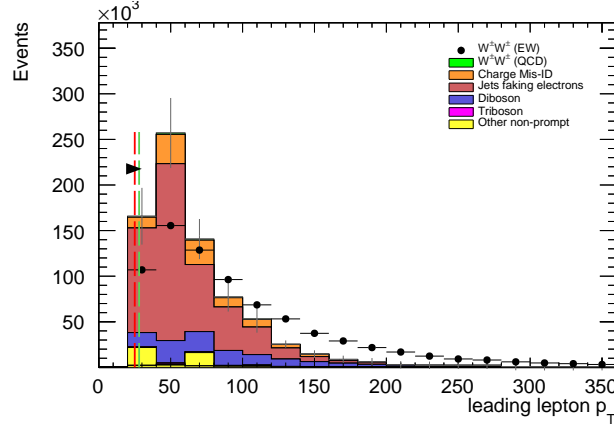


Figure B.2: Leading lepton p_T distribution. The default and optimized cuts are represented by the red and green dashed lines, respectively. The $W^\pm W^\pm jj$ EWK signal (black points) is normalized to the same area as the sum of the backgrounds (colored histogram).

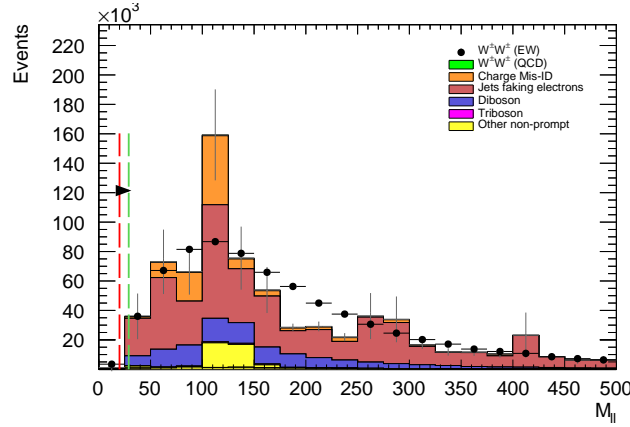


Figure B.3: Dilepton invariant mass distribution. The default and optimized cuts are represented by the red and green dashed lines, respectively. The $W^\pm W^\pm jj$ EWK signal (black points) is normalized to the same area as the sum of the backgrounds (colored histogram).

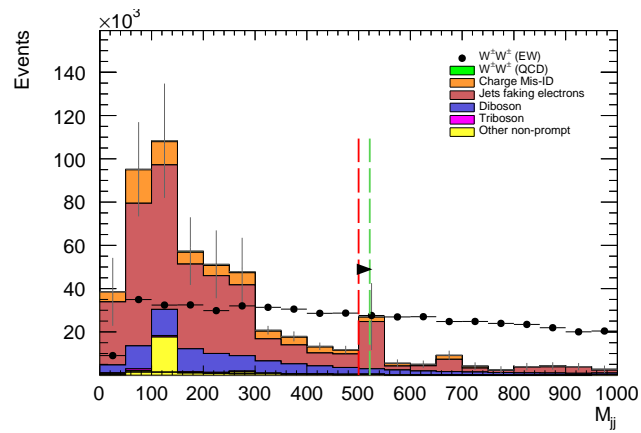


Figure B.4: Dijet invariant mass distribution. The default and optimized cuts are represented by the red and green dashed lines, respectively. The $W^\pm W^\pm jj$ EWK signal (black points) is normalized to the same area as the sum of the backgrounds (colored histogram).

Bibliography

- 2456 [1] ATLAS Collaboration Collaboration, M. Marjanovic, *ATLAS Tile calorimeter calibration*
 2457 *and monitoring systems*, Tech. Rep. arXiv:1806.09156, Jun, 2018.
 2458 <http://cds.cern.ch/record/2629424>. 8 pages, 21 figures, IEEE Real Time 2018
 2459 proceedings. ([document](#)), 3.7
- 2460 [2] ATLAS Collaboration, M. Aaboud et al., *Measurement of the $W^\pm Z$ boson pair-production*
 2461 *cross section in pp collisions at $\sqrt{s} = 13$ TeV with the ATLAS Detector*, *Phys. Lett. B* **762**
 2462 (2016) 1–22, arXiv:1606.04017 [hep-ex]. ([document](#))
- 2463 [3] ATLAS Collaboration, *Summary plots from the ATLAS Standard Model physics group*,
 2464 February, 2019.
<https://atlas.web.cern.ch/Atlas/GROUPS/PHYSICS/CombinedSummaryPlots/SM/>. 2.1
- 2466 [4] S. Weinberg, *The Quantum Theory of Fields, Volume 1: Foundations*. Cambridge University
 2467 Press, 1995. 2.1
- 2468 [5] M. E. Peskin and D. V. Schroeder, *An Introduction to Quantum Field Theory*.
 2469 Addison-Wesley, 1995. 2.1
- 2470 [6] R. P. Feynman, *Mathematical formulation of the quantum theory of electromagnetic*
 2471 *interaction*, *Phys. Rev.* **80** (1950) 440–457. 2.1
- 2472 [7] M. Y. Han and Y. Nambu, *Three-triplet model with double SU(3) symmetry*, *Phys. Rev.* **139**
 2473 (1965) B1006–B1010. 2.1
- 2474 [8] D. J. Gross and F. Wilczek, *Asymptotically Free Gauge Theories - I*, *Phys. Rev. D* **8** (1973)
 2475 3633–3652. 2.1
- 2476 [9] D. J. Gross and F. Wilczek, *ASYMPTOTICALLY FREE GAUGE THEORIES. 2.*, *Phys.*
 2477 *Rev. D* **9** (1974) 980–993. 2.1
- 2478 [10] H. D. Politzer, *Reliable Perturbative Results for Strong Interactions?*, *Phys. Rev. Lett.* **30**
 2479 (1973) 1346–1349. [274(1973)]. 2.1
- 2480 [11] A. Salam and J. C. Ward, *Weak and Electromagnetic Interactions*, *Nuovo Cimento* **11**
 2481 (1959) 568–577. 2.1

- 2482 [12] S. L. Glashow, *The Renormalizability of Vector Meson Interactions*, *Nucl. Phys.* **10** (1959)
2483 107–117. 2.1
- 2484 [13] ALEPH, DELPHI, L3, OPAL, SLD, LEP Electroweak Working Group, SLD Electroweak
2485 Group, SLD Heavy Flavour Group Collaboration, S. Schael et al., *Precision electroweak*
2486 *measurements on the Z resonance*, *Phys. Rept.* **427** (2006) 257–454, [arXiv:hep-ex/0509008](#)
2487 [*hep-ex*]. 2.1
- 2488 [14] F. Englert and R. Brout, *Broken symmetry and the mass of gauge vector mesons*, *Phys. Rev.*
2489 *Lett.* **13** (1964) 321–323. 2.1
- 2490 [15] P. W. Higgs, *Broken symmetries, massless particles and gauge fields*, *Physics Letters* **12**
2491 (1964) 132–133. 2.1
- 2492 [16] P. W. Higgs, *Broken symmetries and the masses of gauge bosons*, *Phys. Rev. Lett.* **13** (1964)
2493 508–509. 2.1
- 2494 [17] ATLAS Collaboration, *Observation of a new particle in the search for the Standard Model*
2495 *Higgs boson with the ATLAS detector at the LHC*, *Phys. Lett. B* **716** (2012) 1,
2496 [arXiv:1207.7214](#) [*hep-ex*]. 2.1, 5.0.1
- 2497 [18] CMS Collaboration, *Observation of a new boson at a mass of 125 GeV with the CMS*
2498 *experiment at the LHC*, *Phys. Lett. B* **716** (2012) 30, [arXiv:1207.7235](#) [*hep-ex*]. 2.1, 5.0.1
- 2499 [19] UA1 Collaboration, G. Arnison et al., *Experimental Observation of Isolated Large Transverse*
2500 *Energy Electrons with Associated Missing Energy at $s^{**}(1/2) = 540\text{-GeV}$* , *Phys. Lett.* **B122**
2501 (1983) 103–116. [,611(1983)]. 2.2
- 2502 [20] UA1 Collaboration, G. Arnison et al., *Experimental Observation of Lepton Pairs of Invariant*
2503 *Mass Around $95\text{-GeV}/c^{**2}$ at the CERN SPS Collider*, *Phys. Lett.* **B126** (1983) 398–410.
2504 [,7.55(1983)]. 2.2
- 2505 [21] Particle Data Group Collaboration, K. A. Olive et al., *Review of Particle Physics*, *Chin.*
2506 *Phys.* **C38** (2014) 090001. 2.2, 2.2
- 2507 [22] D. R. Green, P. Meade, and M.-A. Pleier, *Multiboson interactions at the LHC*, *Rev. Mod.*
2508 *Phys.* **89** (2017) no. 3, 035008, [arXiv:1610.07572](#) [*hep-ex*]. 2.3
- 2509 [23] H.-J. He and W. B. Kilgore, *The Equivalence theorem and its radiative correction - free*
2510 *formulation for all $R(xi)$ gauges*, *Phys. Rev.* **D55** (1997) 1515–1532, [arXiv:hep-ph/9609326](#)
2511 [*hep-ph*]. 2.3
- 2512 [24] B. W. Lee, C. Quigg, and H. B. Thacker, *The Strength of Weak Interactions at Very*
2513 *High-Energies and the Higgs Boson Mass*, *Phys. Rev. Lett.* **38** (1977) 883–885. 2.3
- 2514 [25] S. D. Rindani, *Strong gauge boson scattering at the LHC*, in *Physics at the Large Hadron*
2515 *Collider*, A. Datta, B. Mukhopadhyaya, A. Raychaudhuri, A. K. Gupta, C. L. Khetrapal,
2516 T. Padmanabhan, and M. Vijayan, eds., pp. 145–155. 2009. [arXiv:0910.5068](#) [*hep-ph*]. 2.3,
2517 2.3
- 2518 [26] V. D. Barger, K.-m. Cheung, T. Han, and R. J. N. Phillips, *Strong W^+W^+ scattering signals*
2519 *at pp supercolliders*, *Phys. Rev.* **D42** (1990) 3052–3077. 2.3

- 2520 [27] G. van den Oord, *Recursion, Monte Carlo and Vector Boson Scattering at Hadron Colliders*.
 2521 PhD thesis, Nijmegen U., 2012.
 2522 http://www.nikhef.nl/pub/services/biblio/theses_pdf/thesis_G_v_d_Oord.pdf. 2.3,
 2523 2.3
- 2524 [28] A. Alboteanu, W. Kilian, and J. Reuter, *Resonances and Unitarity in Weak Boson*
 2525 *Scattering at the LHC*, *JHEP* **11** (2008) 010, arXiv:0806.4145 [hep-ph]. 2.6
- 2526 [29] L. R. Evans and P. Bryant, *LHC Machine*, *JINST* **3** (2008) S08001.
 2527 <https://cds.cern.ch/record/1129806>. This report is an abridged version of the LHC
 2528 Design Report (CERN-2004-003). 3.1
- 2529 [30] ATLAS Collaboration, *The ATLAS Experiment at the CERN Large Hadron Collider*, *JINST*
 2530 **3** (2008) S08003. 3.1, 3.5
- 2531 [31] ALICE Collaboration, K. Aamodt et al., *The ALICE experiment at the CERN LHC*, *JINST*
 2532 **3** (2008) S08002. 3.1
- 2533 [32] CMS Collaboration, S. Chatrchyan et al., *The CMS Experiment at the CERN LHC*, *JINST*
 2534 **3** (2008) S08004. 3.1
- 2535 [33] LHCb Collaboration, A. A. Alves, Jr. et al., *The LHCb Detector at the LHC*, *JINST* **3**
 2536 (2008) S08005. 3.1
- 2537 [34] CERN, *The accelerator complex*, February, 2019.
 2538 <https://home.cern/science/accelerators/accelerator-complex>. 3.1
- 2539 [35] E. Mobs, *The CERN accelerator complex. Complexe des accrateurs du CERN*, .
 2540 <https://cds.cern.ch/record/2197559>. General Photo. 3.1
- 2541 [36] W. Herr and B. Muratori, *Concept of luminosity*, . <https://cds.cern.ch/record/941318>.
 2542 3.1
- 2543 [37] ATLAS Collaboration, *ATLAS Experiment – Public Results: Luminosity Public Results Run*
 2544 *2*, February, 2019.
 2545 <https://twiki.cern.ch/twiki/bin/view/AtlasPublic/LuminosityPublicResultsRun2>.
 2546 3.1, 3.2, 3.3, 3.4, 3.1
- 2547 [38] ATLAS Collaboration Collaboration, *ATLAS inner detector: Technical Design Report*, **1**.
 2548 Technical Design Report ATLAS. CERN, Geneva, 1997.
 2549 <https://cds.cern.ch/record/331063>. 3.2.1
- 2550 [39] ATLAS Collaboration Collaboration, S. Haywood, L. Rossi, R. Nickerson, and
 2551 A. Romanouk, *ATLAS inner detector: Technical Design Report*, **2**. Technical Design Report
 2552 ATLAS. CERN, Geneva, 1997. <https://cds.cern.ch/record/331064>. 3.2.1
- 2553 [40] ATLAS Collaboration Collaboration, M. Capeans, G. Darbo, K. Einsweiller, M. Elsing,
 2554 T. Flick, M. Garcia-Sciveres, C. Gemme, H. Pernegger, O. Rohne, and R. Vuillermet,
 2555 *ATLAS Insertable B-Layer Technical Design Report*, Tech. Rep. CERN-LHCC-2010-013.
 2556 ATLAS-TDR-19, Sep, 2010. <https://cds.cern.ch/record/1291633>. 3.2.1.1
- 2557 [41] ATLAS Collaboration, G. Darbo, *Experience on 3D Silicon Sensors for ATLAS IBL*, *JINST*
 2558 **10** (2015) no. 05, C05001, arXiv:1411.6937 [physics.ins-det]. 3.2.1.1

- 2559 [42] E. Stanecka, *ATLAS Inner Tracker Performance at the Beginning of the LHC Run 2*, Tech.
2560 Rep. ATL-INDET-PROC-2016-002, CERN, Geneva, Apr, 2016.
2561 <https://cds.cern.ch/record/2147407>. 3.2.1.1
- 2562 [43] ATLAS TRT Collaboration, E. Abat et al., *The ATLAS Transition Radiation Tracker
(TRT) proportional drift tube: Design and performance*, *JINST* **3** (2008) P02013. 3.2.1.3
- 2564 [44] ATLAS TRT Collaboration, E. Abat et al., *The ATLAS TRT barrel detector*, *JINST* **3**
2565 (2008) P02014. 3.2.1.3
- 2566 [45] E. Abat et al., *The ATLAS TRT end-cap detectors*, *JINST* **3** (2008) P10003. 3.2.1.3
- 2567 [46] ATLAS Collaboration Collaboration, *ATLAS liquid-argon calorimeter: Technical Design
Report*. Technical Design Report ATLAS. CERN, Geneva, 1996.
2569 <https://cds.cern.ch/record/331061>. 3.2.2, 3.8
- 2570 [47] ATLAS Collaboration Collaboration, *ATLAS tile calorimeter: Technical Design Report*.
2571 Technical Design Report ATLAS. CERN, Geneva, 1996.
2572 <https://cds.cern.ch/record/331062>. 3.2.2
- 2573 [48] ATLAS Collaboration Collaboration, *ATLAS muon spectrometer: Technical Design Report*.
2574 Technical Design Report ATLAS. CERN, Geneva, 1997.
2575 <https://cds.cern.ch/record/331068>. 3.2.3
- 2576 [49] T. Cornelissen, M. Elsing, I. Gavrilenko, W. Liebig, E. Moyse, and A. Salzburger, *The new
2577 ATLAS track reconstruction (NEWT)*, J. Phys.: Conf. Ser. **119** (2008) 032014.
2578 <http://cds.cern.ch/record/1176900>. 3.2.4.1
- 2579 [50] ATLAS Collaboration, *ATLAS inner detector: Technical Design Report, Vol. 1*. CERN,
2580 Geneva, 1997. <https://cds.cern.ch/record/331063>. 4
- 2581 [51] P. F. Åkesson, T. Atkinson, M. J. Costa, M. Elsing, S. Fleischmann, A. N. Gaponenko,
2582 W. Liebig, E. Moyse, A. Salzburger, and M. Siebel, *ATLAS Tracking Event Data Model*,
2583 Tech. Rep. ATL-SOFT-PUB-2006-004. ATL-COM-SOFT-2006-005.
2584 CERN-ATL-COM-SOFT-2006-005, CERN, Geneva, Jul, 2006.
2585 <https://cds.cern.ch/record/973401>. 4.1
- 2586 [52] P. Brückman, A. Hicheur, and S. J. Haywood, *Global chi2 approach to the Alignment of the
2587 ATLAS Silicon Tracking Detectors*, Tech. Rep. ATL-INDET-PUB-2005-002.
2588 ATL-COM-INDET-2005-004. CERN-ATL-INDET-PUB-2005-002, CERN, Geneva, 2005.
2589 <https://cds.cern.ch/record/835270>. 4.1, 4.1
- 2590 [53] ATLAS Collaboration Collaboration, *Alignment of the ATLAS Inner Detector Tracking
2591 System with 2010 LHC proton-proton collisions at $\sqrt{s} = 7$ TeV*, Tech. Rep.
2592 ATLAS-CONF-2011-012, CERN, Geneva, Mar, 2011.
2593 <https://cds.cern.ch/record/1334582>. 4.1, 4.2.3, 4.15
- 2594 [54] R. Härtel and S. Bethke, *Iterative local Chi2 alignment approach for the ATLAS SCT
2595 detector*. PhD thesis, Nov, 2005. <http://cds.cern.ch/record/1511044>. Presented 28 Nov
2596 2005. 4.1
- 2597 [55] ATLAS Collaboration Collaboration, P. Brückman de Renstrom, *Alignment strategy for the
2598 Inner Detector of ATLAS*, . <https://cds.cern.ch/record/1047114>. 4.1

- 2599 [56] *Alignment of the ATLAS Inner Detector and its Performance in 2012*, Tech. Rep.
2600 ATLAS-CONF-2014-047, CERN, Geneva, Jul, 2014.
2601 <https://cds.cern.ch/record/1741021>. 4.1, 4.2.1, 4.4
- 2602 [57] J. J. Peña, *Alignment of the ATLAS Inner Detector Upgraded for the LHC Run II*, *J. Phys.*
2603 *Conf. Ser.* **664** (2015) no. 7, 072025. 4.1
- 2604 [58] J. Alison and I. J. Kroll, *The Road to Discovery: Detector Alignment, Electron Identification,*
2605 *Particle Misidentification, WW Physics, and the Discovery of the Higgs Boson*. PhD thesis,
2606 Dec, 2015. <https://cds.cern.ch/record/1536507>. Presented 08 Nov 2012. 9
- 2607 [59] *ATLAS Inner Detector Alignment Performance with February 2015 Cosmic Rays Data*,
2608 Tech. Rep. ATL-PHYS-PUB-2015-009, CERN, Geneva, Apr, 2015.
2609 <https://cds.cern.ch/record/2008724>. 4.3, 4.2
- 2610 [60] *Alignment of the ATLAS Inner Detector with the initial LHC data at $\sqrt{s} = 13$ TeV*, Tech.
2611 Rep. ATL-PHYS-PUB-2015-031, CERN, Geneva, Jul, 2015.
2612 <https://cds.cern.ch/record/2038139>. 4.2
- 2613 [61] *Study of the mechanical stability of the ATLAS Insertable B-Layer*, Tech. Rep.
2614 ATL-INDET-PUB-2015-001, CERN, Geneva, Jun, 2015.
2615 <https://cds.cern.ch/record/2022587>. 4.2.1
- 2616 [62] *Common Framework Implementation for the Track-Based Alignment of the ATLAS*
2617 *Detector*, Tech. Rep. ATL-SOFT-PUB-2014-003, CERN, Geneva, Mar, 2014.
2618 <https://cds.cern.ch/record/1670354>. 4.2.1
- 2619 [63] ATLAS Collaboration Collaboration, *Study of alignment-related systematic effects on the*
2620 *ATLAS Inner Detector track reconstruction*, Tech. Rep. ATLAS-CONF-2012-141, CERN,
2621 Geneva, Oct, 2012. <https://cds.cern.ch/record/1483518>. 4.4, 4.4, 4.4.1.1, 4.4.1.2
- 2622 [64] S. Marti-Garcia, S. Camarda, T. Golling, M. Danninger, N. A. Styles, J. Wollrath, W. K.
2623 Di Clemente, S. Henkelmann, J. Jimenez Peña, O. Estrada Pastor, A. K. Morley, H. Oide,
2624 A. T. Vermeulen, P. Butti, E. Ricci, F. M. Follega, and R. Iuppa, *Studies of radial*
2625 *distortions of the ATLAS Inner Detector*, Tech. Rep. ATL-COM-INDET-2018-010, CERN,
2626 Geneva, Mar, 2018. <https://cds.cern.ch/record/2306724>. 4.4
- 2627 [65] ATLAS Collaboration Collaboration, *Electron and photon energy calibration with the ATLAS*
2628 *detector using data collected in 2015 at $\sqrt{s} = 13$ TeV*, Tech. Rep. ATL-PHYS-PUB-2016-015,
2629 CERN, Geneva, Aug, 2016. <https://cds.cern.ch/record/2203514>. 4.4.1
- 2630 [66] ATLAS Collaboration, ATLAS Collaboration, *Evidence for Electroweak Production*
2631 *of $W^\pm W^\pm jj$ in pp Collisions at $\sqrt{s} = 8$ TeV with the ATLAS Detector*, *Phys. Rev. Lett.*
2632 **113** (2014) no. 14, 141803, arXiv:1405.6241 [hep-ex]. 5
- 2633 [67] CMS Collaboration, V. Khachatryan et al., *Study of vector boson scattering and search for*
2634 *new physics in events with two same-sign leptons and two jets*, *Phys. Rev. Lett.* **114** (2015)
2635 no. 5, 051801, arXiv:1410.6315 [hep-ex]. 5
- 2636 [68] ATLAS Collaboration Collaboration, *Observation of electroweak production of a same-sign*
2637 *W boson pair in association with two jets in pp collisions at $\sqrt{s} = 13$ TeV with the ATLAS*
2638 *detector*, Tech. Rep. ATLAS-CONF-2018-030, CERN, Geneva, Jul, 2018.
2639 <https://cds.cern.ch/record/2629411>. 5, 5.7, 6.6.2

- 2640 [69] CMS Collaboration, CMS Collaboration, *Observation of electroweak production of same-sign*
 2641 *W boson pairs in the two jet and two same-sign lepton final state in proton-proton collisions*
 2642 *at $\sqrt{s} = 13$ TeV*, arXiv:1709.05822 [hep-ex]. 5
- 2643 [70] C. Bittrich, W. K. Di Clemente, et al., *Support note for measurement of electroweak*
 2644 *$W^\pm W^\pm jj$ production at $\sqrt{s} = 13$ TeV*, Tech. Rep. ATL-COM-PHYS-2018-252, CERN,
 2645 Geneva, Mar, 2018. <https://cds.cern.ch/record/2309552>. 5, 5.3.3, 2, 4, 5.4.3
- 2646 [71] J. M. Campbell and R. K. Ellis, *Higgs Constraints from Vector Boson Fusion and*
 2647 *Scattering*, JHEP **04** (2015) 030, arXiv:1502.02990 [hep-ph]. 5.0.1, 5.0.2
- 2648 [72] M. Szleper, *The Higgs boson and the physics of WW scattering before and after Higgs*
 2649 *discovery*, arXiv:1412.8367 [hep-ph]. 5.0.1
- 2650 [73] E. Accomando, A. Ballestrero, A. Belhouari, and E. Maina, *Isolating Vector Boson Scattering*
 2651 *at the LHC: Gauge cancellations and the Equivalent Vector Boson Approximation vs*
 2652 *complete calculations*, Phys. Rev. **D74** (2006) 073010, arXiv:hep-ph/0608019 [hep-ph]. 5.0.1
- 2653 [74] C. Gumpert, M. Kobel, B. Heinemann, and U. Klein, *Measurement of Electroweak Gauge*
 2654 *Boson Scattering in the Channel $pp \rightarrow W^\pm W^\pm jj$ with the ATLAS Detector at the Large*
 2655 *Hadron Collider*. PhD thesis, Dec, 2014. <https://cds.cern.ch/record/2003240>.
 2656 Presented 27 Feb 2015. 5.0.2, 5.1
- 2657 [75] B. Jager, L. Salfelder, M. Worek, and D. Zeppenfeld, *Physics opportunities for vector-boson*
 2658 *scattering at a future 100 TeV hadron collider*, Phys. Rev. **D96** (2017) no. 7, 073008,
 2659 arXiv:1704.04911 [hep-ph]. 5.6
- 2660 [76] J. Almond, L. Bianchini, et al., *Search for heavy neutrino, W_R and Z_R gauge bosons in*
 2661 *events with two high- P_T leptons and jets with the ATLAS detector in pp collisions at $\sqrt{s} = 8$*
 2662 *TeV*, Tech. Rep. ATL-COM-PHYS-2013-810, CERN, Geneva, Jun, 2013.
<https://cds.cern.ch/record/1555805>. Supporting note for EXOT-2012-24, published as
 2663 JHEP07 (2015) 162. 5.0.3
- 2665 [77] ATLAS Collaboration, M. Aaboud et al., *Luminosity determination in pp collisions at $\sqrt{s} = 8$*
 2666 *TeV using the ATLAS detector at the LHC*, Eur. Phys. J. **C76** (2016) no. 12, 653,
 2667 arXiv:1608.03953 [hep-ex]. 5.1
- 2668 [78] G. Avoni et al., *The new LUCID-2 detector for luminosity measurement and monitoring in*
 2669 *ATLAS*, JINST **13** (2018) no. 07, P07017. 5.1
- 2670 [79] ATLAS Collaboration, G. Aad et al., *The ATLAS Simulation Infrastructure*, Eur. Phys. J. **C70** (2010) 823–874, arXiv:1005.4568 [physics.ins-det]. 5.1.1
- 2672 [80] S. Agostinelli et al., *GEANT4 - a simulation toolkit*, Nucl. Instrum. Meth. **A506** (2003)
 2673 250–303. 5.1.1
- 2674 [81] T. Sjostrand, S. Mrenna, and P. Skands, *A Brief Introduction to PYTHIA 8.1*, Comput.
- 2675 Phys. Commun. **178** (2008) 852–867, arXiv:0710.3820 [hep-ph]. 5.1.1
- 2676 [82] T. Gleisberg et al., *Event generation with SHERPA 1.1*, JHEP **02** (2009) 007,
 2677 arXiv:0811.4622 [hep-ph]. 5.1.1
- 2678 [83] S. Schumann and F. Krauss, *A parton shower algorithm based on Catani-Seymour dipole*
 2679 *factorization*, JHEP **03** (2008) 038, arXiv:0709.1027 [hep-ph]. 5.1.1

- 2680 [84] S. Höche, F. Krauss, S. Schumann, and F. Siegert, *QCD matrix elements and truncated*
 2681 *showers*, JHEP **05** (2009) 053, arXiv:0903.1219 [hep-ph]. 5.1.1
- 2682 [85] R. D. Ball et al., *Parton distributions for the LHC Run II*, JHEP **04** (2015) 040,
 2683 arXiv:1410.8849 [hep-ph]. 5.1.1
- 2684 [86] S. Alioli, P. Nason, C. Oleari, and E. Re, *A general framework for implementing NLO*
 2685 *calculations in shower Monte Carlo programs: the POWHEG BOX*, JHEP **06** (2010) 043,
 2686 arXiv:1002.2581 [hep-ph]. 5.1.1
- 2687 [87] A. Ballestrero et al., *Precise predictions for same-sign W-boson scattering at the LHC*, Eur.
 2688 Phys. J. **C78** (2018) no. 8, 671, arXiv:1803.07943 [hep-ph]. 5.1.1
- 2689 [88] J. Alwall, R. Frederix, S. Frixione, V. Hirschi, F. Maltoni, O. Mattelaer, H. S. Shao,
 2690 T. Stelzer, P. Torrielli, and M. Zaro, *The automated computation of tree-level and*
 2691 *next-to-leading order differential cross sections, and their matching to parton shower*
 2692 *simulations*, JHEP **07** (2014) 079, arXiv:1405.0301 [hep-ph]. 5.1.1
- 2693 [89] H.-L. Lai, M. Guzzi, J. Huston, Z. Li, P. M. Nadolsky, J. Pumplin, and C. P. Yuan, *New*
 2694 *parton distributions for collider physics*, Phys. Rev. D **82** (2010) 074024, arXiv:1007.2241
 2695 [hep-ph]. 5.1.1
- 2696 [90] T. Sjostrand, S. Mrenna, and P. Skands, *PYTHIA 6.4 physics and manual*, JHEP **05** (2006)
 2697 026, arXiv:0603175 [hep-ph]. 5.1.1
- 2698 [91] ATLAS Collaboration, G. Aad et al., *Muon reconstruction performance of the ATLAS*
 2699 *detector in protonproton collision data at $\sqrt{s} = 13$ TeV*, Eur. Phys. J. **C76** (2016) no. 5, 292,
 2700 arXiv:1603.05598 [hep-ex]. 5.2.1.1, 15
- 2701 [92] ATLAS Collaboration Collaboration, *Electron efficiency measurements with the ATLAS*
 2702 *detector using the 2015 LHC proton-proton collision data*, Tech. Rep.
 2703 ATLAS-CONF-2016-024, CERN, Geneva, Jun, 2016.
 2704 <https://cds.cern.ch/record/2157687>. 5.2.1.2
- 2705 [93] M. Cacciari, G. P. Salam, G. Soyez, *The anti- k_t jet clustering algorithm*, JHEP **04** (2008)
 2706 063, arXiv:0802.1189 [hep-ph]. 5.2.1.3
- 2707 [94] ATLAS Collaboration, M. Aaboud et al., *Jet energy scale measurements and their systematic*
 2708 *uncertainties in proton-proton collisions at $\sqrt{s} = 13$ TeV with the ATLAS detector*, Phys.
 2709 Rev. D **96** (2017) no. 7, 072002, arXiv:1703.09665 [hep-ex]. 5.2.1.3
- 2710 [95] *Tagging and suppression of pileup jets with the ATLAS detector*, Tech. Rep.
 2711 ATLAS-CONF-2014-018, CERN, Geneva, May, 2014.
 2712 <http://cds.cern.ch/record/1700870>. 5.2.1.3
- 2713 [96] D. Adams, C. Anastopoulos, et al., *Recommendations of the Physics Objects and Analysis*
 2714 *Harmonisation Study Groups 2014*, Tech. Rep. ATL-PHYS-INT-2014-018, CERN, Geneva,
 2715 Jul, 2014. <https://cds.cern.ch/record/1743654>. 5.2.1.4
- 2716 [97] ATLAS Collaboration, M. Aaboud et al., *Measurement of the cross-section for producing a*
 2717 *W boson in association with a single top quark in pp collisions at $\sqrt{s} = 13$ TeV with ATLAS*,
 2718 JHEP **01** (2018) 063, arXiv:1612.07231 [hep-ex]. 5.2.1.4

- 2719 [98] ATLAS Collaboration, M. Aaboud et al., *Performance of missing transverse momentum*
 2720 *reconstruction with the ATLAS detector using proton-proton collisions at $\sqrt{s} = 13$ TeV*,
 2721 *Eur. Phys. J.* **C78** (2018) no. 11, 903, arXiv:1802.08168 [hep-ex]. 5.2.2
- 2722 [99] ATLAS Collaboration, M. Aaboud et al., *Measurements of b-jet tagging efficiency with the*
 2723 *ATLAS detector using $t\bar{t}$ events at $\sqrt{s} = 13$ TeV*, *JHEP* **08** (2018) 089, arXiv:1805.01845
 2724 [hep-ex]. 5.2.2
- 2725 [100] J.-F. Arguin, J. Claude, G. Gonella, B. P. Kersevan, K. Koneke, K. Lohwasser,
 2726 K. Mochizuki, M. Muskinja, C. Piaulet, and P. Sommer, *Support Note for Electron ID:*
 2727 *charge mis-identification*, Tech. Rep. ATL-COM-PHYS-2017-1014, CERN, Geneva, Jul,
 2728 2017. <https://cds.cern.ch/record/2273365>. 5.3.3
- 2729 [101] C.-H. Kom and W. J. Stirling, *Charge asymmetry in $W + \text{jets}$ production at the LHC*, *Eur.*
 2730 *Phys. J.* **C69** (2010) 67–73, arXiv:1004.3404 [hep-ph]. 5.4
- 2731 [102] R. Steerenberg, *LHC Report: Another run is over and LS2 has just begun...*,
 2732 [https://home.cern/news/news/accelerators/](https://home.cern/news/news/accelerators/lhc-report-another-run-over-and-ls2-has-just-begun)
 2733 [lhc-report-another-run-over-and-ls2-has-just-begun](https://home.cern/news/news/accelerators/lhc-report-another-run-over-and-ls2-has-just-begun), 2018. Accessed: 2018-12-14. 6
- 2734 [103] *Letter of Intent for the Phase-I Upgrade of the ATLAS Experiment*, Tech. Rep.
 2735 CERN-LHCC-2011-012. LHCC-I-020, CERN, Geneva, Nov, 2011.
 2736 <http://cds.cern.ch/record/1402470>. 6
- 2737 [104] G. Apollinari, I. Bjar Alonso, O. Brning, M. Lamont, and L. Rossi, *High-Luminosity Large*
 2738 *Hadron Collider (HL-LHC): Preliminary Design Report*. CERN Yellow Reports:
 2739 Monographs. CERN, Geneva, 2015. <https://cds.cern.ch/record/2116337>. 6
- 2740 [105] ATLAS Collaboration Collaboration, ATLAS Collaboration, *ATLAS Phase-II Upgrade*
 2741 *Scoping Document*, Cern-lhcc-2015-020, Geneva, Sep, 2015.
 2742 <http://cds.cern.ch/record/2055248>. 6
- 2743 [106] D. Espriu and B. Yencho, *Longitudinal WW scattering in light of the “Higgs boson”*
 2744 *discovery*, *Phys. Rev. D* **87** (2013) 055017, arXiv:1212.4158 [hep-ph]. 6, 6.1
- 2745 [107] ATLAS Collaboration Collaboration, *Prospects for the measurement of the $W^\pm W^\pm$*
 2746 *scattering cross section and extraction of the longitudinal scattering component in pp*
 2747 *collisions at the High-Luminosity LHC with the ATLAS experiment*, Tech. Rep.
 2748 ATL-PHYS-PUB-2018-052, CERN, Geneva, Dec, 2018.
 2749 <http://cds.cern.ch/record/2652447>. 6
- 2750 [108] ATLAS Collaboration Collaboration, *Studies on the impact of an extended Inner Detector*
 2751 *tracker and a forward muon tagger on $W^\pm W^\pm$ scattering in pp collisions at the*
 2752 *High-Luminosity LHC with the ATLAS experiment*, Tech. Rep. ATL-PHYS-PUB-2017-023,
 2753 CERN, Geneva, Dec, 2017. <https://cds.cern.ch/record/2298958>. 6, 6.4
- 2754 [109] T. Sjöstrand, S. Ask, J. R. Christiansen, R. Corke, N. Desai, P. Ilten, S. Mrenna, S. Prestel,
 2755 C. O. Rasmussen, and P. Z. Skands, *An Introduction to PYTHIA 8.2*, *Comput. Phys.*
 2756 *Commun.* **191** (2015) 159–177, arXiv:1410.3012 [hep-ph]. 6.2
- 2757 [110] ATLAS Collaboration Collaboration, *Expected performance for an upgraded ATLAS detector*
 2758 *at High-Luminosity LHC*, Tech. Rep. ATL-PHYS-PUB-2016-026, CERN, Geneva, Oct, 2016.
 2759 <http://cds.cern.ch/record/2223839>. 6.3

- 2760 [111] P. C. Bhat, H. B. Prosper, S. Sekmen, and C. Stewart, *Optimizing Event Selection with the*
2761 *Random Grid Search*, [Comput. Phys. Commun.](#) **228** (2018) 245–257, [arXiv:1706.09907](#)
2762 [[hep-ph](#)]. [6.5.1](#)
- 2763 [112] G. Cowan, K. Cranmer, E. Gross, and O. Vitells, *Asymptotic formulae for likelihood-based*
2764 *tests of new physics*, [Eur. Phys. J.](#) **C71** (2011) 1554, [arXiv:1007.1727](#) [[physics.data-an](#)].
2765 [Erratum: [Eur. Phys. J.](#) C73,2501(2013)]. [6.5.1](#)